5-3-2018

Polychromatic Optical Forces in Diatomic Systems

Scott Edwin Galica
University of Connecticut - Storrs, scott.galica@uconn.edu

Polychromatic Optical Forces in Diatomic Systems

Scott E. Galica, Ph.D.

University of Connecticut, 2018

This dissertation discusses an experiment to demonstrate the application of the stimulated bichromatic optical force (BCF) on the diatomic molecule calcium monofluoride (CaF). The research demonstrates the deflection of a supersonic beam of CaF through the application of BCF under a variety of conditions, highlighting distinctive characteristics of the force. Results show that the measured deflection of the molecular beam is consistent with the behavior of BCF under the tested conditions. In particular, we have measured a predicted reversal in the direction of the force as well as an applied force which exceeds the radiation pressure force. Detailed modeling of the BCF in multilevel systems corroborates our findings. We discuss the development and application of these models with respect to non-ideal conditions present in the experiment. The construction of the molecular beam source and BCF laser systems are discussed in detail. A brief discussion of further modeled extensions of the BCF through the addition of higher order sidebands is presented as well. Overall, our results demonstrate that the BCF is a potentially useful tool for manipulation of cold molecules.

Polychromatic Optical Forces in Diatomic Systems

Scott E. Galica

B.A., Colby College, Waterville, ME 2011

M.S., University of Connecticut, Storrs, CT 2013

A Dissertation

Submitted in Partial Fullfilment of the

Requirements for the Degree of

Doctor of Philosophy

at the

University of Connecticut

2018

APPROVAL PAGE

Doctor of Philosophy Dissertation

Polychromatic Optical Forces in Diatomic Systems

Presented by

Scott E. Galica, B.A., M.S.

Major Advisor

Phillip Gould

Associate Advisor

Robin Côté

Associate Advisor

Winthrop Smith

University of Connecticut

2018

To Dr. Edward E. Eyler

ACKNOWLEDGEMENTS

As anyone who's gone through it can tell you: getting a degree can be a long process. This process is almost never one that's carried out alone, and I'd like to take this opportunity to thank some of the people who helped me along my way:

First of all, I'd like to thank my advisory committee. My advisor, Professor Phillip Gould, for agreeing to take on my project on top of his own research and for sticking with me through to the end. His guidance and insight was invaluable to my research and I would not have been able to complete my project without his aid. My associate advisors, Professor Robin Côté and Professor Winthrop Smith, for their helpful comments and constructive insights on my work, in particular on this thesis.

Professor Dan McCarron for his assistance with completing my experiment and for his interest in continuing it in the future.

The physics department office staff for their help navigating the University bureaucracy and coordinating the logistical nightmare that is graduate research. In particular, I'd like to thank Micki Bellamy and Anna Huang for their help (and patience) with my last-minute scheduling issues.

The physics department technical staff, in particular Dave Perry for his assistance with keeping the lab in one piece and Alan Chasse for building the experimental apparatus in the first place.

My former group members: Leland Aldridge, for his invaluable insight and theory support; Drew Chieda, for laying much of the groundwork for my experiment and introducing me to the lab; and Donal Sheets, for his assistance both in

and out of the lab.

The undergraduate "army" that has come through the lab: Tony Le, Michael Cantara, Kurt Nesteruk, Matt Knocklein, and Brian Roy.

My friends and fellow graduate students, current and past, who are too many to name, but who have all shared with me many long hours of problems sets, studying, teaching, and research. My experience would not have been the same without the willingness of the graduate student community to offer assistance, advice, and motivation.

To my family for their constant support and affirmation, which helped me maintain perspective and stay motivated when things got difficult.

To my friends and roommates for offering much-needed diversions and helping to keep me grounded. And of course, to my writing partner T. T.-S. R.-G. G. Norton.

To my girlfriend, Kate Jones, for sticking with me through this entire process despite the distance, long hours, and inevitable hardships.

Lastly, I'd like to thank Edward E. Eyler. He was an exceptional mentor, and I consider myself lucky to have had the opportunity to work along side him. He taught me how to be a better researcher, how to ask the right questions, and to have the persistence to do things the right way, even if it's harder. It was a privilege to call him my mentor.

TABLE OF CONTENTS

LIST OF FIGURES

LIST OF TABLES

Chapter 1

Introduction

Since the radiative force made its experimental debut [1–3], optical forces have grown to be an invaluable tool in the study of experimental atomic, molecular, and optical physics. For many experiments, particularly those concerned with spectroscopy, optical force slowing and cooling have become an almost mandatory first step preceding any further manipulation or observations. As is commonly the case in physics research, the first applications of optical forces occurred in relatively simple systems—atoms—using a straightforward technique—the radiative force (see section 1.1.1). Ever since the initial demonstrations, the progression of optical forces has followed a familiar story: find the limitations of the technique and then find methods to circumvent them. Following this principle, the road-map of optical forces leads away from the radiative force, through the dipole force, and into stimulated optical forces. Of particular interest to this research is the stimulated force known as the bichromatic force (see chapter 2). In brief, the bichromatic force uses a pair of two-color beams to coherently drive transitions within the system, allowing it to exchange momentum at a much higher rate than the radiative force [4–11]. This technique has been extensively explored in a variety of species including Cs [12], Rb [13], Na [14], and He [8, 9], which includes work from within our own group.

For the most part, the progression of optical forces has relied on atoms as a testing ground. Recently, however, there has been an increasing interest in expanding the map along a different route, namely, into the exploration of more complicated systems: molecules. The increased complexity of molecular species had stifled interest in their study, but recent successes in radiatively slowing several different species [15–20] have since kindled a new wave of interest. These successes, while impressive, have relied on stringent conditions placed upon the species under study and typically require a large number of laser frequencies to properly implement.

It is the purpose of this research to explore and demonstrate an alternative method of molecular slowing. Using stimulated force techniques, first developed for atomic applications, we demonstrate the deflection of a diatomic molecular beam via the bichromatic force. The use of such a stimulated force allows us to maximize the applied force on the beam while minimizing the number of spontaneous decay events which occur. The result is a large force with wide velocity range, and which requires only a single driving laser to apply.

1.1 Optical Forces on Atoms

The internal structure of an atom is principally determined by the electrostatic interactions between its nucleus and electrons. Despite being a many-body problem, the symmetry of the potential limits the number of degrees of freedom that must be considered. This is especially true for effectively single-active-electron atoms, such as alkali metals and rare gases in metastable states, and results in a relatively simple energy structure that underlies any additional perturbations that are considered. The simplicity of this architecture makes atoms an

ideal playground for testing theories and techniques—in particular, optical forces.

1.1.1 Radiative Force

The most basic of the optical forces is the radiative force. The radiative force is generated through scattering of resonant photons incident on an atom [21, 22], as illustrated in Fig. 1.1. The dynamics of this system are most easily illustrated by considering a simplified two-level system. While a pure two-level model is not a strictly accurate description of the internal structure of an atom, it does encapsulate most of the underlying dynamics of the radiative force. Thus, consider a system with two energy levels: a ground state, $|g\rangle$, with energy $E_0 = 0$ and an excited state, $|e\rangle$, with energy $E_1 = \hbar\omega_0$. Introducing a monochromatic light field with frequency $\omega_l = \omega_0 + \delta$ and wave vector $\vec{k} = (\omega_l/c)\hat{x}$ (where $\hat{x}$ indicates the direction of propagation) that couples the two states, allowing electronic transitions between them to occur. By absorbing a photon from the light field, the atom transitions from its ground state to its excited state and simultaneously receives an impulse of $\Delta\vec{p} = \hbar\vec{k}$ due to conservation of momentum. Once excited, the system cannot absorb any additional photons and must first de-excite before additional impulses can be imparted to it [23].

The atom can return to the ground state through one of two paths. In the limit of low light field intensity, the decay is dominated by spontaneous emission. The upper state is not stable and can decay back to the ground state by emitting a photon. This decay is a random process with an average lifetime of τ—i.e. a fixed decay rate $\Gamma = 1/\tau$—determined by the coupling strength between the energy levels. Spontaneously emitted photons are distributed symmetrically such that they impart an average impulse of $\overline{\Delta\vec{p}} = 0$ over several decay events. The average

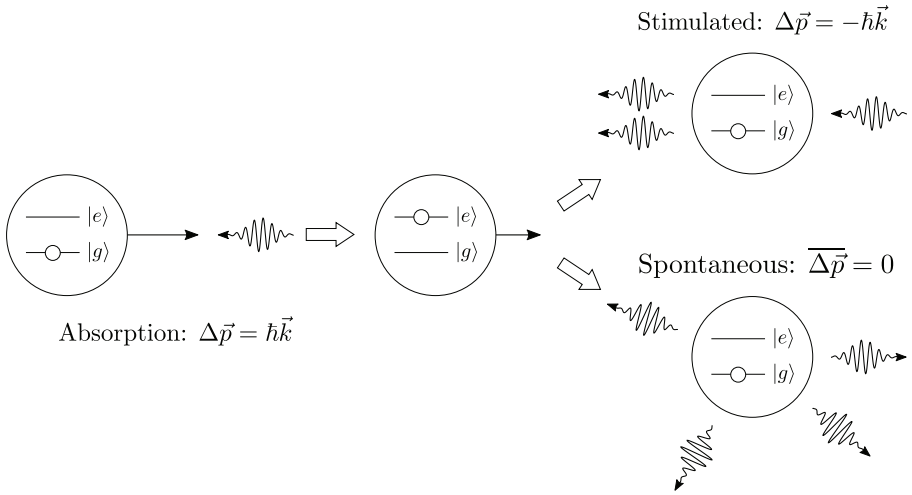

Fig. 1.1: A diagram illustrating the process of the radiative force on a two-level atom. The atom absorbs an incident photon and becomes internally excited. In doing so, by conservation of momentum, the atom receives an impulse, $\Delta\vec{p} = \hbar\vec{k}$. Before the atom can absorb another photon, it must first return to its ground state. It can do this in either of two ways: spontaneous emission (bottom), in which the atom emits a randomly-directed photon, imparting an average impulse of 0; or stimulated emission (top), in which emission is induced by the presence of a secondary photon, imparting an impulse of $\Delta\vec{p} = -\hbar\vec{k}$. Thus the average net momentum transfer for an absorption/emission cycle ending with spontaneous decay is $\overline{\Delta\vec{p}_{net}} = \hbar\vec{k}$ and ending with stimulated emission is $\Delta\vec{p}_{net} = 0$.

net momentum transfer to the atom is thus $\Delta\vec{p}_{net} = \hbar\vec{k}$ per excitation cycle. Alternatively, in the limit of high light field intensity or long upper state lifetime, the return to the ground state becomes dominated by stimulated emission. Just as a photon can be absorbed by an atom to induce an excitation, so too can a photon induce stimulated emission in the atom. When a downward transition is induced in this way, it causes the atom to emit a photon identical to the one which induced the decay. By conservation of momentum, the atom receives an impulse $\Delta\vec{p} = -\hbar\vec{k}$ leading to a net momentum transfer of $\Delta\vec{p}_{net} = 0$ for the excitation cycle. Combining these two decay mechanisms, we can define a photon scattering rate, γ_{sc} [23], such that the net force acting on the atom becomes $\vec{F}_{rad} = \hbar\vec{k}\gamma_{sc}$. For an atom moving at velocity $\vec{v}$ in a light field of intensity I, we find that this scattering rate is given by

$$\gamma_{sc} = \frac{s\Gamma/2}{1 + s + (2(\delta - \vec{k}\cdot\vec{v})/\Gamma)^2}, \tag{1.1.1}$$

where Γ is the upper state decay rate and δ is the detuning, as defined previously. The dimensionless quantity s is the saturation parameter, defined as

$$s = I\frac{3\lambda^3}{\pi hc\Gamma} = \frac{I}{I_{sat}}, \tag{1.1.2}$$

for laser intensity I and saturation intensity I_{sat} defined as

$$I_{sat} = \frac{\pi hc}{3\lambda^3\tau} = \frac{\pi hc\Gamma}{3\lambda^3}. \tag{1.1.3}$$

From the expression for γ_{sc} we find two relevant limits. In the limit $I \to 0$ we find the scattering rate (and thus the force) also approaches zero, as we might expect.

In the limit of high intensity ($I \to \infty$), however, we find that the scattering rate asymptotically approaches value of $\gamma_{sc} = \Gamma/2$. It follows from this limit that the maximum achievable force is $F_{rad}^{max} = \hbar k\Gamma/2$ which is scaled by Γ, an internal property of the system. This can be seen in Fig. 1.2. Due to this limit on the force magnitude, long interaction times may be required to apply significant momentum changes to the system. For systems where the interaction time is limited—for example, where high velocity limits the interaction time or where decay pathways to optically inaccessible states limit the number of transition cycles—the radiative force loses its utility.

1.1.2 Dipole Force

For systems where the interaction time sets the primary limit on the applied force, it becomes necessary to increase the magnitude of the force in order to impart a sufficient change in velocity. As stated previously, the magnitude of the radiative force cannot be increased beyond its fundamental limit of $\hbar k\Gamma/2$, set by the reliance of resonant scattering on spontaneous decay to reset the system before subsequent impulses can be applied. Increasing the force beyond this limit requires a method which does not depend on spontaneous decay to reset the system. One such method is to avoid using resonant scattering altogether, and instead make use of a different mechanism to impart a force.

An atom placed in a non-resonant optical field will experience a shift in its energy levels due to the external field. From a semi-classical perspective, the presence of the external field induces an electric dipole moment within the atom proportional to the external field magnitude, $\vec{p} = -\alpha\vec{E}$. The induced dipole then interacts with the external field, introducing a dipole potential [24], $U = -\frac{1}{2}\alpha E^2$,

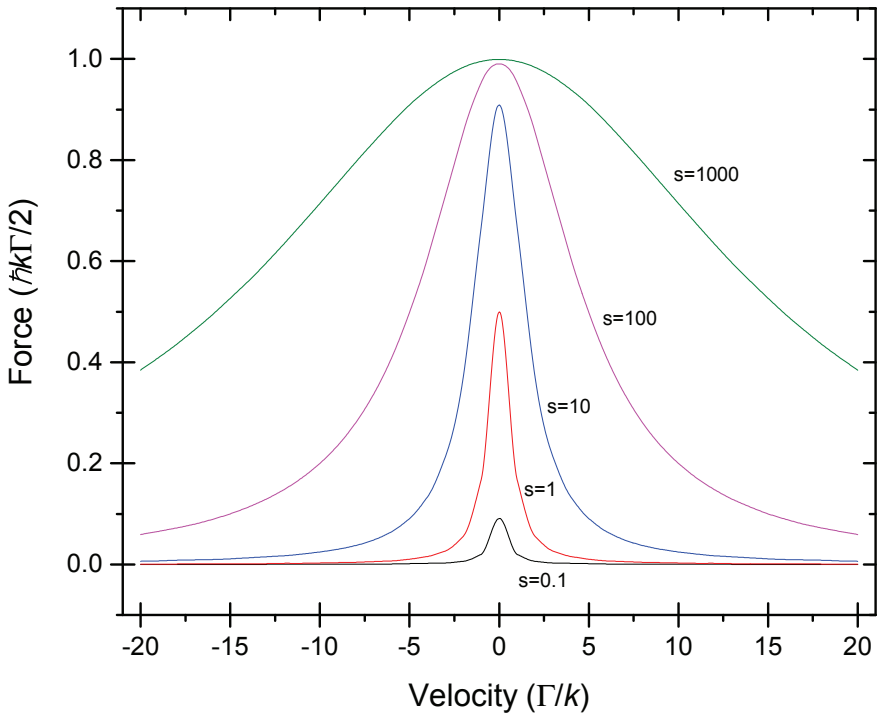

Fig. 1.2: A plot of F_{rad} vs. velocity for a detuning $\delta = 0$. The different values of the saturation parameter, s, ranging from 0.1 to 1000 show the effects of intensity on the width and magnitude of the force. Note that the vertical axis is scaled by units of the maximum radiative force, $F_{rad}^{max} = \hbar k\Gamma/2$.

which shifts the internal energy levels of the atom. For optical fields detuned far from resonance, the energy shift in the ground state is given by

$$\Delta E_g = \frac{\hbar \Omega_r^2}{4\delta}, \tag{1.1.4}$$

where δ is the laser detuning and Ω_r is the Rabi frequency, defined as

$$\Omega_r = -\vec{d} \cdot \vec{E}/\hbar. \tag{1.1.5}$$

Here $\vec{d}$ is the dipole matrix element between the two coupled states and $\vec{E}$ is the external field. The intensity of the external field can be expressed in terms of the Rabi frequency as

$$I = 2I_{sat} \left(\frac{\Omega_r}{\Gamma} \right)^2. \tag{1.1.6}$$

Thus we find the ground-state energy shift is proportional to the laser intensity, I. Introducing spatial variation to the external field intensity therefore introduces spatial variation to the energy shift—i.e., a spatially varying potential energy—which introduces a force, $F = -\nabla U = -\nabla(\Delta E_g)$. For a monochromatic standing plane wave, the intensity is periodic in space: $I = I(z) = I_0 \cos^2(kz)$. From this field we derive a force

$$F_{Dip}(z) = -\nabla \frac{\hbar \Omega_r^2}{4\delta} = -\frac{\hbar \Gamma^2 I_0}{8\delta I_{sat}} \frac{\partial}{\partial z} \cos^2(kz) = \frac{\hbar k \Gamma^2 I_0}{8\delta I_{sat}} \sin(2kz), \tag{1.1.7}$$

as shown in Fig. 1.3.

Unlike the radiative force, we note that the dipole force is not limited by the upper state decay rate of the system. The decay rate, Γ, shows up in the expression for F_{dip}, but only as a metric of coupling strength between the two

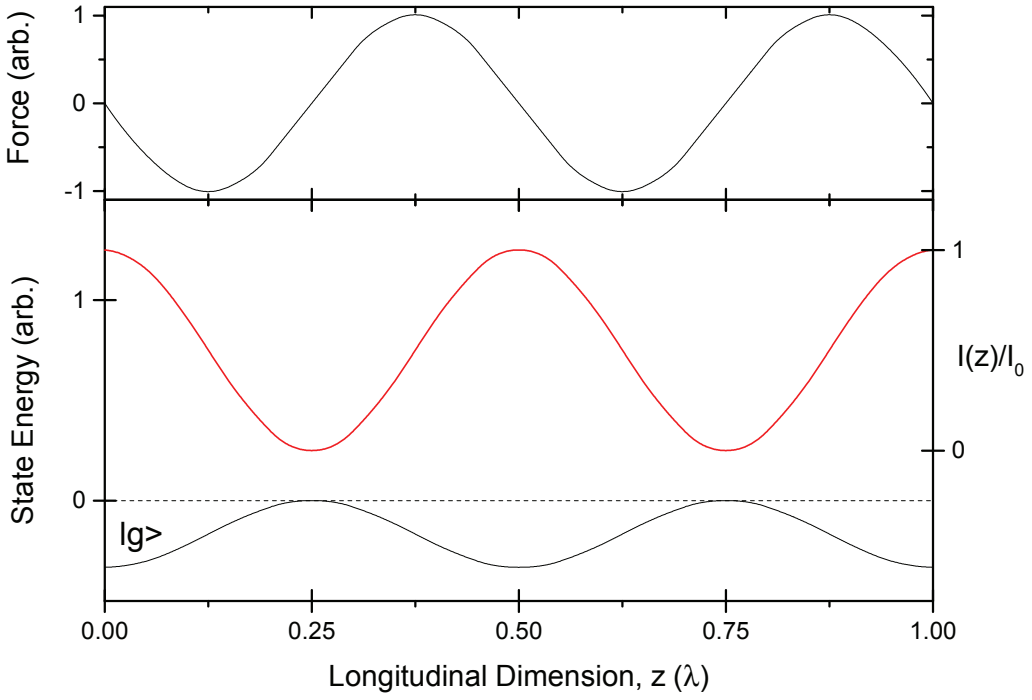

Fig. 1.3: (Top) Plot of dipole force for a red-detuned beam ($\delta < 0$), F_{Dip}, as a function of longitudinal dimension, z, scaled by the wavelength of the dipole force beam. (Middle) Plot of the intensity of the force beam as a function of z and (Bottom) its effect on the energy of the ground-state of a two-level atom.

levels of the system; it does not set any fundamental limits on the system. In fact, there is no saturation limit of any kind explicitly placed on the dipole force. Since the force increases linearly with external field intensity, the magnitude of the force can be set arbitrarily (high or low) by tuning the power of the external field appropriately. There is, however, an implicit limit on the force. As the intensity is increased, the field must remain non-resonant—$|\delta| \gg |\Omega_r|$—but that is not typically a significant experimental concern. The real limitation to the dipole force comes about from the spatial dependence of the force. For a monochromatic standing wave, the intensity varies sinusoidally along the axis of the force. Thus, despite the large peak magnitude of the force, the periodic sign reversal attenuates the integrated momentum change, and makes the average change in momentum zero over a full wavelength. For transverse deflection, this is not necessarily an obstacle as careful placement of intensity nodes can in principle isolate specific regions of force. For laser slowing, however, the interaction length will almost certainly cover several wavelengths of the external field beam, thereby limiting the effects of the force. If, however, the sign oscillations could be rectified the dipole force would have the potential to be an effective slowing force.

One method of rectifying the dipole force uses a second standing wave at a different detuning, i.e. a bichromatic standing wave [10, 25]. The first standing wave exerts a dipole force in the typical sense described above. The second standing wave is at a higher intensity and a different detuning than the first. The second standing wave adds an additional shift to the energy levels of the atom which causes the effective detuning of the first wave to modulate sign over the optical wavelength. By carefully tuning the parameters of this second standing wave, the detuning of the first wave can be made to oscillate in phase with the

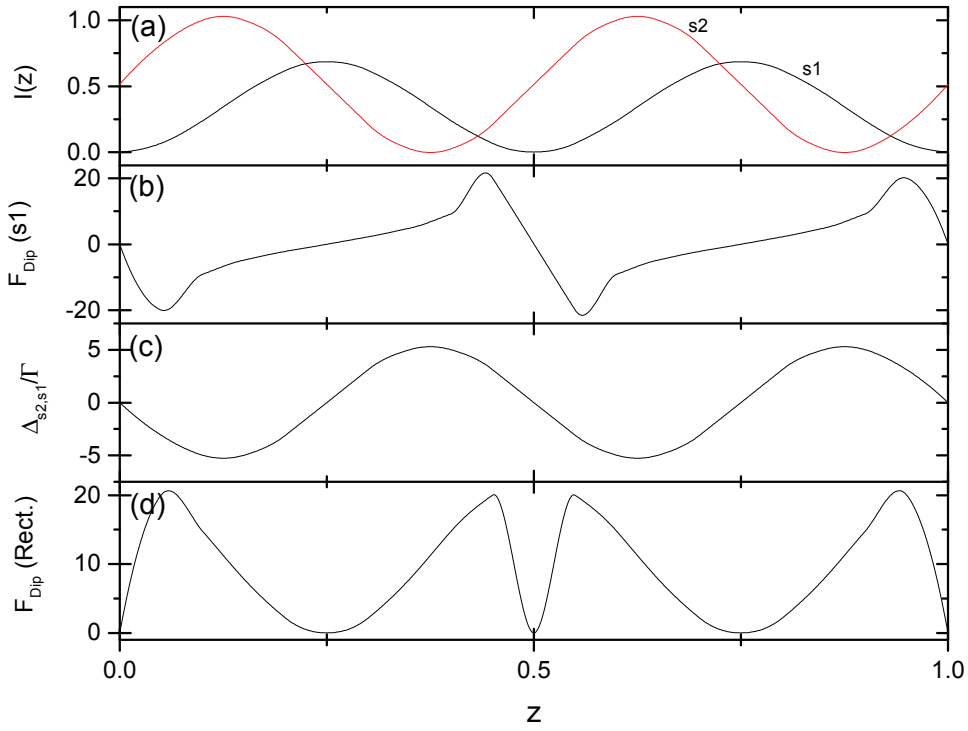

Fig. 1.4: A schematic diagram of the rectified dipole force. (a) The two bichromatic standing wave intensities, s1 and s2, as a function of z, scaled by the wavelength of s1. (b) The dipole force exerted by s1 (in the absence of s2) as a function of z. Note that the force depicted is no longer in the large detuning limit (as we described in 1.1.7). (c) The effective detuning experienced by s1 in the presence of s2. (d) The resulting rectified dipole force caused by the effective detuning of s2 on s1.

dipole force oscillations, thereby generating a positive definite force over several optical wavelengths. A schematic diagram of this force is shown in Fig. 1.4. The specific parameters necessary to generate this force are highly sensitive and, unfortunately, still limit the dipole force to relatively narrow velocity ranges. Thus, while the rectified dipole force does have useful applications, it is still not quite versatile enough to slow atomic beams effectively.

1.1.3 Stimulated Forces

An alternative solution to the spontaneous decay limitation of the radiative force is to change the decay mechanism of the atom. Stimulated forces still rely on the scattering of resonant photons to impart momentum impulses, just like the radiative force, but increase the scattering rate by using stimulated emission rather than spontaneous emission. From our treatment of the radiative force (see sec. 1.1.1), it is clear that stimulated emission for spatially uniform monochromatic beams results in no net momentum transfer. Thus, in order to generate a force via stimulated emission, a more carefully controlled interaction is necessary.

One particular example of a stimulated force is generated via adiabatic rapid passage (ARP). This technique uses frequency-chirped pulses to coherently drive two-level systems between their ground and excited states [26, 27]. For ensembles, careful engineering of the time dependence of pulse intensity and detuning is necessary to maximize the inversion of the system. The ideal parameters can be summarized as

$$\delta_0 \sim \Omega_0 \gg \pi/\mathrm{T}_s \gg \Gamma, \tag{1.1.8}$$

where δ_0, Ω_0, ω_s, and Γ are the chirp amplitude, peak Rabi frequency, pulse repetition rate, and spontaneous decay rate, respectively [26, 27].

Two counter-propagating pulse trains are then used to generate a force. The trains are timed such that a pulse from one direction drives the system into the excited state, followed immediately by a pulse from the other direction which guides the system back to the ground state, as shown in Fig. 1.5. The net result is that for each pulse cycle the atoms experience two impulses in the same direction and are left in the ground state. The rate of momentum transfer is, as alluded to previously, independent of the spontaneous decay rate and is set by the repetition

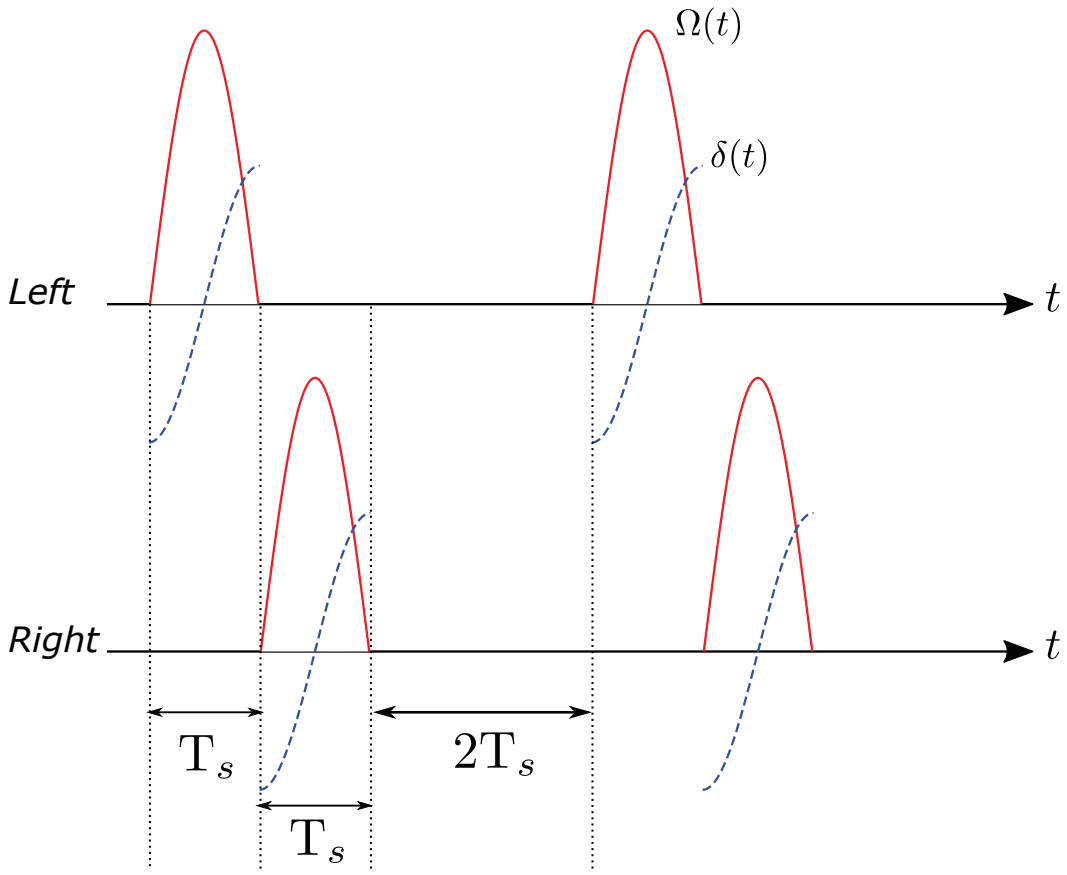

Fig. 1.5: A schematic diagram of the pulse sequencing used to generated a force via Adiabatic Rapid Passage (ARP). Pulse trains from the left and right are sequenced such that pulses from one direction drive the system into the excited state while pulses from the other direction carry it back down to the ground state. The pulses are chirped to coherently control the system's evolution between the ground and excited states and occur at an independently adjustable repetition rate $1/4\mathrm{T}_s$. The force generated by ARP is $F_{ARP} \sim \hbar k/2\mathrm{T}_s$.

rate of the pulse sequence. Thus, for repetition rate $1/4\mathrm{T}_s$ we find the force is

$$F_{ARP} \sim \frac{\hbar k}{2\mathrm{T}_s}. \tag{1.1.9}$$

The magnitude of the force is adjustable by tuning the repetition rate and (with correct choice of parameters) can be made to far exceed the magnitude of the radiative force [26, 27]. In addition, for sufficiently short pulses the system spends only a very short time in the excited state, effectively minimizing the possibility of a spontaneous decay event occurring at all. Similar forces can also be generated using pairs of carefully generated π-pulses such as from a pulsed laser (or other source) [28–30]. This method, however, lacks robustness. Small deviations from an exact π-pulse from either direction will leave the system in a superposition state which will continue to accumulate phase over repeated pulse cycles. If the system accumulates enough phase to fully invert the cycling sequence, the direction of the force will invert as well.

An alternative to ARP, known as the bichromatic force (BCF), takes a simpler approach. First developed as an offshoot of the rectified dipole force, BCF recreates the coherent cycling and increased force magnitude of ARP without the need for careful synchronization of the chirp frequency in each pulse (see chapter 2). It is for this reason that BCF was chosen to be the focus of this dissertation.

1.2 Optical Forces on Molecules

As with many techniques in physics, the successes of optical forces in atomic systems have led to interest in applying them to more complicated systems. The next logical step after atomic species is, of course, molecular species. This step

has, however, proven to be a stumbling block until recently.

The gross internal structure of simple atoms, particularly single-effective-electron atoms, is typically dominated by the electronic energy structure. As such, the density of states is limited, thereby reducing the number of internal states that need to be addressed when attempting to cool the system. For molecules, however, this is no longer the case. Even the simplest diatomic molecule has additional vibrational and rotational degrees of freedom which arise from the relative motion of the nuclei and add to the electronic degrees of freedom. Due to these additional degrees of freedom, the internal structure of molecules contains a vastly greater number of energy states than atomic systems: a dense manifold of sub-states within every electronic state. The increased density of states requires a much more careful approach to direct laser cooling. Through judicious choice of molecular species and careful selection of electronic transition, several groups have managed to slow and even trap various simple molecules including CaF [15, 17], SrF [16, 19, 20], and SrOH [18, 31].

1.2.1 Radiative Force

The primary obstacle to the application of the radiative force in molecules is spontaneous decay. The increased complexity of the internal structure of molecules means that a given atom has a much higher probability of decaying to an optically inaccessible dark state. In atoms, this loss mechanism can usually be attenuated through careful exploitation of selection rules. The increased density of internal states in most molecules, however, means that finding a closed transition can be difficult (if not impossible). If/when closed transitions cannot be found, the other alternative is to close the open decay pathways via repump lasers. Again,

whereas atoms rarely require more than one or two repumps to close extraneous decay pathways, the density of states in molecules means that closing molecular transitions could require driving the system at literally dozens of discrete frequencies simultaneously in order to address every open pathway. The plethora of decay pathways means that most molecules can only be excited a few times before they inevitably decay to a dark state and are lost from the system. This inherently sets a limit on the number of momentum impulses that can be applied to any given molecule via the radiative force.

Recently, several groups have been able to achieve radiative force slowing of molecules [15–20]. By very carefully choosing their molecule, they were able to find nearly-closed transitions thereby limiting the number of repump frequencies needed. Even in these cases, however, because of the sheer number of decays needed to slow the molecular beam, repumps were needed to address decay paths with branching ratios down to order 10^{-4} [17]. An example of the transitions used by [15] to radiatively slow CaF is shown in Fig. 1.6.

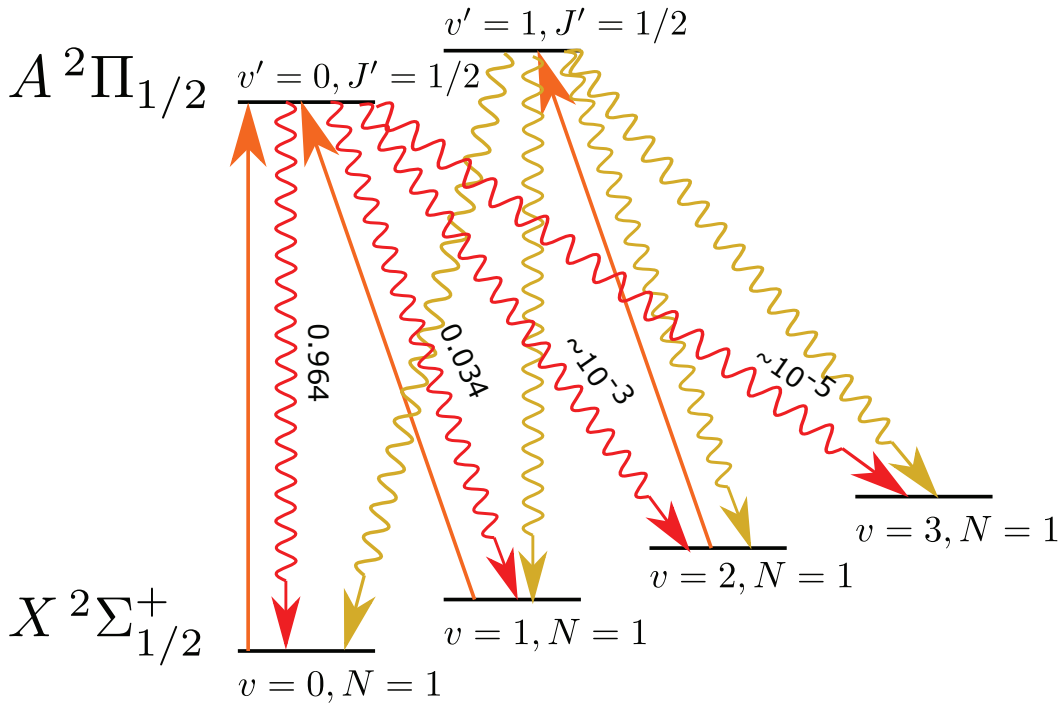

Fig. 1.6: A diagram of the transitions used by [15] to radiatively slow CaF. Orange solid lines represent the primary driving frequencies, each of which was further broadened to a linewidth of ∼400 MHz. The wavy lines represent the important decay pathways of the molecule, numbers next to them indicate the Franck-Condon factors of each decay pathway.

Chapter 2

Bichromatic Force Theory

The bichromatic force (BCF) was first theorized in the 1980s as an extension of the rectified dipole force (see sec. 1.1.2) and has since been put to use in slowing a variety of atomic species including Rb, Cs, Na, and He*. Following from its dipole force origins, the BCF makes use of a two-color standing wave to coherently transfer momentum from a system into the surrounding light field [4–7, 13, 32–34]. As is the case for the rectified dipole force, the presence of one color Stark shifts the energy levels of the system into resonance with the secondary frequency. As the system evolves, the two frequencies trade off roles, thereby increasing the momentum transfer to the system.

The BCF can also be thought of in an alternative, equivalent picture as a pair of counterpropagating pulse trains, as shown in Fig. 2.1. The counterpropagating trains are comprised of the beat notes formed by combination of two beams which have been symmetrically detuned from a central resonance. Tuning the intensity of the counterpropagating trains allows each beat pulse to act as a π pulse. By properly sequencing these pulses, the system can be excited from one direction, and immediately stimulated into emission from the other. This scheme affords us a basic form of coherent control over the system, allowing for the transfer of momentum into or out of the system, depending on the parameters of the pulses.

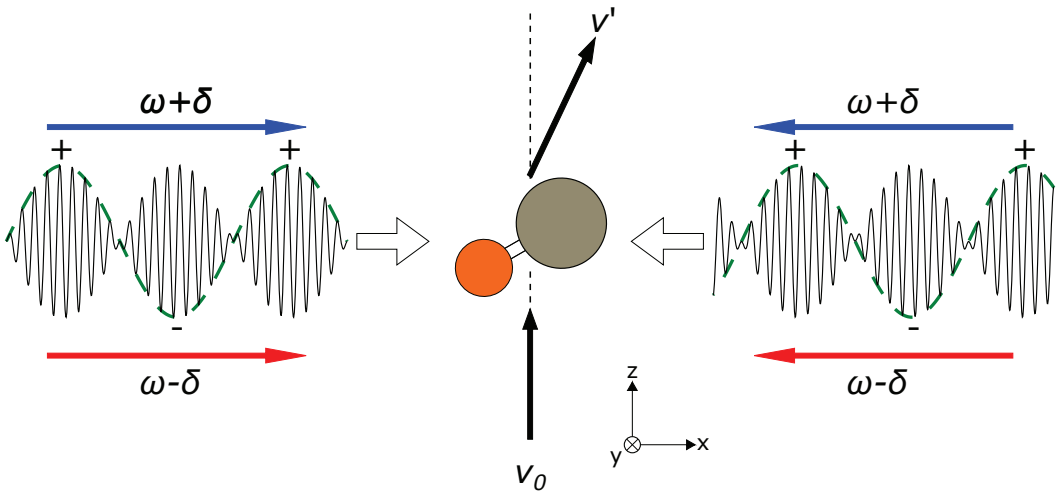

Fig. 2.1: The BCF is generated by counterpropagating trains of beat notes, generated by the combination of two symmetrically detuned frequency components. The beat notes, which act as π-pulses, coherently transfer momentum in or out of the system at a repetition rate set by the bichromatic detuning, δ. With a proper choice of δ, this rate can be made much larger than the upper state decay rate of the system, Γ.

We can study the momentum transfer process in a number of ways. For atomic systems, we use two models to describe the dynamics: the π-pulse model [14], which provides an intuitive understanding of the dynamics, as well as reasonably accurate qualitative predictions; and detailed numerical solutions to the Optical Bloch Equations (OBEs) [7–9, 35], which provided accurate quantitative information. For molecular systems, the dynamics of the system are explored quantitatively via numerical solutions of the Liouville-von Neumann equation with dissipation terms, encapsulating the full multi-level density matrix dynamics [36, 37]. The results of the multilevel simulations were found to be qualitatively consistent with the two-level solutions, with numerical scaling corrections needed to achieve quantitative agreement between the models.

2.1 π-Pulse Model

The simplest (and potentially most useful) picture to consider when discussing the behavior of the BCF is the π-pulse model [14]. In this approximation, the BCF is composed of two counterpropagating trains of isolated π-pulses. A π-pulse approaching from one side first excites the system, driving all of the population into the excited state. A second π-pulse immediately approaches from the other side and stimulates the system to emit, returning the population to the ground state. This scheme is shown in Fig. 2.2. The excitation pulse transfers to the system one unit of momentum, $\hbar k$, in the direction of the pulse's travel. The de-excitation pulse stimulates emission in its direction of travel, thereby transferring to the system one unit of momentum, $\hbar k$, in the direction opposite to its travel. By alternating the arrival direction of the excitation and de-excitation pulses, the two momentum transfers are made to be parallel and, in the absence of

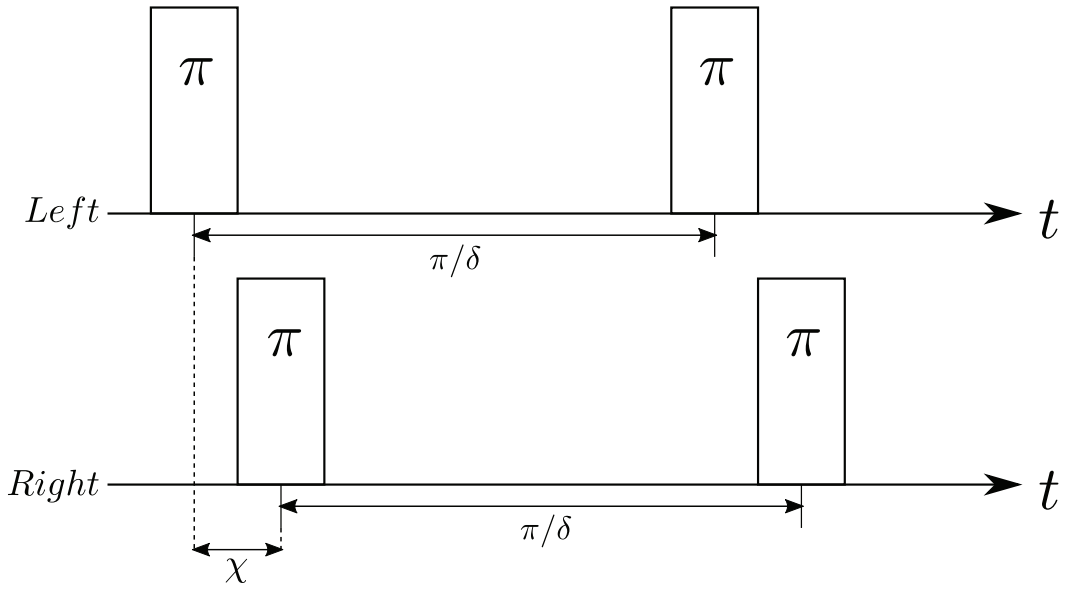

Fig. 2.2: The basic scheme of the π-pulse model of the BCF. Pulses from two opposite directions are sequenced such that pulses from one direction excite the system while pulses from the other stimulate emission and return the system to the ground state. By changing the relative timing of these pulses, the force can be made to act in either direction. This model provides an intuitive qualitative description of the BCF, but more complete models are needed to draw quantitative conclusions.

spontaneous emission, the entire system will experience a momentum transfer of $2\hbar k$ per pulse pair. The relative timing of the pulse arrivals, and thus the direction of the momentum transfer, can be controlled. If the first pulse (excitation) travels along $+x$, the system will experience $2\hbar k$ in the $+x$ direction; if the first pulse travels along $-x$ the system will transfer $2\hbar k$ in the $-x$ direction. By changing the timing between the incident pulses—or, equivalently, by adjusting the phase between the counterpropagating pulse trains—the direction of the force can be reversed.

Based on this model, we observe that the system spends the majority of its time in the ground state. The only time it is in the excited state is the brief moment after the absorption of the excitation pulse and before the arrival of the de-excitation pulse. It remains in the ground-state between pulse pairs. Taking into account the effects of spontaneous decay, we find that the system spends 25% of its time in the excited state, thus, statistically, 25% of the population will decay during this period and end up cycling in the wrong sequence. This results in a reduction in the net momentum transfer as the reverse-cycling causes an oppositely-directed force. Weighting these forces by their respective populations we find the net momentum transfer becomes $(3/4)(2\hbar k) + (1/4)(-2\hbar k) = \hbar k$ per pulse pair cycle [9]. By similar logic, we can also predict the systems average excitation fraction. Recalling that 3/4 of the population will cycle correctly, i.e. spend 1/4 of their time in the excited state, and 1/4 will cycle incorrectly, spending 3/4 of their time in the excited state, we find that the average excitation fraction is simply (3/4)(1/4)+(1/4)(3/4)=3/8=37.5% of the time [38].

With careful treatment, it is possible to extract further properties of the BCF from this simple treatment such as its velocity width and the π-pulse intensity condition. These conclusions, however, tend to be more qualitative than quantitative in their description. For a more exhaustive treatment of this model see [12, 14, 39]. For our purposes, the π-pulse model serves as an intuitive model of the behavior of the BCF but is not typically used to draw quantitative conclusions about the behavior of the force.

2.2 Optical Bloch Equation Solutions

In order to draw quantitative conclusions about the dynamics of the BCF, a more complete model than the π-pulse model must be used. Previous studies by our group [8, 9, 40] (and others [7, 41]) have made use of doubly-dressed-state atom models, but we found that direct numerical simulation of the system provided a more complete picture of the internal dynamics. The optical Bloch equations (OBEs) [35]—which are equivalent to the Liouville-von Neumann equation of a two-level atom—are solved numerically for a bichromatic field in the rotating wave approximation. In the OBE representation, the state of the system is represented by the orientation of a unit vector (the Bloch vector). The components of the Bloch vector—$u(t)$, $v(t)$, and $w(t)$—are given by

$$\begin{aligned} u &= \rho_{12} + \rho_{21}, \\ v &= i(\rho_{12} - \rho_{21}), \\ w &= \rho_{22} - \rho_{11}. \end{aligned} \tag{2.2.1}$$

where ρ_{ij} are elements of the density matrix. The elements ρ_{11} and ρ_{22} describe the fraction of the system in the ground and excited states, respectively, while the elements ρ_{12} and ρ_{21} describe the coherence between the states. Note that in this form $w = -1$ corresponds to a pure ground-state system and $w = +1$ corresponds to a pure excited-state system. The OBEs are solved in the form

$$\begin{aligned} \frac{du}{dt} &= -\Gamma u - \delta_{\text{asym}} v - \text{Im}\left[\Omega(t)\right] w \\ \frac{dv}{dt} &= \delta_{\text{asym}} u - \Gamma v + \text{Re}\left[\Omega(t)\right] w \\ \frac{dw}{dt} &= \text{Im}\left[\Omega(t)\right] u - \text{Re}\left[\Omega(t)\right] v - 2\Gamma(w+1), \end{aligned} \tag{2.2.2}$$

where Γ is the excited state lifetime and $\Omega(t)$ is the time-dependent Rabi frequency. The parameter δ_{asym} is the detuning between the BCF optical carrier frequency and the resonant frequency of the system. The time-dependent Rabi frequency for the two-color BCF field is given by

$$\Omega(t) = 4\Omega_r \left[\cos(\chi/2)\cos(\delta t)\cos(kx) + i\sin(\chi/2)\sin(\delta t)\sin(kx)\right], \tag{2.2.3}$$

where χ is the phase between counterpropagating beat notes, δ is the bichromatic detuning, and Ω_r is the Rabi frequency amplitude (as defined in Eq. 1.1.5). We make the substitution $x = vt$ and use this to obtain the velocity dependence of the force. The force is calculated from the system dynamics solutions using Ehrenfest's theorem. The simulations are run using programs written in Mathematica and Fortran. The two different algorithms allows us to verify the validity of the solutions and to independently optimize different programs for different tasks.

Through our study of the numerical simulations, we are able to explore both the velocity-dependent behavior of the force as well as the time-evolution of the system. Using these insights, we optimize the parameters of the force, namely relative phase between pulses, χ, and beam component intensity, Ω_r, and observed the effects on the excited-state character of the system. The flexibility of the model also allows us to explore the effects of experimental non-idealities, namely imbalance between pulse intensities.

It was through our study of the dynamics that we discovered an important factor in the robustness of BCF against non-ideal parameters [38]. At zero velocity, the BCF field is real. As a result, for a system starting in the ground state, the evolution of the Bloch vector (u, v, w) reduces from a 3D to a 2D domain—i.e. u is identically 0, thus the Bloch vector remains confined to the v/w plane. This makes

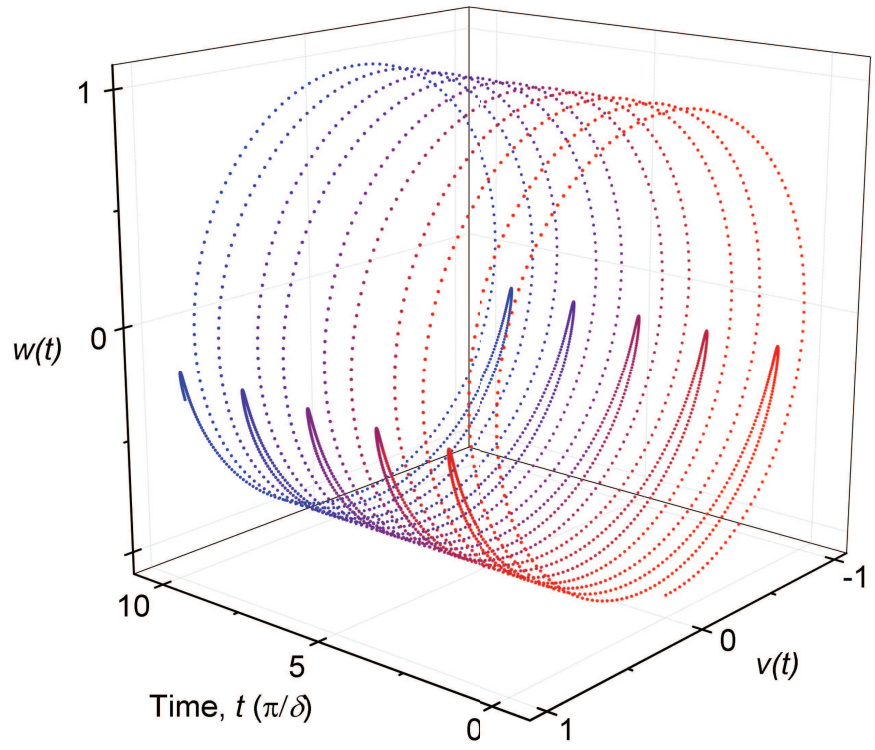

(a)

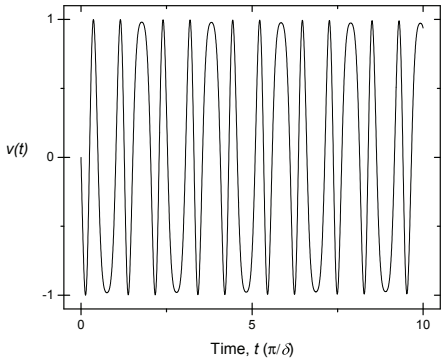

(b)

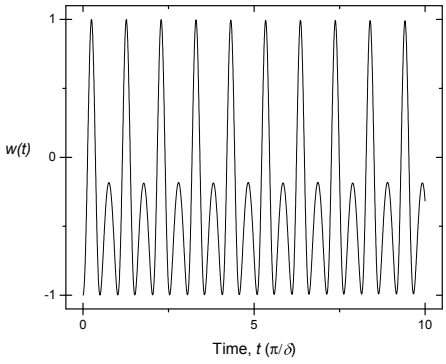

(c)

Fig. 2.3: (a) A Bloch vector trajectory plotted under optimal BCF conditions for a system at velocity=0, such that the Rabi frequency $\Omega(t)$ is real. Under these conditions the Bloch vector component $u(t) = 0$ identically. We plot the remaining components $v(t)$, $w(t)$ as a function of time and observe the evolution of the Bloch vector under a BCF field. Note the reversal of the direction of precession which occurs between BCF pulses. The subplots (b) and (c) are projections of $v(t)$ and $w(t)$, respectively.

it possible to intuitively visualize the time evolution of the system by plotting the trajectory of $v(t)$ and $w(t)$ with respect to time. An example of this is shown in Fig. 2.3. An analysis of this trajectory shows that the BCF does not simply accumulate phase with time, but rather alternatively wraps and unwraps phase over the duration of its evolution. This oscillation of rotation direction prevents phase over-shoots and under-shoots—which result from imbalanced or otherwise non-ideal pulses—from accumulating and upsetting or reversing the evolution of the system (and thus reversing the direction of the force). This phase reversal is due to the oscillating sign of the beat note's sinusoidal envelope, as shown in Fig. 2.1. The phase of each beat pulse from a given train alternates between $(+)$ and $(-)$ according to the sign of the envelope pulse. As this phase alternates, so too does the direction of the system's evolution about the Bloch sphere. This leads to a 4π periodicity, always ending in the starting state of the system (typically the ground state). Regardless of the exact phase sequencing, either $(+)(+), (-)(-)$ or $(+)(-), (-)(+)$, we find that after four pulses we always return to our initial system configuration, as illustrated by Fig. 2.4, thereby preventing dephasing from upsetting the system. This robustness is an important practical feature of the BCF.

2.3 Density Matrix Solutions

To explore the dynamics of the BCF in molecules, we have to further evolve our treatment of the system. The two-level approximation of the OBEs is insufficient to describe the internal dynamics of a molecule. Thus, a multi-level simulation was developed [36, 37] in order to model the more complicated internal structure of CaF. A program was developed in Mathematica to numerically

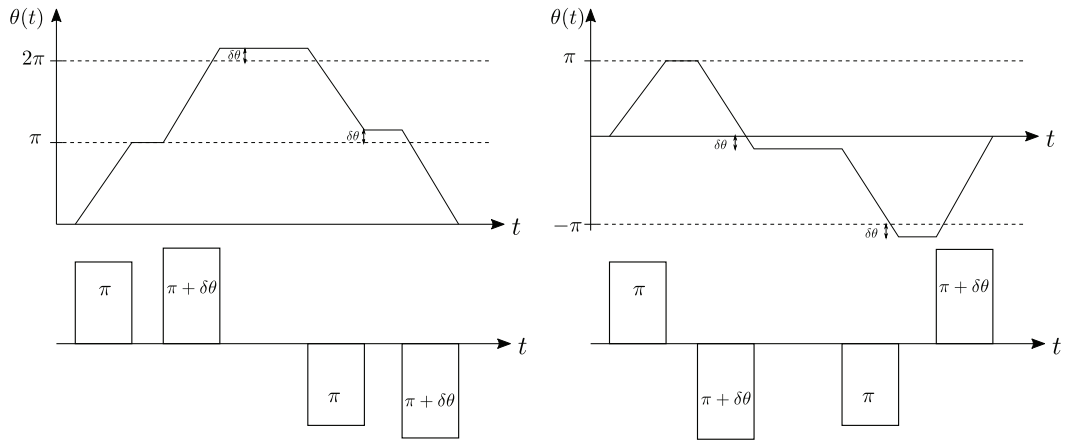

Fig. 2.4: The 4π periodicity of the BCF cycling gives rise to a robustness against imbalance between adjacent pulses. Shown here in the π-pulse model, the oscillating phase of the beat envelope (see Fig. 2.1) changes the direction of propagation about the Bloch sphere, i.e. alternately adds and subtracts phase rather than strictly adding it. Because of this oscillation, phase does not accumulate over time, preserving the correct cycling sequence within the system.

solve the Liouville-von Neumann equation for a bichromatic driving field using the rotating wave approximation. For density matrix ρ, defined as

$$\rho(t) = |\psi(t)\rangle \langle\psi(t)| = \sum_{i,j} \rho_{ij}(t) |i\rangle \langle j| \tag{2.3.1}$$

with state populations ρ_{ii} and coherences ρ_{ij}, the evolution of the system is given by

$$i\hbar \frac{d\rho}{dt} = [H, \rho] + i\hbar \frac{\partial \rho}{\partial t}, \tag{2.3.2}$$

for Hamiltonian, H. These density matrix calculations contain the full dynamics of the multi-level system and take into account couplings between all of the excited and ground states (see [36, 37] for details). In order to account for the different coupling strengths between states, we redefine the Rabi frequency amplitude as

$$\Omega_r^{ij} = \frac{E_0}{\hbar} \langle i| \hat{d} \cdot \hat{\epsilon} |j\rangle , \tag{2.3.3}$$

where E_0 is the amplitude of the external field, $\hat{\epsilon}$ is the polarization unit vector for the external field, and $\hat{d}$ is the dipole operator. We also define the total Rabi frequency for a given excited state as

$$\Omega_r^i = \sqrt{\sum_j (\Omega_r^{ij})^2}. \tag{2.3.4}$$

For our particular system, we find that the total Rabi frequency is the same for every excited state (see Sec. 4.3), $\Omega_r^i = \Omega_r^j$ so that we can ignore the superscripts and simply consider the total Rabi frequency amplitude, Ω_r. The program also includes simulation of a magnetic remixing field that is used in the experiment. The field is necessary to allow transitions which can remix molecules lost to dark

ground-state hyperfine levels. There are further provisions in the code for the inclusion of repump lasers [36], but since they are not necessary for the nearly-closed BCF transition we have chosen, they are omitted for all of the calculations performed in this dissertation.

Just as in the two-level case, this program is used to re-optimize the force parameters for the new system including relative phase, χ; Rabi frequency, Ω_r; magnetic field strength, B; magnetic field angle, θ_{BE}; and central resonance detuning, δ_{asym} [36, 37]. After the force had been fully optimized, the program was modified to explore the effects of asymmetric non-idealities on the force. In particular, the effect of imbalance between the counterpropagating pulse intensities is studied across a variety of force conditions. Generally, we note qualitative agreement between the two-level and multi-level calculations. The sensitivity to imbalance and the velocity-width of the forces in particular show close agreement. The overall magnitude of the forces, however, differ by nearly an order of magnitude due to the presence of many states in the molecular system.

Due to the increased complexity of the multi-level system, it is no longer possible to visualize the evolution of the system in the intuitive way it was done for the two-level case. Despite this unfortunate shortcoming, we still perform studies of the average excited state character of the system. The average steady-state excited-state fraction is computed and compared to the two-level case [37].

2.4 Bichromatic Force Properties

Most of the qualitative properties of the BCF can be deduced directly from its simplest model: the π-pulse model. For quantitative properties, however, numerical models are necessary to unpack the complex dynamics of multi-level

Table 2.1: A brief summary of some of the key features of BCF as found in two-level and multilevel systems.

Property	Two-Level Model Value	Multilevel Model Value
Optimum Ω_r	$\sqrt{3/2}\delta$	$\sqrt{3/2}\delta$
Velocity Range	$\sim \delta/k$	$\sim \delta/2k$
Force Magnitude	$\hbar k\delta/\pi$	$\sim (1/5)\hbar k\delta/\pi$

systems and what effect they have on the characteristics of the BCF. A summary of some of the key properties of BCF are summarized in Table 2.1.

2.4.1 General Characteristics

The conditions for optimization remain nearly the same between the atomic and molecular cases. The force in both cases varies periodically with the relative phase between beat pulses: maximizing at $\chi = 45^o$, vanishing at $\chi = 90^o$, inverting at $\chi = 135^o$, and so-on, repeating for phases through at least $\chi = 270^o$ (the highest phase tested). This is shown clearly in Figs. 2.5(a)-(c). The phase between beats is independent of the internal structure of the system and is only a property of the external field, which is the same in both cases. Thus, the recurrence of this particular dependence for the molecular case is natural. A similar system independence is also seen in the dependence on external field intensity. With an important caveat (see Sec. 2.4.2), the intensity dependence for the BCF for the atomic case applies also to the molecular case. Namely, at a fixed bichromatic detuning, δ, the force shows a strong non-linear dependence on intensity with a peak at Rabi frequency given by

$$\Omega_r = \sqrt{3/2}\delta, \tag{2.4.1}$$

dropping off sharply for deviations away from this value. Figure 2.6 shows this relationship for a multilevel system at $\delta = 30\Gamma$ and $\chi = 45^o$.

Many of the general characteristics of the BCF from simpler models also carry over directly into considerations of more complicated systems, i.e. molecules. With another important caveat (see Sec. 2.4.2), the magnitude of molecular BCF scales linearly with detuning [36], just as it did for atomic systems [4, 8] (assuming that Ω_r is increased proportionally as well). The constant of proportionality does change, however. In the two-level case, the optimized BCF scales according to $F_{2LA} = \frac{\hbar k\delta}{\pi}$ with a velocity width that scales as $\Delta v_{2LA} \sim \delta/k$ [4, 8, 32, 34]. In molecular systems, the optimized force magnitude is reduced by roughly a fifth to $F_{MLV} = 0.1992\frac{\hbar k\delta}{\pi}$ [36], which is roughly commensurate with the ratio of degeneracies in the excited-state to the total system. As for velocity width, the molecular case also seems to scale roughly as $\Delta v_{MLV} \sim \delta/k$ [36], but the softening of the edges of the force profile from the nearly top-hat shape of the force profile for the two-level case makes this proportionality slightly harder to determine precisely. These relationships can be seen in Figs. 2.8(a) and (b) for force magnitude and velocity width, respectively. Despite the reduction in force magnitude, as illustrated in Fig. 2.7, the multi-level BCF can still produces a force many times stronger than the radiative force with a proper choice of detuning, δ.

Somewhat surprisingly, the multi-level case was observed to be surprisingly robust against imbalance between pulses. The increased complexity of the molecular system would have seemed to make it more susceptible to perturbations to the BCF cycling. However, the density of states seems to provide somewhat of a buffer against interruptions. Comparison of the two models under left-right intensity imbalance, see Fig. 2.9, shows that the multi-level model actually has

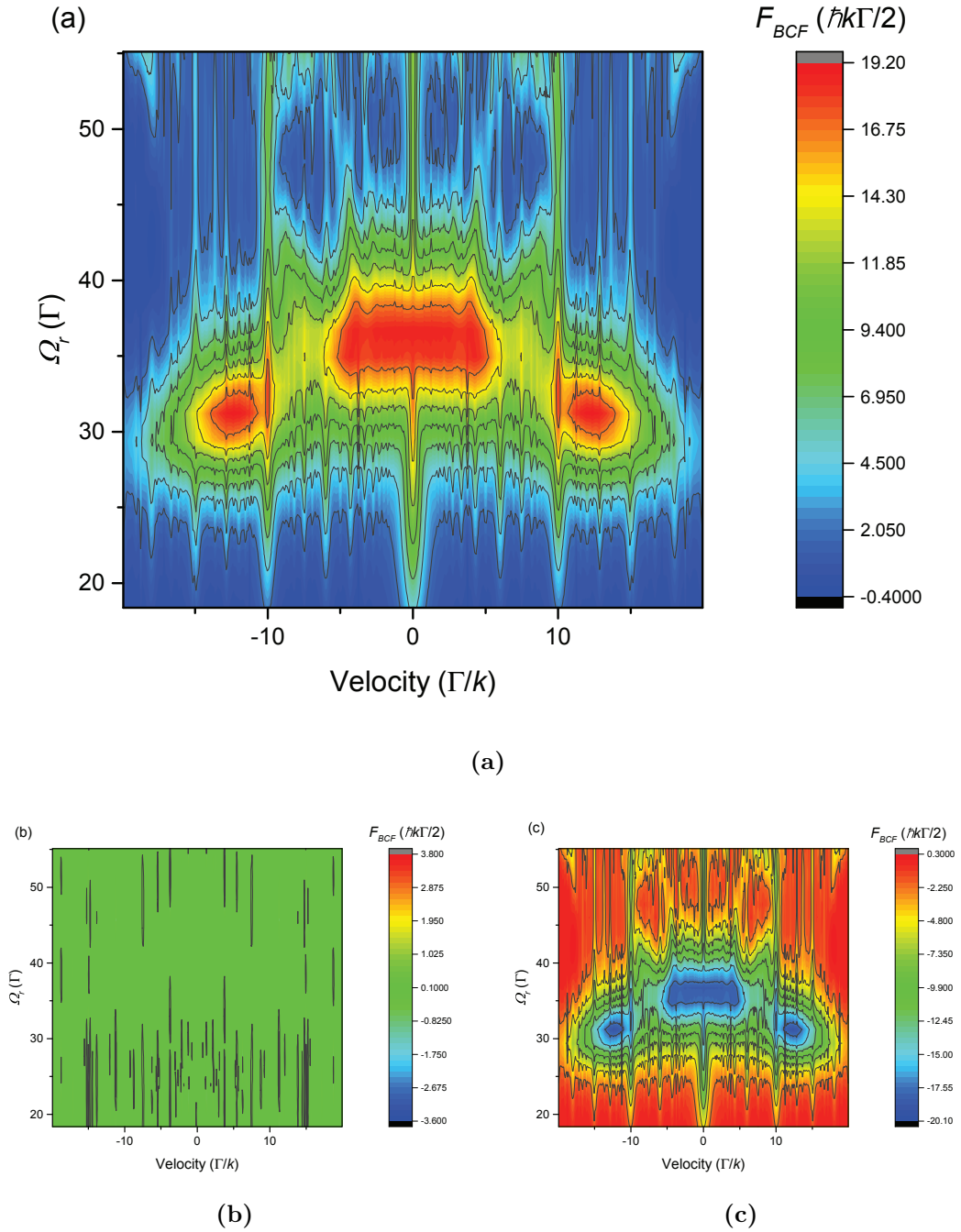

Fig. 2.5: Two-level model simulations of BCF as functions of velocity and Ω_r at $\delta = 30\Gamma$ for phases (a) $\chi = 45^o$, (b) $\chi = 90^o$, and (c) $\chi = 135^o$. Note the color inversion between (a) and (c) which have equal magnitude forces, but are oppositely directed. The force is maximized at $\Omega_r = \sqrt{3/2}\delta$ and shows strongly non-linear behavior under deviations from this value.

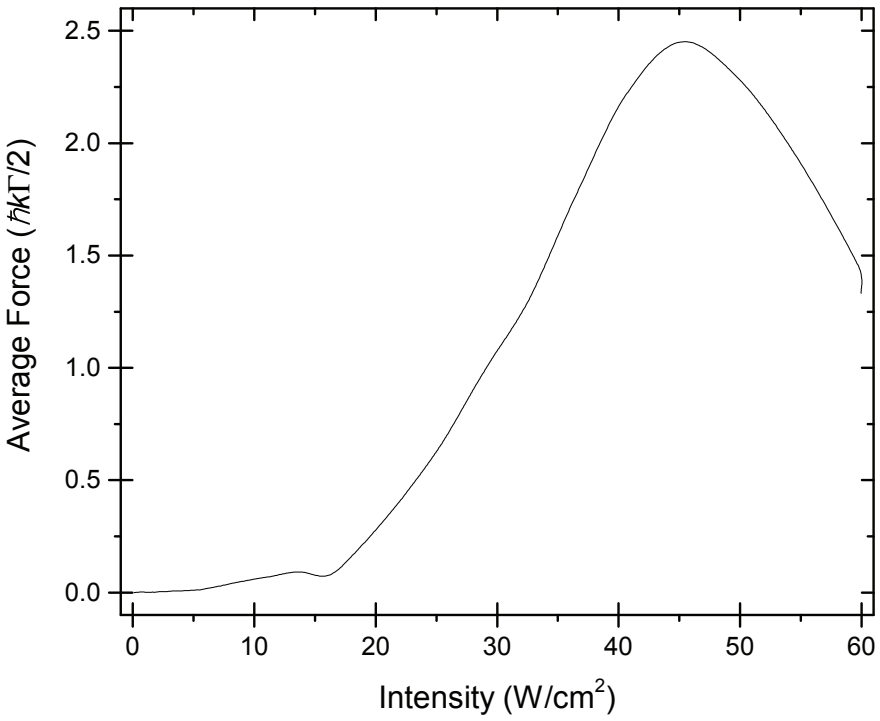

Fig. 2.6: The average force near zero velocity as a function of intensity for BCF with $\delta = 30\Gamma$ at $\chi = 45^o$. The force rises sharply to a peak at 45.2 W/cm^2 before dropping off just as sharply for higher intensities. The Rabi frequency at 45.2 W/cm^2 corresponds to the condition $\Omega_r = \sqrt{3/2}\delta$ (see Eq. 2.4.1).

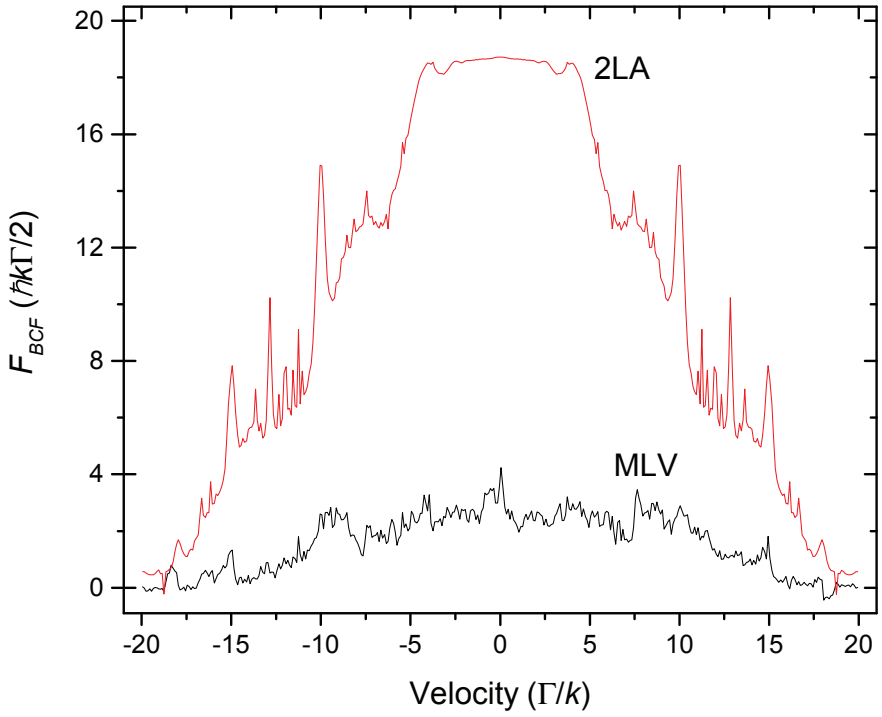

Fig. 2.7: A direct comparison of force profiles computed from the two-level (2LA) and multilevel (MLV) models. Both force profiles shown were computed for $\chi = 45^o$ and at $\delta = 30\Gamma$ with $\Omega_r = \sqrt{3/2}\delta$. The vertical scale for both profiles is in units of the saturated two-level radiative force, $\hbar k\Gamma/2$.

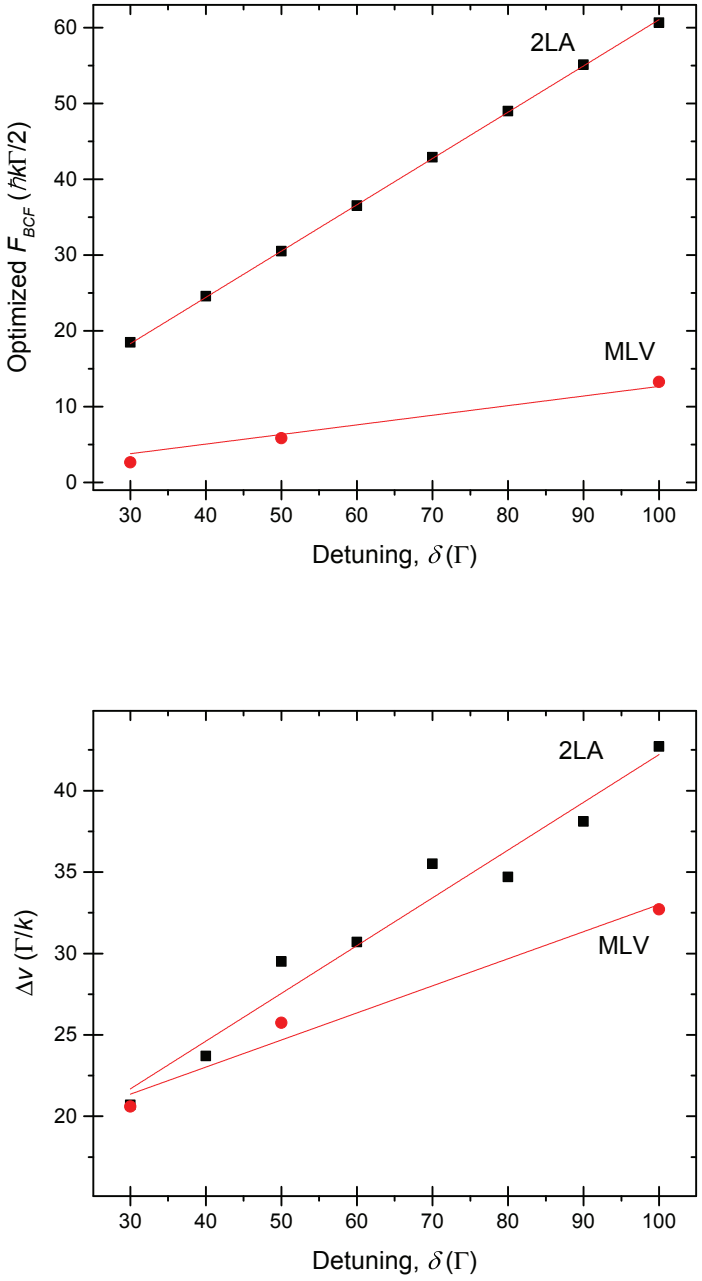

Fig. 2.8: The BCF force magnitude and velocity width calculated via two-level and multilevel models as functions of detuning for $\chi = 45^o$. At each detuning, the Rabi frequency was set to the optimal $\Omega_r = \sqrt{3/2}\delta$ and the results computed from the calculated force profile. The relationships are linear in each case, but the constants of proportionality change from the two-level to the multilevel system.

some enhanced resistance to asymmetric pulses for mid-range imbalances. Previous studies of imbalance in the two-level system have shown that sensitivity to imbalance increases with detuning. This was expected to continue in the multi-level case as well, but the enhanced robustness shown at $\delta = 30\Gamma$ may suggest that this is an avenue worth further study.

The excited-state fraction for the two-level atom is computed to be 41%, which is consistent with the simple approximation of 38% predicted by the π-pulse model [38]. Interestingly, the excited-state fraction is notably lower in the multi-level case than in its simplified counterpart. The average excited-state fraction for the molecular case was calculated to be only 16% [37]. This is likely due to extra time spent in dark hyperfine ground states. The two-level system has nowhere to hide its ground-state population: all of it gets cycled from the ground to excited state and back during each pulse sequence. The dark ground states in the multi-level system, however, provide a ground-state "reservoir." The presence of these states will tend to increase the average time spent in the ground state as individual molecules are cycled amongst the ground-state levels until they return to an optically accessible one.

2.4.2 Detuning Regimes

The behavior of the BCF relies principally on the properties of the external field. As a result of this, most of the optimization conditions and properties of the BCF are independent of the internal properties of the system to which the BCF is applied. The one vital exception to this independence is the detuning frequency, δ [36]. If δ is comparable to the internal energy splittings of the target system, the coherent cycling of the BCF can be interrupted, causing the force to vanish.

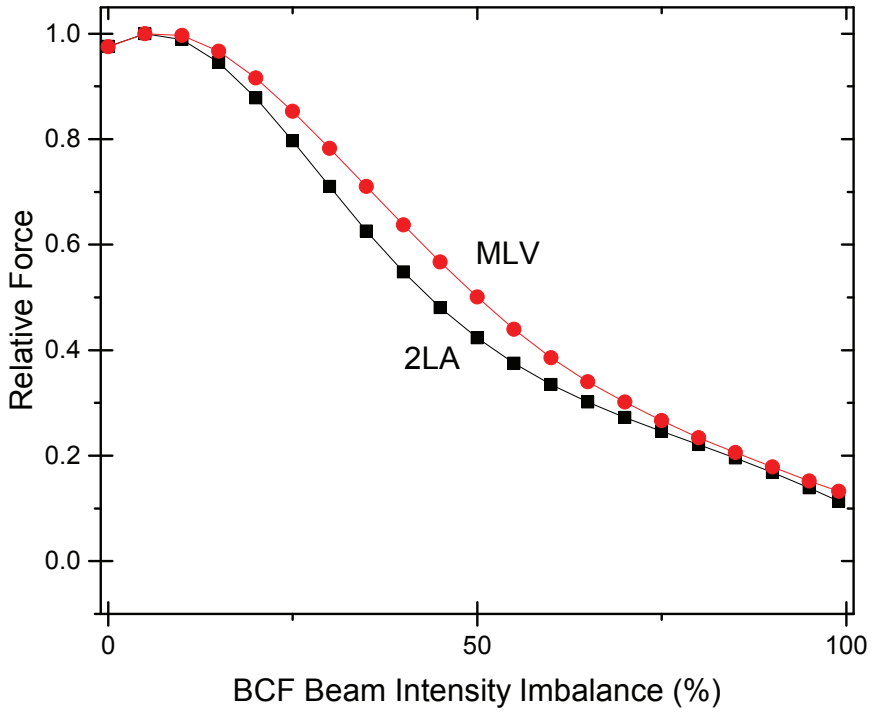

Fig. 2.9: Relative force computed for two-level and multilevel models as a function of left-right intensity imbalance. The left-going intensity was held constant at $\Omega_r = \sqrt{3/2}\delta$, while the right-going intensity was decreased by the indicated percentage from ideal. The forces were computed for $\delta = 30\Gamma$ at $\chi = 135^o$. Note that since the two models produce such widely differing forces, the relative forces (ratio of imbalanced force to balanced force) were used to allow a metric for comparison. The limit of 100% imbalance corresponds to the radiative force from a bichromatic traveling wave.

Hence, we find that for systems with internal structure, properties lose their simple linear scaling with detuning and become divided into three distinct regimes: low detuning, high detuning, and intermediate detuning. This phenomenon is illustrated in Fig. 2.10.

In the low detuning regime, the BCF detuning is small enough that adjacent internal states can be addressed independently [36]. In this case, the BCF can be tuned to act independently on whichever internal state is most convenient, treating it like a two-level system. The optimization parameters for this case are the same as they would be for a similarly structured two-level system: $\chi = 45^o$ and $\Omega_r^0 = \sqrt{3/2}\delta$, where Ω_r^0 refers specifically to the coupling between the two states being addressed. Note that the total Rabi frequency, Ω^{tot} is defined as a quadrature sum of the different state-specific Rabi frequencies and will thus not meet the condition $\Omega^{tot} = \sqrt{3/2}\delta$ [36]. The force produced in this regime still follows the typical velocity width scaling, $\Delta v \sim \delta/k$ (assuming that Ω_r is optimized for the particular bichromatic detuning, δ). The optimized force magnitude, however, scales non-linearly in this regime and is proportional to δ^3 until it levels off and then vanishes as δ approaches the intermediate regime [37].

In the high detuning regime, the internal energy structure is small enough that the levels are effectively blurred together into a single state. The high power of the BCF broadens the states sufficiently that they become a single aggregate state and the system once again becomes an effective two-level system [36]. To some degree, we have always known this was the case and have operated in this regime. Earlier atomic experiments ignored small energy splitting within levels, due to the high BCF power, and treated them as effectively two-level systems. The high detuning regime follows this same scheme, only for a slightly larger energy

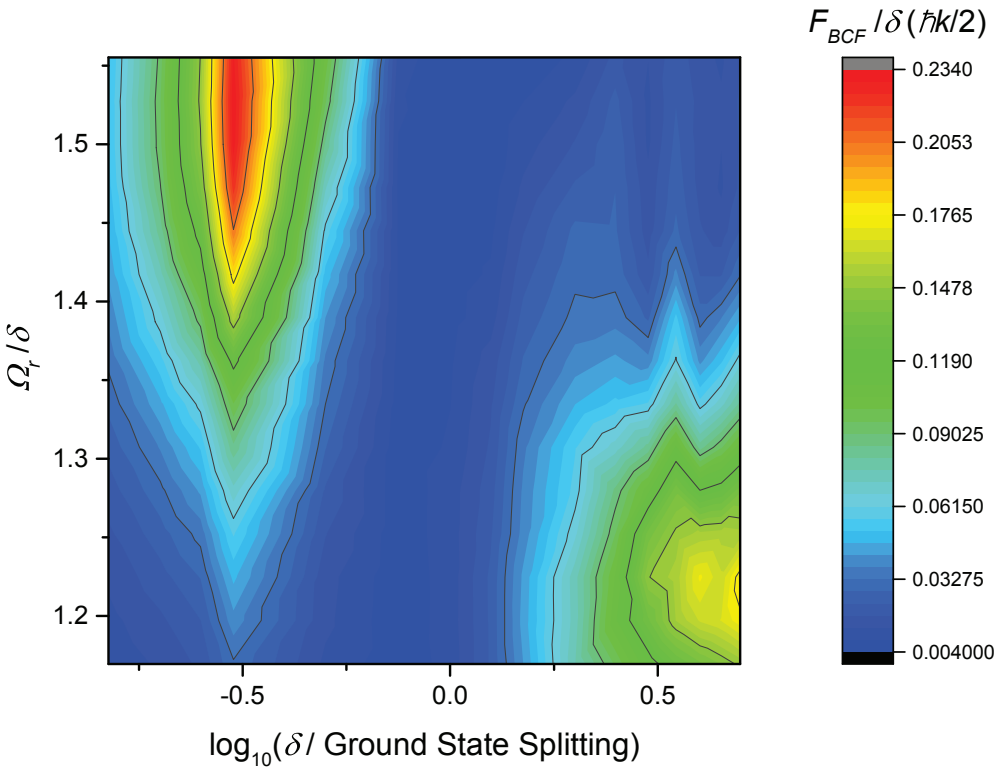

Fig. 2.10: A plot of BCF force as a function of detuning and Rabi frequency for a multilevel system. When the detuning is larger than the ground-state splitting, the BCF behaves as an approximately two-level system, optimizing at $\Omega_r = \sqrt{3/2}\delta \approx 1.22\delta$. When the detuning matches the ground-state splitting, the BCF vanishes, regardless of the driving Rabi frequency. At low detuning, the BCF again behaves as an approximately two-level system, ignoring the additional (off-resonant) ground state. The BCF on this transition is maximized when the particular coupling strength is optimized, i.e. $\Omega_r^{ij} = \sqrt{3/2}\delta$, but the residual coupling to the additional state increases the quadrature sum such that $\Omega_r \neq \sqrt{3/2}\delta$.

interval. As such, the effective two-level system once again follows the two-level system optimization conditions and force scaling: $\chi = 45^o$, $\Omega^{tot} = \Omega_r = \sqrt{3/2}\delta$, $F(\delta) \propto \delta$ (see sec. 2.4.1), and $\Delta v \sim \delta/k$.

As stated previously, in the intermediate regime the force vanishes. The presence of a resonant transition with one of the two frequencies destroys the coherent cycling of the BCF and prevents any force from being generated. It should be noted that the force does not become identically zero, but no significant force can be generated regardless of Rabi frequency [36, 37].

2.4.3 Gaussian Intensity Requirements

As noted in section 2.4.1, the BCF has an optimum intensity at the condition $\Omega_r = \sqrt{3/2}\delta$ and has a highly non-linear dependence on intensity away from this ideal. This leads to an interesting dilemma in the case of a Gaussian laser beam—what is the ideal experimental intensity? Simple intuition may suggest that the peak intensity should be set to the optimal intensity condition, however the sharp non-linearity of the BCF with intensity means that the resulting force will only be optimal at the very center of the beam, where the intensity is peaked and (therefore) optimized. Rather, the overall force output is optimized by maximizing the area of ideal intensity within the beam. For a Gaussian beam, this requires that the peak intensity be set super-optimally, creating a decrease in force at the beams peak intensity. This intentional overshoot produces an annulus within the 2D Gaussian profile at the ideal intensity, as shown in Fig. 2.11. By tuning the area of this annulus, the effective force can be tuned and maximized.

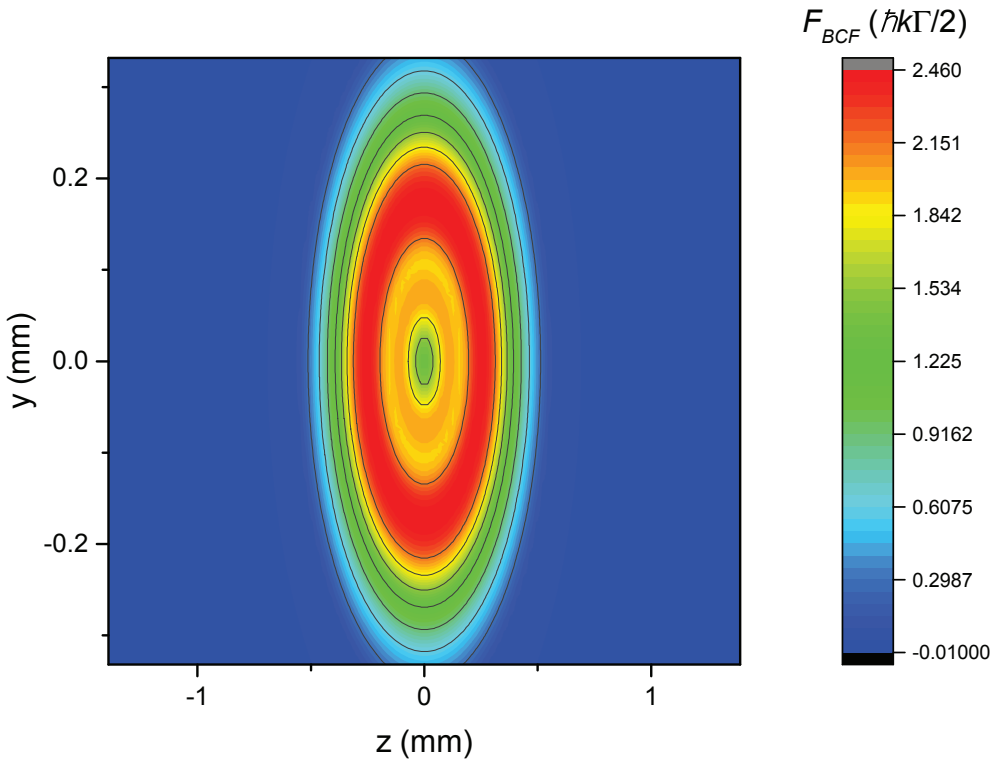

Fig. 2.11: The force vs. intensity profile shown in Fig. 2.6 was mapped onto the intensity profile of our experimental beam to show BCF force as a function of position within the beam. The underlying Gaussian beam has waist radius of 0.7 mm in the z-direction and 0.5 mm in the y-direction. The center of the beam, i.e. peak intensity, has lower force than the surrounding area. This was done intentionally by overshooting the ideal intensity in order maximize the area of the beam at ideal intensity. (Note that the ranges of the z-axis and y-axis are not the same, thus the aspect ratio of the beam appears warped.)

Chapter 3

Deflection Experiment: Molecular Source

The molecular source comprises the largest physical component of the experimental apparatus and also required the most development time. A diagram of the complete system can be seen in Fig. 3.1. For purposes of discussion, the apparatus can be divided into three main components: the vacuum system, the supersonic molecular beam, and the detection infrastructure. In reality these components are all interwoven and work together to generate our molecular sample, but let us first consider the components individually, starting with the vacuum system.

3.1 Vacuum System

The experimental chamber is divided into three sections: a source chamber, an interaction chamber, and a detection chamber. The chambers are discussed in detail below. The source chamber is differentially pumped and maintained at a higher pressure than the interaction/detection chambers which comprise the experimental beam line. A diagram of the complete system is found in Figure 3.1.

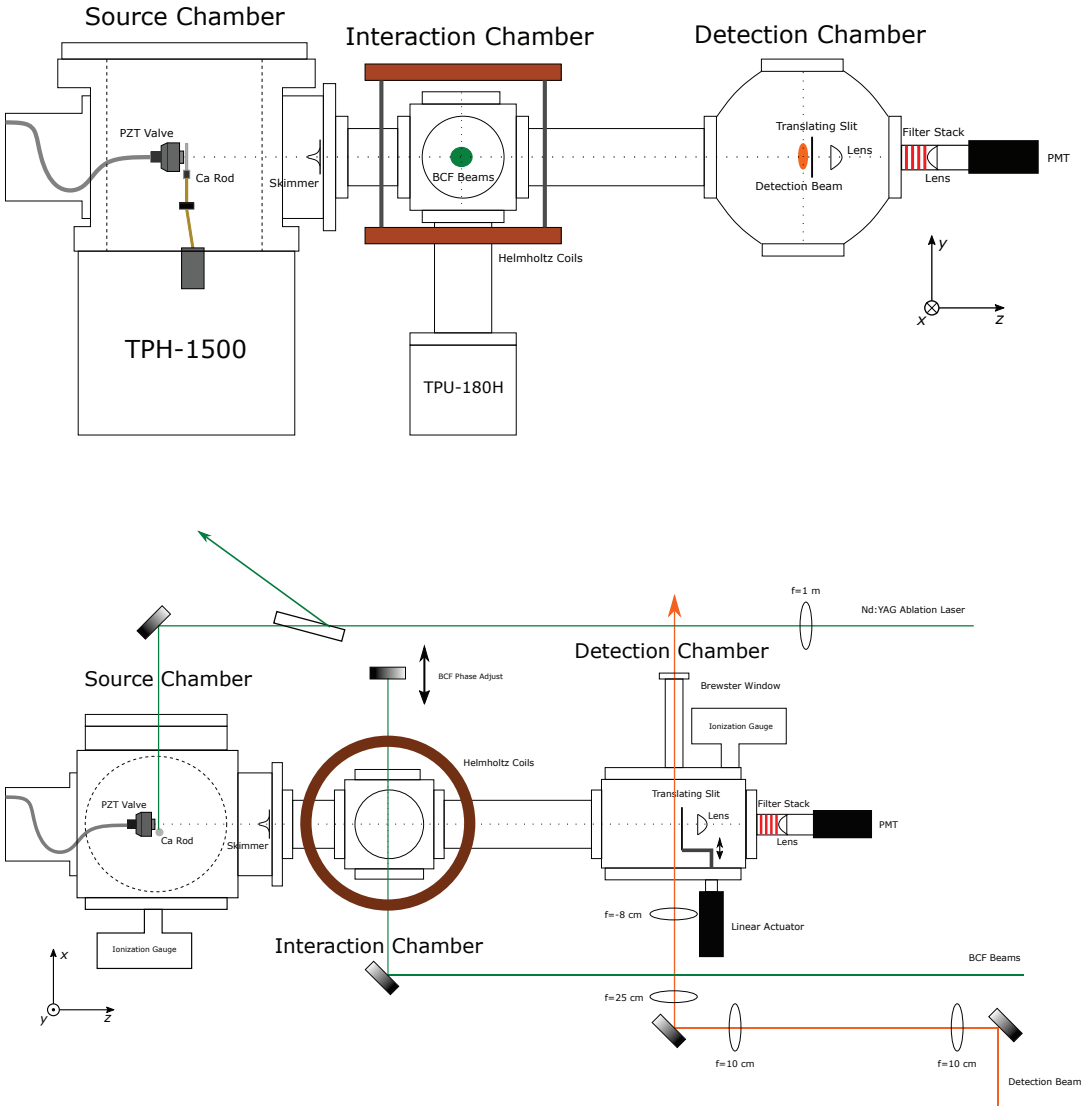

Fig. 3.1: The complete molecular beam vacuum system: side view and top view. The source chamber houses the molecular beam generation apparatus: calcium rod mount, pulsed valve, and vacuum pump. A 1 mm skimmer separates the source chamber from the rest of the beam line, comprised of the interaction and detection chambers. The interaction chamber is a 2.75" spherical cube from Kimball Physics. AR-coated windows along the x-axis allow optical access to the CaF beam for the application of the BCF. Inside the detection chamber a slit is translated along the x-axis to allow measurement of beam deflection along this axis. The chamber has optical access along the x-axis for the LIF excitation beam and along the z-axis for fluorescence collection. Optical access to the y-axis was incorporated to allow for a normalization detector.

3.1.1 Source Chamber

The source chamber is the largest component of the experimental chamber. It is comprised of a custom-sized six-way cross which is re-purposed from an older experiment. The vertical axis is sized for ASA-6" flanges—the bottom is tapped to accept a vacuum pump flange; the top is sealed with an over-sized flange. The horizontal four-way cross is made of symmetric 7" ID bores, each with an external O-ring groove. The chamber is also fitted with a series of BNC connector feedthroughs. On each corner going around the horizontal cross there are 8 such feedthroughs for a total of 32 connectors on the chamber. Each feedthrough is fitted with an O-ring and screwed into mating threads in the chamber wall. The experiment itself only uses eight of the connectors (plus an additional two during early diagnostic tests), leaving the additional 20+ connectors as potential leaks that had to be checked and fixed during the course of setup.

To evacuate this chamber, two different pumps were used. During initial setup, a Varian VHS-6 diffusion pump (with a pumping speed of 1550 l/s) was used to pump out the chamber. While effective, this pump had a few inherent issues which eventually led to its retirement. The VHS-6, like most diffusion pumps, required an extended cool-down period after operation had concluded. Because of this, a gate valve was added between the chamber and pump to allow it to be isolated while the chamber was vented. In order to accommodate the gate valve, an additional adapter flange was also necessary which increased the overall chamber volume and decreased the tube bore leading to the chamber and thus the pumping speed, thereby increasing evacuation time for the chamber. Despite these issues, the VHS-6 worked well enough that we continued to use it for several years until it was found that oil mist was drifting into the main chamber. We

briefly considered adding a liquid nitrogen vapor trap, but it was determined that the chamber geometry did not allow for easy addition of such a trap and furthermore adding such a vapor trap would further reduce the pumping speed below acceptable levels.

In order to solve the oil contamination issue, we switched from our diffusion pump to a refurbished Pfeiffer TPH-1500 turbo pump. At 1500 l/s, the TPH-1500 delivers nearly the same pumping speed as the VHS-6, but with the advantage of an oil-free turbine mechanism. The pump is driven by a TCP-300 pump controller which is optimized for long-term operation of the turbo pump. Using this controller, the pump requires a spin-up time of 30 minutes and reaches full operating vacuum after about 45 minutes—comparable to the warm-up time required by the VHS-6. Unlike the VHS-6, however, the TPH-1500 only requires 10–15 minutes of spin-down time before the chamber can be vented—less than half of the cool-down time required by the diffusion pump. Thus, the total turnaround time for the turbo pump ends up being roughly half the time required by the diffusion pump, thereby alleviating the need for a gate valve. The removal of the gate valve significantly reduces the leak rate of the chamber while also allowing us to switch to a shorter, larger-bore adapter flange between the chamber and pump. Hence, in addition to solving the oil contamination issue, the switch to the turbo pump also increases our overall pumping speed and reduces our overall pressure. With these modifications in place, we were able to achieve almost an order of magnitude lower pressure than with the previous pump configuration. Under typical operating conditions, the turbo pump is able to achieve a vacuum of $1\text{x}10^{-6}$ Torr, with an ultimate recorded pressure of $7\text{x}10^{-7}$ Torr (with the molecular beam absent). Under these conditions the mean free path in the vacuum chamber is on the order

of 5x10^3 cm [42]. With the molecular beam present, the pressure increases to ≈1x10^{-4} Torr, which corresponds to a mean free path roughly equal to the length of the beam line—still sufficient to allow for a collision-free molecular beam [42]. The source chamber pressure was monitored via a Granville-Phillips ion gauge fitted to a coupling flange on the horizontal cross.

3.1.2 Interaction Chamber

Connected to the front of the source chamber is the experimental beam line. The two regions are separated by a 1 mm skimmer which is screwed to the inner face of the source chamber flange. The addition of the skimmer collimates the molecular beam while also allowing us to differentially pump the source and beam regions of the experiment. In order to prevent damage to the fragile skimmer during pump-down from atmosphere, the skimmer is set off from the chamber wall by approximately 2 mm, leaving a gap for viscous flow gas at higher pressures to move around it while still shadowing the beam line opening from direct molecular flow at lower pressures.

The first major component of the beam line following the source chamber is the interaction chamber. This is a commercially produced, 2.75" spherical cube from Kimball Physics. This particular model was chosen due to its large internal volume and the number of available ports it provided. This model also includes provisions for a variety of internal mounting options which proved to be invaluable during the early stages of the experiment. The spherical cube is attached to the source chamber via a semi-custom 3 1/8" long 2.75" CF nipple purchased from Kurt J. Lesker. The interaction chamber was originally attached directly to the source chamber output flange, but this connection required the use of O-ring

sealed screws which made it difficult to maintain proper vacuum and the tight clearance severely limited access to the interaction chamber. On the horizontal axis, perpendicular to the beam line, two 1" anti-reflection coated windows are mounted to provide optical access to the molecular beam for the BCF light.

The vacuum pump for the beam-side of the experiment is also attached to the interaction chamber. A wide-bore 2.75" CF nipple connects the bottom of the interaction chamber to the top of a Pfeiffer TPH-180H turbo pump (pumping speed 180 l/s). During initial testing, before the rest of the beam line was added, a smaller TPH-050 pump (pumping speed of 50 l/s) was used, but the additional gas load of the beam line and detection chamber necessitated the move to a larger-capacity pump. With the TPH-180H installed, the beam line is able to achieve a vacuum of $1x10^{-6}$ Torr without the molecular beam or $1x10^{-5}$ Torr with it, corresponding to mean free paths of roughly 50 m and 5 m, respectively [42]. This pressure was measured with a secondary Granville-Phillips ion gauge fitted to the detection chamber (see sec. 3.1.3).

3.1.3 Detection Chamber

The final component of the beam line is the detection chamber. This chamber is attached to the interaction chamber via another semi-custom CF nipple from Kurt J. Lesker. This nipple comprises the main flight tube of the beam line and is longer than standard at 5 5/16". This length was chosen to give us a total distance of 223 mm from interaction to detection.

The detection chamber itself is another Kimball Physics vacuum chamber. Though we considered using another spherical cube, we ended up deferring to a so-called spherical square chamber instead. The primary motivators behind this

choice were to allow for greater access to the interior of the chamber and to leave sufficient room for detection optics/apparatus. The spherical square chamber is essentially an asymmetric six-way hub with two opposing 4.5" CF ports and four 2.75" CF ports arranged equally around a perpendicular axis. The chamber is arranged such that the 4.5" ports form the main horizontal axis, perpendicular to the molecular beam line. This configuration allows us to use the 4.5" flanges as our primary mounting platforms rather than trying to squeeze all of our chamber accesses onto the much smaller 2.75" flanges.

As is often the case with experimental chambers, we had to custom manufacture access ports in our 4.5" CF flanges. For one of the 4.5" ports, we started with a custom reducer nipple flange. The flange as delivered to us had a 6" length of tubing fitted with a KF25 port welded into the center of the 4.5" CF flange. We cut off the KF25 port and machined the remaining tube length to an angle of 56^o—Brewster's angle for our detection laser frequency. Finally, a 2" BK7 window from Thorlabs was Torr-Sealed into place at the far end of the tube, giving us a zero-reflection output port for our vertically-polarized detection laser (see Sec. 3.3.2). The other 4.5" flange required a bit more modification. With the help of our in-house machinist, we bored a 0.75" hole to serve as a viewport. Around the viewport we also added an O-ring groove as well as a bolt circle to accept an aluminum clamp (also manufactured in-house) which serves to hold an AR-coated window in place. In addition to the viewport, we also added a 1.33" CF flange to the 4.5" CF flange face. This was beyond what we had the in-house capabilities to do, so we instead sent our flange off to be modified. The additional port was added by Key High Vacuum. They drilled the flange and welded on the additional tube on according to our supplied blueprint and returned it after leak testing the

weld.

3.2 Supersonic Beam

The molecule under study in our experiment is calcium mono-fluoride (CaF). As a free radical, CaF is unstable in atmosphere and must be generated and used in real time. For our experiment, the most convenient and useful way to produce CaF is in the form of a supersonic beam. By generating our sample under high vacuum, we are able to minimize interference with background gases and observe the evolution of the beam without interference from non-experimental sources.

3.2.1 CaF Internal Structure

Despite the apparent inconvenience of working with an unstable species like CaF, it has an internal structure which makes it easy to address with available lasers. Like many other metal-halide free radicals, CaF has highly diagonal Frank-Condon factors throughout its electronic levels. In particular, the $A - X$ and $B - X$ (0,0) vibrational bands have Frank-Condon factors of 0.987 and 0.999, respectively [43–45]. When working with any molecular transition, minimizing losses to dark states is paramount in order to maintain signal. For most species, this means the addition of repump lasers to move lost population back into levels of interest. For CaF, however, near-unity Frank-Condon factors mean that loss to adjacent vibrational states is essentially a non-issue, thereby removing the need for a vibrational repump laser.

In addition to being (nearly) vibrationally closed, CaF also has a very well-known spectrum. Previous studies have examined many of the rotational levels throughout the $A - X$ (0,0), (0,1), and (1,1) bands [44, 46] as well as the $B - X$

(0,0) and (1,1) bands [44, 47]. One reason for this extensive study is the fact that transitions on these bands happen to be accessible by easily-generated laser frequencies. The $A-X$ electronic transition has a fundamental wavelength on the order of 580 nm which puts it well into the heart of dye-laser accessible frequencies. Similarly, the $B-X$ electronic transition has a fundamental wavelength on the order of 532 nm which is accessible by a dye laser or a frequency-doubled diode laser.

3.2.2 Molecular Production

As previously mentioned, CaF is a free radical and therefore highly reactive—reactive enough that it cannot be bottled or produced in atmosphere. Thus, in order to study it, CaF must be generated in vacuum. There are several ways to generate CaF, and each method has its pros and cons. For our purposes, it is most convenient to produce CaF by reaction in an expanding supersonic gas [43, 48–52].

The first step in the reaction is generating a source of Ca atoms. We accomplished this by ablating a rod of solid, pure calcium with a pulsed Nd:YAG laser. Our laser operates at a repetition rate of 10 Hz, which sets the repetition rate for the rest of the experiment. To that end, we used a TTL timing pulse from the laser as the master timing/synchronization clock. This timing pulse was taken from the "Fire" output on the rear of the Nd:YAG controller and was triggered internally after the flashlamp capacitor bank completed charging. This timing pulse has an adjustable delay which was set and fixed at 1 ms for the duration of the experiment. For ease of use and enhanced safety, we choose to use the visible 532 nm second harmonic output of the YAG rather than the near-infrared

fundamental output at 1064 nm. The output beam is focused from its original size, on the order of 4 mm, to a spot size of 1 mm by a lens with a 1 m focal length [49]. The waist location for the beam is set to be on the far side of the calcium rod, such that the ablation intensity will increase as the rod gets smaller and (as a result) further from the axis of the molecular beam.

In order to minimize drilling into the rod, an in-vacuo motor was added to rotate a threaded rod onto which the calcium rod is mounted. This allows us to simultaneously rotate and translate the calcium rod to move the ablation spot for more even wear. The threaded rod also serves to make end-of-travel switching easier. Momentary switches are connected such that the calcium rod mount strikes them at the end of travel and reverses the direction of the DC turning motor. A simple circuit was constructed such that the momentary switches trigger a flip-flop which in turn switches a small relay and reverses the motor current direction.

The raw output of the laser is far more powerful than what is needed for ablation. Average pulse energy for the raw output beam is roughly 60 mJ/pulse at 532 nm, whereas the energy needed for ablation is only ≈11 mJ/pulse [49, 50, 52]. Rather than intentionally misalign the laser, we instead added an adjustable beam splitter to the beam path. The nominal transmission of the beamsplitter is 30% at 45^o, but by adjusting the angle of the beamsplitter we are able to fine tune the transmittance to what we needed on a daily basis.

To generate CaF, the freed calcium atoms need to be reacted with a source of fluorine. Our source supplies the fluorine via a pulse of sulfur hexafluoride (SF_6) gas, mixed into an argon carrier gas. The gas mix is delivered to the chamber via a piezoelectric-driven pulsed valve. Our earliest attempts to generate CaF relied on a home-made valve. Using a commercial housing, we custom-built a

poppet sealing mechanism which attached to a piezoelectric bimorph actuator. The poppet was comprised of a stainless steel threaded rod which was clamped in place through the center of an annular bimorph disc. The sealing surface itself was a small viton O-ring which sat in a depression machined at the end of the poppet rod. Despite our best efforts, the valve never performed well enough to be our primary pulse source. We found that the PZT bimorph disc was prone to cracking and the electrical connections on its perimeter were too delicate to withstand the frequent handling that was required during the valve's development stages. We instead choose to use an older commercial valve based on similar technology. The Lasertechnix LPV pulsed valve that we use is also based on a PZT bimorph actuator, and is actually the platform on which we based our home-made design. The difference is that the commercial valve featured a much lighter-weight aluminum poppet with a viton face-seal glued to the end. The poppet rod itself is also glued, rather than screw-clamped, onto a solid bimorph disc, thereby further reducing the weight of the mechanism. The commercial bimorph also seems to have much more robust electrical connections—soldered directly to the face of the PZT surface, rather than the custom disc's fine solder pads along its edge.

The pulsed valve is driven by an old home-made driver. The driver is externally triggered by the TTL pulse from the YAG and features an adjustable 0-80 V output pulse, an adjustable pulse width, fine and coarse adjustable pulse delays, and an external sync TTL output. Initial characterization of the valve operation/timing was done by observation of a high-voltage discharge glow from neon pulsed through the valve. From the glow discharge data, it was determined that when operated at 80 V, the valve required a pulse width of at least 200 μs to

open completely and that pulse widths in excess of 300 μs caused the poppet valve to bounce, resulting in a bimodal pulse. It was also observed that in addition to the adjustable delays, there was a fixed 200 μs delay between the external trigger pulse and the opening of the valve (presumably due to the high capacitance of the bimorph disc). After the minimum pulse width was determined, the pulse delay was adjusted empirically by optimizing the CaF flux signal. Fine tuning of the width and delay is performed iteratively until the maximum flux is achieved. The final values for pulse width and delay are 250 μs and 480 μs, respectively. Interestingly, while the CaF flux exhibits a peak in pulse delay, the flux plateaus with pulse width. This is likely due to the inherently short duration of the calcium plasma plume after ablation—it reacts optimally at a certain point in its evolution and additional SF_6 present after that point simply serves to increase the background pressure in the chamber.

In addition to the timing of the gas pulses, their composition also has a large effect on the CaF flux. The purpose of using a supersonic expansion as a molecular source is that supersonic beams of ideal gases have low rotational temperature and are nearly collision-free—their degrees of freedom are frozen out by collisions during passage through the valve orifice. However, SF_6 is highly non-ideal as a gas (it is typically stored in cylinders as a liquid) and must be buffered by an ideal carrier gas to expand properly. Furthermore, as has been said several times, CaF is highly unstable and an overabundance of SF_6 could potential cause further reactions with CaF, turning it into the stable form, CaF_2, which is (for our purposes) a waste product. We examined a number of SF_6 concentrations ranging from 1-4% in an argon carrier gas [49, 50, 52] and determined that 2% SF_6 produced the highest flux of CaF. Variation with backing pressure is harder

to study, but CaF flux decreases dramatically for pressures less than 20 psig and since there is no obvious signal increase for pressures above 30 psig, we choose to operate at that pressure.

3.2.3 Beam Parameters

Once the CaF beam had been established, we then measured the properties of the beam. The velocity of the beam is determined by observing the real-time time-of-flight (TOF) signal of the beam. The delay between the pulse valve sync pulse and the arrival of the CaF flux peak is measured to be ∼1.1 ms. For a beam line length of 474 mm, this corresponds to a mean velocity of 415 m/s with a FWHM of 75 m/s. Our measured velocity is slightly slower than the theoretical value of 432 m/s for a pure argon beam at 300 K. The difference is likely due to the added complications to the beam dynamics caused by interaction with the calcium plasma plume and the fact that our beam is not pure argon.

We also measure the rotational temperature of the beam by measuring the relative populations of the $J = 1/2$ and $J = 5/2$ rotational levels of the $v = 0$ ground state. Spectroscopy on these states via $Q_{12}(1/2)$ and $P_{22}(5/2)$ transitions show an average population ratio of ≈2.0. Comparing this to a Maxwell-Boltzmann population distribution model suggests an average rotational temperature of 2.2±0.7 K. This value is consistent with temperatures reported by other groups using similar supersonic beams [49, 52].

Initial estimates of beam brightness were computed by assuming a beam diameter of 3.68 mm at the interaction region based on the pulsed valve/skimmer geometry, and using the peak fluorescent photon flux of our TOF signals, as collected by a 15 μs boxcar gate, to find the peak beam flux. After taking

into account detector collection efficiency, gain, and quantum efficiency, we estimate the number of incident molecules and compute a brightness of $7.24\text{x}10^{11}$ molecules/sr·s. Further measurements, however, revealed an error in our beam size estimate. After changing the detection geometry to increase our photon collection area by a factor of 2.81, the corresponding increase in signal size was not proportional. Thus, we determine a more accurate upper-limit on the size of the CaF beam to be 5 mm, resulting in a calculated brightness of $1.54\text{x}10^{12}$ molecules/sr·s. This was further refined after direct measurement of our beam size (see Fig. 3.2) yielded a width of 1.64 mm, and thus a brightness of $4.57\text{x}10^{12}$ molecules/sr·s (or approximately $1.98\text{x}10^{8}$ molecules/sr·pulse). Though specific values have been difficult to find, other sources of the same type have reported brightness on the order of $3\text{x}10^{13}$ molecules/sr·s (reported as $1.4\text{x}10^{9}$ molecules/sr·pulse)[53, 54]—roughly an order of magnitude higher than what we are able to observe. This lack of signal is the primary stumbling block for our experiment. Our low signal necessitates extended data collection periods in order to get a high enough signal-to-noise ratio to have meaningful results. This means that we have to strictly limit the number of condition sets we are able to explore and instead focus on a limited number of variables. Of the improvements/changes that could be made to the experiment, increasing signal brightness is potentially the most important factor in improving the overall performance of the experiment. A brief summary of the key parameters for the ablation source are included in Table 3.1.

3.3 Detection

We detect our beam by laser-induced fluorescence (LIF) on an $A - X$ transition in CaF. To cut down on scattered light, we excite on the weak, off-diagonal

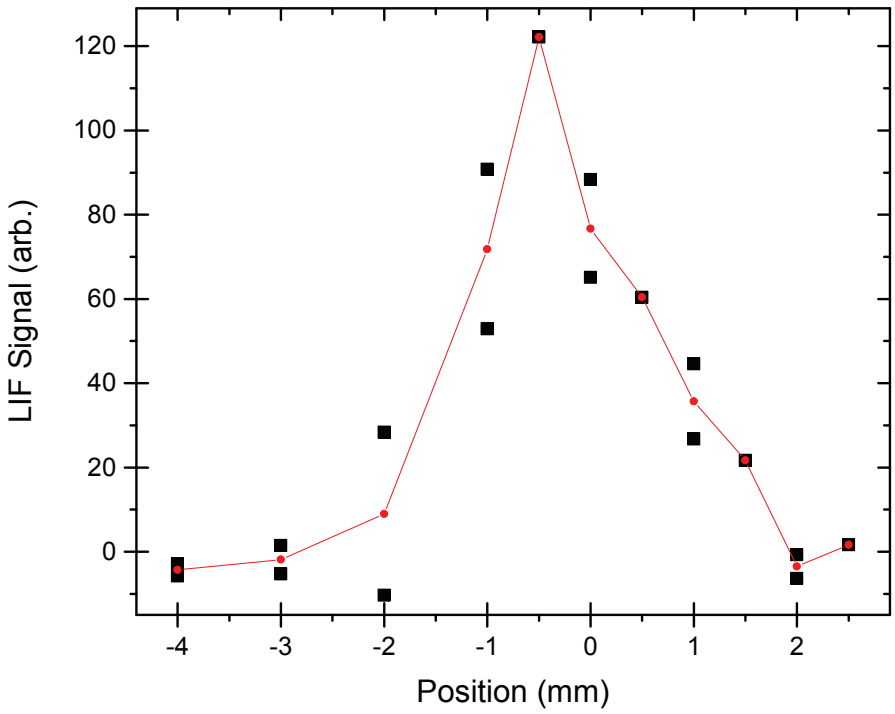

Fig. 3.2: Direct measurement of the vertical profile of our CaF beam at the interaction region. Using a resonant $B - X$ transition, the detection laser was translated along y and the LIF measured at each point. A fit to the data yield a width of 1.64 mm.

Table 3.1: A summary of parameters used for the ablation source.

Property	Value	Units
Ablation wavelength	532	nm
Pulse Energy	11	mJ
Average Laser Power	110	mW
Ablation spot size	1	mm
Carrier Gas	Ar	
SF_6 Mix	2%	
Gas Backing Pressure	30	psig
Mean Velocity	415	m/s
Rotational Temp	2.2±0.7	K
Brightness	$4.5x10^{12}$	molecules/sr·s
Ca Rod diameter	0.2	inches
Rod mount shim thickness	2*	mm
Pulse Width	200	μs
Pulse Delay	480	μs
Valve orifice	1	mm

*typical value, needs occasional adjustment

(1,0) vibrational band at 583 nm and detect on the much stronger (1,1) band decay at 606 nm. The excitation beam is generated by a Coherent 699 dye laser operating with Rhodamine-6G laser dye, pumped by a Coherent I-300 argon-ion laser, and locked to a molecular iodine transition. The detection frequency is approximately 23 nm redder than the excitation which allows us to reject residual dye laser scattered light with a filter stack placed before our detector. The detector itself is a Hamamatsu photomultiplier tube (PMT) module—a self-contained PMT, power supply, and gain controller. Fluorescence is collected by an in-vacuuo aspheric lens and refocused onto the detector by a matching lens outside the chamber. An additional silicon photomultiplier (SiPM) has also been added on a perpendicular axis. The SiPM is intended to work as a normalization detector, but never worked as well as we hoped it would.

3.3.1 LIF Transition

For a pulsed beam experiment such as ours, LIF is a natural choice for detection. We laser-excite molecules in the beam and collect the subsequent spontaneous decay fluorescence. The optically accessible transitions in CaF have sufficiently short excited-state lifetimes (τ=19.8 ns for $A-X$ [45]) that, on the scale of the supersonic beam flight time, the decay is essentially instantaneous. As such, the time-dependence of the signal fluorescence will accurately reflect the time-of-flight distribution of molecules. As stated previously, CaF has two easily accessible optical transitions from which we were able to choose: either the $A-X$ or $B-X$ electronic transition. For detection we choose to use the $A-X$ transition. While both transitions have remarkably high Franck-Condon factors on their (0,0) bands—0.987 for $A-X$ vs 0.999 for $B-X$—the $B-X$ transition's is more favorable. The closure of this decay route is more important for BCF cycling than it is for detection, thus we decided to save the $B-X$ for our force transition (keeping $A-X$ in mind as a backup). In addition, the laser system needed for $B-X$ was still under construction while we were beginning characterization of the CaF beam. Thus choosing $B-X$ would have meant that any measurements of the beam would have had to wait, whereas the $A-X$ laser system (see Sec. 3.3.2) was already complete, allowing us to begin beam diagnostics immediately.

After settling on the $A-X$ electronic transition, we then selected a rovibrational transition to excite within the electronic transition manifold. We knew we would be exciting out of a low-lying rotational state in the $v=0$ vibrational band for our BCF transition, so the detection transition would also have to excite out of the $v=0$ state. The diagonality of the (0,0) transition means that excitation on the (0,0) band would require collection of fluorescence on the (0,0)

band as well—i.e., at the same frequency. This type of detection scheme requires extremely stringent controls on the amount of scattered excitation light within the experimental apparatus or one risks losing small fluorescence signals in the shot noise of the scattered light. To get around this issue, we choose to instead excite on the next logical choice: the weaker, off-diagonal (1,0) band, as shown in Fig. 3.3. The (1,0) band in $A - X$ has a Franck-Condon factor of $\sim$0.013 while its diagonal counterpart, the (1,1) band, has a Franck-Condon factor of $\sim$0.98 [45, 55]. Thus, the vast majority of excitations to $v' = 1$ will decay to $v = 1$ instead of $v = 0$, allowing us to separate the two frequencies. In CaF, the (1,0) band pump is centered near 583 nm while the (1,1) decay signal is centered around 606 nm [55]. This $\approx$23 nm difference allows us to filter out scattered light from our excitation beam while collecting the redder fluorescence from our molecular beam signal. The tradeoff for this convenience is that excitation on the off-diagonal (1,0) band will only produce one photon per molecule as excited molecules are immediately lost to the dark $v = 1$ state. Furthermore, the (1,0) band is a very weak transition, requiring far more intensity to saturate it than the (0,0) band requires (see Sec. 3.3.2). Despite the weakness of this transition, the analogous transition is even harder to saturate in $B - X$, where the Franck-Condon factor is roughly an order of magnitude smaller ($\sim$0.0013 in $B - X$ vs. $\sim$0.013 in $A - X$). This would make a similar detection scheme far more difficult to implement in $B - X$, further justifying our choice of $A - X$.

With the vibrational transition selected, picking a rotational transition is simply a matter of determining which frequency would be easiest to lock. We began by examining the rotational structure of the $^2\Pi - {}^2\Sigma^+$ $A - X$ transition. Supersonic beam expansions typically have low rotational temperature, so we

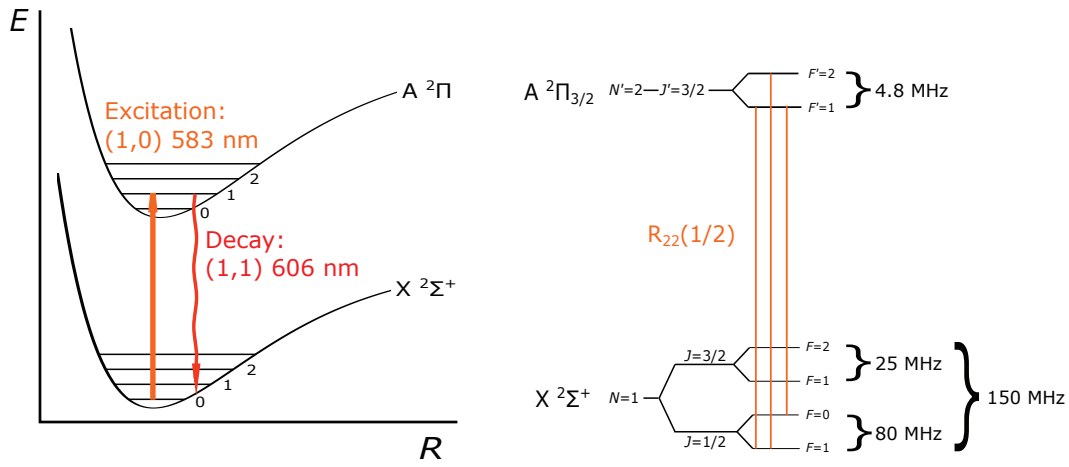

Fig. 3.3: The energy level structure of the $X^2\Sigma^+ - A^2\Pi$ electronic levels is shown. At left, representative potentials show the excitation and fluorescence bands used for CaF detection. At right, the rotational transition used for excitation, $R_{22}(1/2)$, is shown. This transition occurs at 17153.92 cm^{-1} (583 nm). Neither the upper-state hyperfine levels nor the ground-state hyperfine levels are individually resolved [56].

Table 3.2: Details on the $^2\Pi$ $A-$ $^2\Sigma^+$ X (1,1) band rotational transitions described in 3.3.1 based on Fig. 123 from [59]. Values listed for the transition wavenumber are computed from measurements listed in [44, 46, 47, 57]. The quantum number labels J (total angular momentum) and N (nuclear angular momentum) follow the convention of unprimed for ground-state labels and primed for excited-state labels.

Transition	J	J'	N	N'	$\overline{\nu}$ (cm^{-1})
$Q_{11}(1/2)$	1/2	1/2	0	1	17081.5685
$Q_{12}(1/2)$	1/2	1/2	1	1	17080.9342
$R_{11}(1/2)$	1/2	3/2	0	1	17082.6686
$R_{12}(1/2)$	1/2	3/2	1	1	17081.8884
$R_{21}(1/2)$	1/2	3/2	0	2	17154.6120
$R_{22}(1/2)$	1/2	3/2	1	2	17153.9162

compiled a list of the transitions from $J = 1/2$: $Q_{11}(1/2)$, $R_{21}(1/2)$, $R_{11}(1/2)$, $R_{22}(1/2)$, $R_{12}(1/2)$, and $Q_{12}(1/2)$ (see Table 3.2 for details). Previous studies by Nakagawa [57] and Field [44, 46, 47] (among others [45, 55, 58]) have explored the rovibrational structure of CaF in detail. Extrapolating based on measured spectra from these sources, we found transition frequencies for each of the $J = 1/2$ transitions in the (1,0) band. Of the six options, only R_{22} and R_{12} are theoretically near enough to stable reference frequencies to properly lock (see Sec. 3.3.3). We note that we only need to find a transition within typical AOM range of an I_2 reference line. Since the $v = 0$ state would be depleted after a single excitation cycle, rotational cycling does not need to be considered. Spectroscopy revealed $R_{22}(1/2)$ to be the most convenient transition to work with, lying approximately 60 MHz from the nearest lockable iodine hyperfine line. A measured spectrum of the $R_{22}(1/2)$ transition is shown in Figure 3.4 along with an I_2 hyperfine manifold reference (see Sec. 3.3.3 for details).

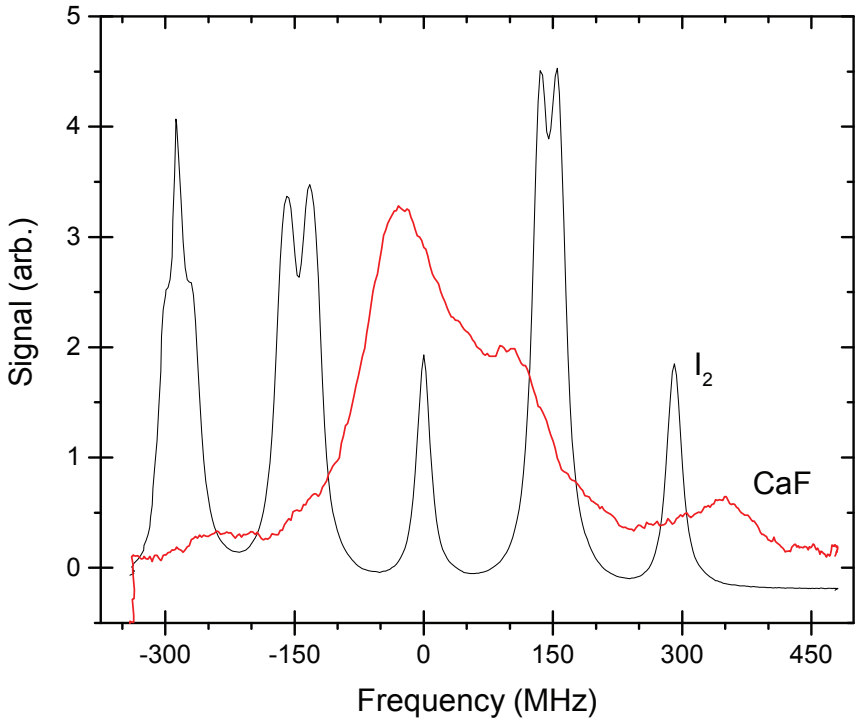

Fig. 3.4: A measured frequency scan of the CaF $A - X(1,0)R_{22}(1/2)$ transition with I_2 hyperfine levels for reference. The upper-state hyperfine structure is unresolved in the spectrum. The ground-state hyperfine structure is significantly broadened, but some features are evident within the scan.

3.3.2 Detection Laser System

As stated previously, the (0,0) and (1,1) bands in CaF's $A - X$ electronic transition are optically-accessible transitions in the neighborhood of 600 nm. This wavelength region is one that is difficult to access via diode lasers, but lies in the heart of dye-accessible wavelengths. Thus, despite their lack of popularity in recent years, a dye laser still makes an excellent choice for accessing these transitions. For our detection laser, we use a Coherent 699 dye laser system. The 699 is an older platform, but proved to be very reliable throughout the course of the experiment. As the gain medium, we run a Rhodamine-6G (R6G) dye, a.k.a. Rhodamine-590, which has a peak output at around 590 nm. The dye is mixed at a concentration of 0.0025 M in ethylene glycol—typically mixed as 1.1 g of R6G chloride or 1.25 g of R6G perchlorate into 1.1 l of pure solvent. There is no apparent difference in output power or spectral performance between the two different salts, but the chloride seems to dissolve more easily into the ethylene glycol while the perchlorate seems to exhibit longer operating lifetimes.

The dye is pumped via a Coherent I-300 or I-200 Argon ion laser operating with multi-line output at a nominal power of 7 W. The I-200 was used during earlier testing, but was abandoned after it malfunctioned. Actual measured pump output power is typically closer to 6.7 W, but as dye mixes near the end of their lifetimes, pump power can be increased to temporarily compensate for the reduced output efficiency. Typical output of the 699 with the I-300 pump is on the order of 600-700 mW broadband or 300-400 mW single-mode. Single-mode outputs for the I-200 pump tend to be closer to 500 mW. The output of the 699 is sent to a 90/10 beamsplitter, as shown in Figure 3.5. The 90% component is sent to the experimental chamber, the 10% component is used for beam diagnostics and

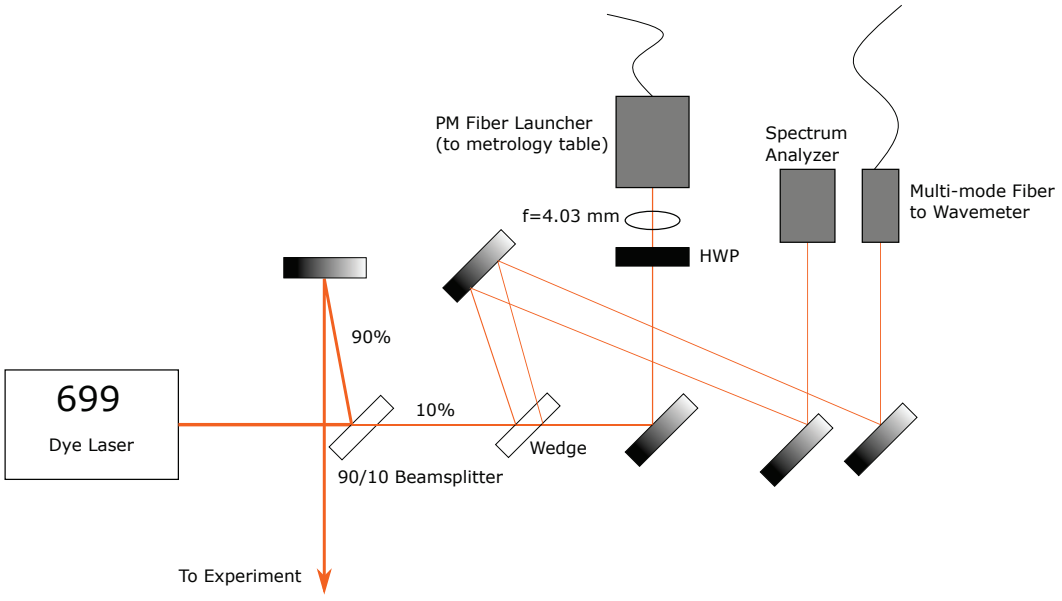

Fig. 3.5: A diagram of the dye laser optical system used in the experiment. The dye laser output is split: the primary beam is sent to the experimental chamber while the secondary beam is used for diagnostics and locking. Diagnostic signals from the spectrum analyzer and wavemeter are used to grossly tune the frequency of the dye laser before it is locked and to monitor the stability of the lock once it has been established (see Sec. 3.3.3).

locking (see Sec. 3.3.3).

The beam sent to the experimental chamber is first folded backwards to a 0^o mirror. The 0^o mirror helps to compensate for the effect of beam shifts due to internal realignments of the dye laser before the beam is sent to the experimental chamber. When the beam exits the laser head, it has a waist diameter of 0.75 mm which then expands to 3.53 mm by the time it reaches the experimental table. Before entering the vacuum chamber, the beam is reshaped by a pair of telescopes. The first telescope is a 1:1 spherical telescope comprised of a pair of

f=10 cm plano-convex lenses which re-collimate the diverging beam and set the vertical $1/e^2$ diameter to 2.45 mm. The second telescope is a horizontal cylindrical telescope which uses an f=25 cm plano-convex lens and an f=-8 cm plano-concave lens to compress the horizontal dimension to a $1/e^2$ diameter of 0.4 mm. The final radii as the beam entered the chamber was approximately 1.22 x 0.4 mm which yields an average intensity of $\approx$20 W/cm^2 for $\sim$300 mW of output power. This corresponds to a little more than twice the intensity at which the detection signal was measured to saturate for the $A - X$ (1,0) $R_{22}(1/2)$ detection transition (see Fig. 3.6). At this intensity, we expect to excite each molecule within the detection beam once and still retain enough of an intensity overhead to sustain saturation if the dye laser power sags.

3.3.3 Frequency Stabilization

As stated previously, the 10% beam sample pulled from the laser output (see Sec. 3.3.2) is used to monitor the dye laser's output power and mode quality, and to lock the laser frequency (see Fig. 3.5). The majority of these tasks are handled on an isolated optical table specifically set aside for metrology. This optical table is coupled to the main table by a polarization-maintaining (PM) single-mode optical fiber. The fiber typically delivers 15-20 mW to the metrology table; a coupling efficiency of $\sim$37.5%. Upstream of the fiber coupling, a wedged flat picks off two more diagnostic beams for use on the main optical table. The first-order reflection is coupled into a multi-mode optical fiber which is then coupled into a Burleigh WA-1000 wavemeter. The second-order reflection is sent into a Thorlabs SA210 scanning optical cavity. The wavemeter is used to verify that the dye laser is tuned to operate on the correct cavity mode. Rather than having to

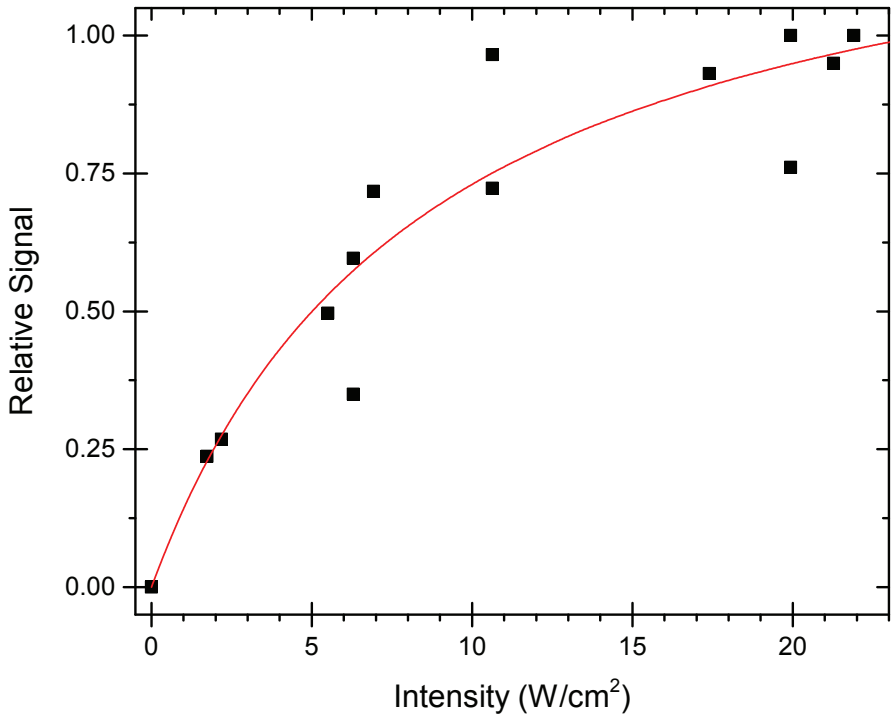

Fig. 3.6: The measured $R_{22}(1/2)$ signal magnitude as a function of input laser intensity. While locked to the CaF transition frequency, the power of the dye laser was attenuated and the signal response measured. Fitting the average CaF to a saturation curve gives a saturation intensity of 8.5 W/cm^2.

monitor the reference spectrum during tuning, we only need to verify that we are tuned to a frequency within the mode-hop-free scan range of the laser—roughly 15 GHz—from our locking transition. The cavity interferometer was is to monitor the longitudinal mode quality of the beam and, to a lesser extent, qualitatively monitor the smoothness of frequency scans.

Once on the metrology table, the light is sampled by another wedged optical flat. The first-order reflection is sent through a temperature-stabilized marker interferometer cavity and the second-order reflection is sent to an amplified photodiode for overall power monitoring. The power monitor simply serves as a normalization metric for fluctuations in the diagnostic signals. The marker cavity has a free-spectral range of 299.79 MHz and is used to calibrate frequency scans, particularly those done during early exploratory spectroscopy tests. Following the wedge, the remaining diagnostic light is used for saturated absorption spectroscopy in an iodine reference cell.

The saturated absorption spectroscopy (SAS) locking setup is based on a generic 3-beam configuration [60]. A thick, uncoated optical flat picks off two $\approx$10% samples from the main beam to serve as probe beams while the remainder is used for the pump beam. The weaker of the two pickoff beams (generated by reflection from the rear surface of the flat) is used as the probe beam of the SAS pump-probe pair, while the stronger pickoff serves as a normalization beam. The two beams are sent through a room-temperature quartz reference cell filled with iodine, which serves as the frequency reference for our laser lock. The entrance and exit windows of the cell are fused silica and are tipped by few degrees to reduce etaloning in the probe beams. The absorption in the probe beams was detected on a pair of photodiodes connected to an auto-balancing circuit (see appendix

A). The homemade circuit is based on an older design [61] and automatically adjusts the internal gain to maintain balanced subtraction of the inputs. This subtraction removes residual Doppler broadened spectral features from the signal, leaving only the Doppler-free elements behind. Despite the increased resolution granted by the signal subtraction, the hyperfine elements of I_2 are still too weak to resolve directly, so we implemented a lock-in detection scheme to further amplify the signal.

Lock-in detection requires the signal to be modulated, so a modulation was added to the pump arm of the optical setup. For preliminary frequency scanning experiments, the pump beam was chopped via an inexpensive 60 MHz commercial AOM, driven by a commercial IntraAction AOM driver as depicted in Figure 3.7. This AOM was not particularly efficient—topping out at around 40% diffraction efficiency. To increase modulation depth, the 1st-order beam was used as the pump. The chopped signal was fed into a home-made lock-in demodulator (see appendix A for details) which also provided a 10 kHz chopping frequency reference for the AOM driver. This configuration was used to perform the exploratory spectroscopy we needed to locate a locking feature near our CaF transitions. We found that the I_2 $B-X$ (18,2) $R(108)$ transition at 17153.9162 cm^{-1} overlapped neatly with the $A-X$ (1,0) $R_{22}(1/2)$ transition in CaF. A shift of ≈60 MHz was all that was necessary to bring an appropriate singlet line in the I_2 spectrum onto the peak of the CaF resonance. Before we could actually lock, however, we needed to apply the shift and adjust the reference lineshape.

The binary on/off chopping of the pump AOM yields an I_2 hyperfine spectrum with Lorentzian lineshapes. For locking, dispersion shaped signals are more robust. To generate these derivative signals, we instead dither the frequency of the

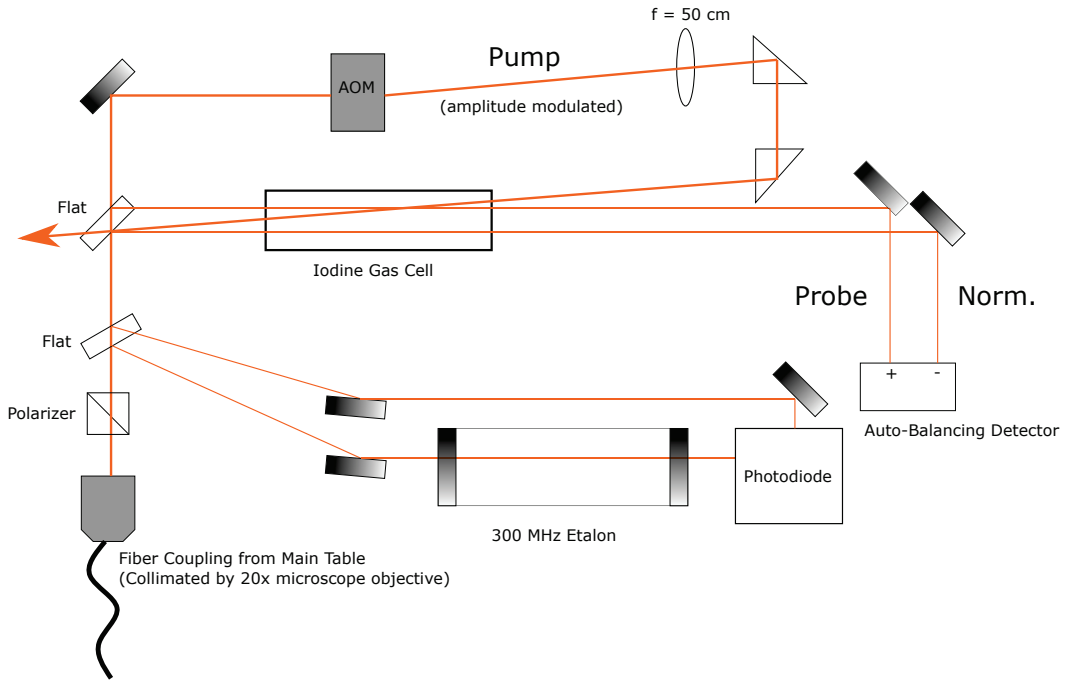

Fig. 3.7: A diagram of the first-generation locking optics setup. The lock is based around a typical 3-beam saturated absorption spectroscopy configuration. A strong pump beam is sampled by an optical flat to produce two weaker beams: a probe and a normalization. The pump is chopped by an AOM—the 1st order diffracted beam is used as the pump in order to maximize modulation depth—and intersected with the probe beam. The normalization and probe signals are collected and subtracted to remove the Doppler-broadened background from the measured spectrum.

pump beam. Using a double-passed IntraAction ADM-602AF1 AOM (as shown in Fig. 3.8), we switch the driving frequency of the AOM between 58 MHz and 46 MHz—i.e. a 52 MHz central frequency with a dither of ±6 MHz—at the 10 kHz chopping frequency. Unfortunately, the commercial driver is not capable of performing this dither, so we instead use a home-made frequency synthesizer and RF amplifier (see appendix A). The spectrum which results from this dither is shown in Figure 3.9. Note that despite a small shift of the frequency axis, Figs. 3.9 and 3.4 both show the same I_2 hyperfine manifold. The lock itself is maintained using a PID controller integrated into our home-made lock-in amplifier. The PID loop gains are set empirically and the error signal is sent into the remote scan input of the 699. Locked in this way, the laser will remain stable for hours at a time. Warm-up drift in the 699 cavity itself typically limits the locking time to 3 or 4 hours immediately after startup, but during extended operation, the lock was sometimes held for more than 12 hours at a time. Stability of the lock was never rigorously measured, but an estimate was computed from the RMS jitter of the lock-in signal. By comparing the measured RMS error signal voltage during lock to a frequency-calibrated scan of the locking transition, the jitter is estimated to be on the order of 1 MHz. A summary of the beam conditions used for SAS locking are included in Table 3.3.

3.3.4 LIF Detection

To detect our LIF signal, we considered several different detector options including avalanche photodiodes, silicon photomultipliers, and traditional photomultipliers. After careful consideration of estimated signals and noise we determined the best option to be a Hamamatsu H10721-20 photomultiplier tube

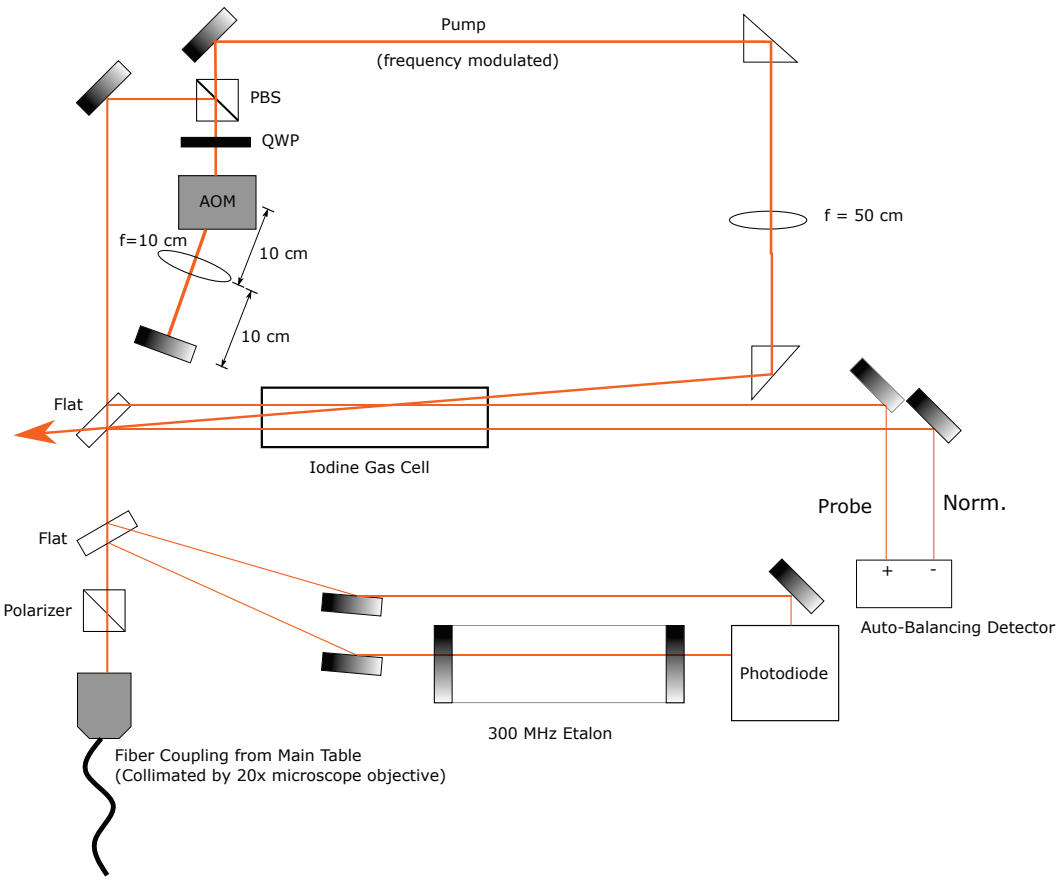

Fig. 3.8: The second-generation frequency lock setup uses a double-passed AOM to dither the the frequency of the pump beam rather than modulate its amplitude. The AOM frequency is modulated about a central 52 MHz shift by ±6 MHz at a rate of 10 kHz. Using the dither rate of 10 kHz for lock-in amplification produces a dispersion-shaped spectrum which is well-suited as an error signal for locking (see Fig. 3.9).

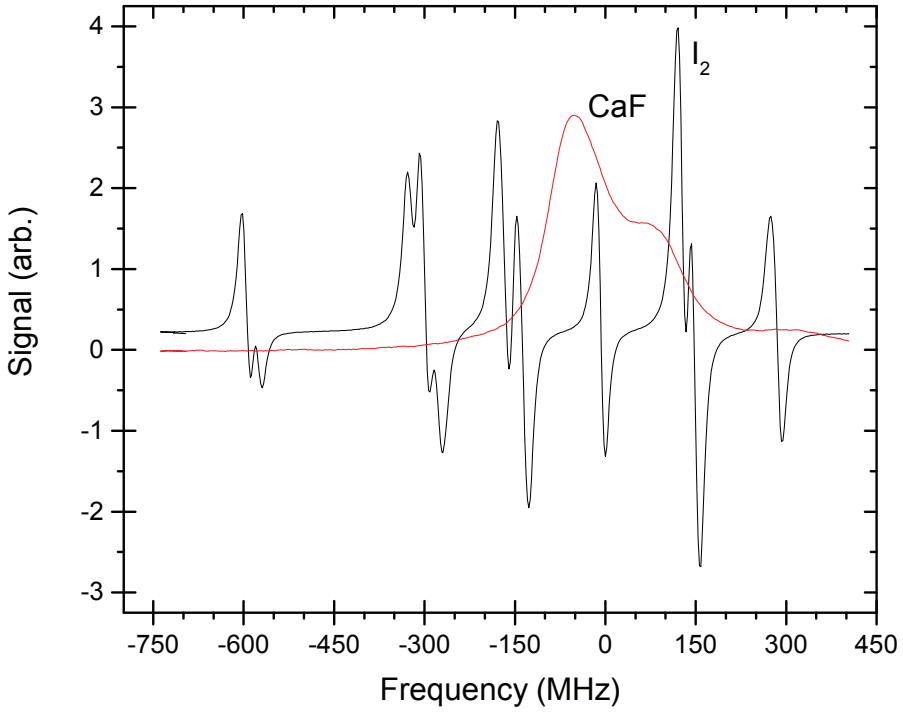

Fig. 3.9: The hyperfine spectrum of the I_2 $B - X$ (18,2) $R(108)$ transition as measured via the second-generation dither locking scheme (see Fig. 3.8). This is the same spectrum as shown for the first generation scheme in Fig. 3.4. The CaF $A - X$ (1,0) $R_{22}(1/2)$ was measured concurrently and is used to determine the frequency shift needed to properly set the lock point for the dye laser.

Table 3.3: A summary of beam parameters used for SAS on I_2. The SNR was measured to be on the order of 400 for cases (a) and (b). The values in (c) are reference values taken from [60].

(a) AOM Chopping	(Single-pass, 40% efficiency at 60 MHz)		
Beam	Power (mW)	Waist radius (mm)	Intensity (mW/mm^2)
Normalization	1.3	0.27	5.75
Probe	1.1	0.30	3.94
Pump	6.4	0.42	11.7

(b) AOM Dither	(Double-pass, 80% efficiency/pass at 52 MHz)		
Beam	Power (mW)	Waist radius (mm)	Intensity (mW/mm^2)
Normalization	0.61	0.52	0.714
Probe	0.521	0.50	0.665
Pump	4.56	0.31	14.8

(c) Reference [60]			
Beam	Power (mW)	Size (mm)	Intensity (W/cm^2)
Normalization	0.1	<1	$\sim$0.003
Probe	0.1	<1	$\sim$0.003
Pump	10	1	0.318

module. These modules are small, self-contained units housing a PMT within a TO-8 can, a HV power supply, and an adjustable gain controller. The H10721-20 model has peak responsivity at 630 nm and has a response of 78 mA/W—i.e. quantum efficiency of 0.16—at our detection wavelength of 606 nm [62]. The module is operated from a home-made controller (based on our general-purpose lab interface card design, see appendix A, which supplies the +5 V input power as well as the 0.5-1.1 V adjustable gain control voltage. The control voltage varies the gain continuously from $5x10^4$-$4x10^6$, scaling (approximately) as $(2x10^6)V^8$, where V is in volts. For flexibility, we opted for a current-output type module, which necessitates the addition of a trans-impedance amplifier (TIA) before data acquisition. Another home-made circuit, our TIA is a modified version of our general-purpose photodiode box (see appendix A), based around an AD8606 opamp. The amplifier is configured with a trans-impedance gain of 100 kΩ, and a secondary output amplifier stage with a gain of 2. The output of this combination yields maximum signal amplitudes on the order of 4 mV. Signals on this level are sufficient for real-time monitoring via an oscilloscope, but for the purposes of data acquisition, an additional post-amplifier stage with a gain of 100 was added before the data acquisition card.

To collect the LIF light and image it onto the PMT we use a pair of aspheric lenses mounted with their optical axis coincident with the CaF beam axis. The first lens has a focal length f=20.1 mm and is affixed inside the vacuum chamber on a home-made mount. The lens is placed such that its focal plane coincides with the LIF detection beam. The mount was machined in-house and is made of aluminum; it was painted black to reduce scattered light and was baked to reduce outgassing. The lens mount is attached to the chamber via Kimball Physicss

proprietary internal mounting groove-grabber system. The collimated signal light is re-focused by a matching asphere outside of the vacuum chamber, producing a 1:1 image of the molecular beam on the surface of the PMT photocathode (which is mounted with its active 8 mm diameter area facing the $-z$-direction, see Fig. 3.1).

Between the two lenses (outside the vacuum chamber) is a stack of optical filters used to reject the scattered 583 nm excitation light and pass the 606 nm signal light. The stack is comprised of four filters. The first is an FGL610 red colored-Schott glass longpass filter from Thorlabs with a cutoff at 610 nm. This filter nominally reduces the excitation light, but is installed principally to attenuate off-axis stray reflected light. To filter the on-axis light, two interference filters are used. The first is a Thorlabs FEL0600 longpass filter with a cutoff at 600 nm, the second is a Semrock LP593 longpass filter with a cutoff a 593 nm. These two filters combine to pass roughly 85% of light at the 606 nm detection wavelength while attenuating the excitation light by a factor of $\geq 10^9$. The final filter is an IR blocking colored Schott glass filter, also from Thorlabs. It was added after we found that the ablation YAG was saturating the PMT, despite being at a wavelength that should be totally rejected. The apparent cause of the saturation was IR fluorescence of the FGL610 glass filter under exposure to intense 532 nm light [63–68].

Despite the effectiveness of the filter stack, scattered light is still the dominant noise source during the experiment. The high power required to saturate the detection transition means that even small diffuse reflections add a lot of light scattered from the chamber relative to the signal size. The Kimball Physics detection chamber is intended for high-vacuum use, so every internal surface is

highly polished, which only exacerbates the problem. To help alleviate this issue, several internal and external light baffles are added to the experiment. Externally, a rectangular mask is added to the input window to limit the entrance aperture to roughly twice the area of the detection beam. The input window is then shrouded with an extended cardboard tube and wrapped in shielding cloth to physically block stray light scattered from optical surfaces from entering the chamber at oblique angles. The output Brewster window is also masked with a slit which passes the entire detection beam, but shields the rest of the window surface from room light. The PMT is also shielded externally. After being pressed tightly against the lens tube housing the filter stack and focusing lens, the entire assembly is covered with a box and further wrapped in shielding cloth. Inside the vacuum chamber, several baffles made of black-painted metal are added to further reduce internal scattered light. The flange bores inside the input and output windows are both lined with cylindrical baffles that extended into the chamber. The LIF collection lens is also surrounded with a baffle that extends from the rear of the lens mount to the chamber output window. As an additional step to help reduce obliquely scattered light from the BCF beams, the flight tube has also been lined with a black cylindrical baffle. As a final measure, during experimental operation, the room lights are turned off and the nearby computer monitor brightness is decreased. Out of all of these measures, none of them proved to be a decisive factor, but rather they work together to reduce the scattered light bit by bit to a level comparable to the signal size, i.e. to an RMS voltage on the order of a few mV.

In order to measure deflection in the beam, we need to add a spatial filter. The PMT photocathode is a uniformly responsive surface, thus we add a physical filter to shield all but a particular vertical slice of the molecular beam. The filter

itself is simply a spectrometer input slit from Newport. We chose a slit with a 0.76 mm width to match our expected shift under optimal BCF conditions. The slit is mounted to an in-vacuum linear actuator from Huntington Mechanical Labs (L-2111-1) which is attached to the detection beam input side of the chamber via a 1 1/3" CF flange. The actuator has a nominal stroke of 1" which allows us to translate the slit from edge to edge of the PMT's 8 mm active area while still allowing us to fully retract the slit to expose the entire PMT to the beam at once. To retain image fidelity, the slit is positioned approximately 1 mm from the center of the detection laser beam—any closer and the detection beam starts to clip on the slit mount and the scattered light signal increases dramatically. To further refine our view, we also add a horizontal masking slit to the face of the PMT. A 1.5 mm mask is added to the detector to limit our light collection to only the portion of the molecular beam that is affected by the BCF. The mask reduces our overall signal magnitude, but increased our relative contrast and thus sensitivity to small shifts in the molecular beam.

As a final measure, in addition to the PMT detector, we also experimented with a SensL silicon photomultiplier (SiPM) mounted perpendicular to the beam as a normalization detector. A C-series SiPM with a 3x3 mm active area and 50 μm microcells was soldered to a spare printed circuit board (PCB). The power and gain controls are provided by a small home-made circuit and the output is sent into another retro-fitted photodiode TIA circuit. External optics matching those for the PMT (an aspheric lens with f=20.1 mm and a comparable filter stack) are used for the SiPM, but due to space constraints inside the chamber a smaller f=18 mm lens is used for in-vacuum light collection. The internal lens is attached to the internal PMT lens mount, perpendicular to the beam axis (aligned along y). On

paper, the SiPM seems like a promising option for LIF detection, but it has never performed as well as projected. More development time, in particular for testing of the gain control circuitry and alignment of the imaging optics, is necessary before it will reach the desired performance levels. Once these operating conditions are achieved, the SiPM will be useful a tool for shot-to-shot normalization of the CaF beam signal.

Chapter 4

Deflection Experiment: BCF Laser System

Generating the laser frequencies necessary for BCF is a multi-stage process. A diagram of the full optical configuration can be seen in Figure 4.1. As is the case for the molecular source, the BCF laser system can be broken into three main sub-systems: a primary IR oscillator (with accompanying amplifier), a frequency doubler, and an acousto-optic modulator system used to generate the symmetrically detuned frequency components. Following the discussion of the laser systems, we will also discuss the details of data acquisition.

4.1 Oscillator and Amplifier

The B-X transition wavelength in CaF is at 531 nm—close enough to the 2nd harmonic of a Nd:YAG laser to use standard 532 nm optics, but not close enough that we could use a commercial 532 nm laser as our primary oscillator. Instead, we opt to frequency double a more easily tunable 1062 nm IR laser. The oscillator itself is a relatively low-power tunable diode laser. In order to get sufficient 531 nm output power, the oscillator is amplified before frequency conversion.

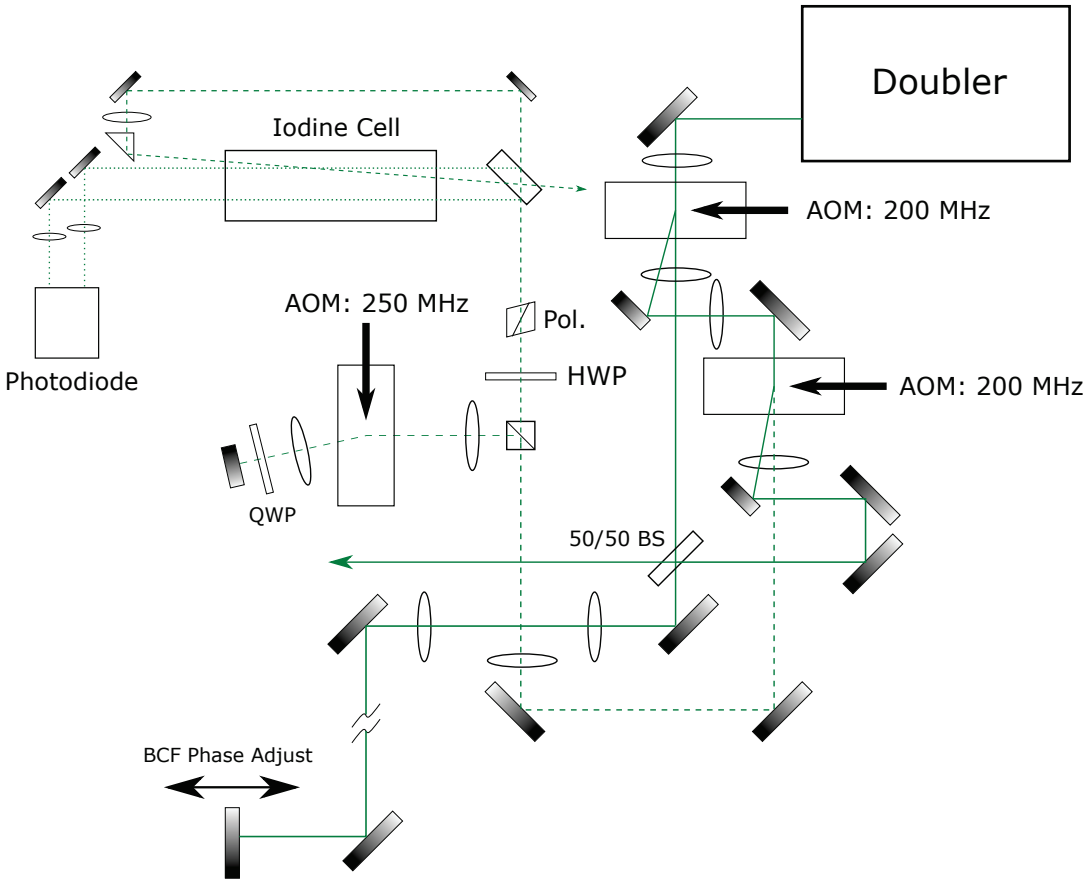

Fig. 4.1: A diagram of the laser system used to generate and lock the BCF beams. The doubler produces a total output of ∼1.3 W at 531 nm, which is then split into the $\omega_0 \pm \delta$ frequency components needed for the experiment. The frequency components are combined on a beamsplitter to form a train of beat note pulses. The counterpropagating pulse train is generated via a retroreflector, and the position of the retroreflector sets the relative phase between pulses. The secondary pulse train produced on the beamsplitter is used for alignment. Residual ω_0 light is used to lock the laser via SAS to an I_2 reference.

4.1.1 Oscillator Diode

For our oscillator, we use a 1064 nm distributed Bragg reflector (DBR) diode laser from Photodigm. As is the case for many of Photodigm's laser diodes, the DBR is intended for spectroscopy. This is reflected in the relatively narrow 8 MHz linewidth and high output power of 80 mW. The diode itself is mounted in a sealed TO-8 can along with an internal photodiode, thermistor, and thermoelectric cooler (TEC). The can is mounted to a heat sink mount (also from Photodigm) which included DB-9 and DC-15 connectors wired to the can's electrical and cooling pins, respectively.

The diode temperature is stabilized via its internal TEC. The proximity of the TEC to the diode means that the system responds very quickly and requires virtually no warm-up time for the diode. However, the lack of a secondary temperature regulation stage means that in order to maintain active control of the system, the diode must be cooled below ambient temperature, typically to $\approx 21^o$ C. Fortunately, cooling is already required in order to shift the center wavelength of the DBR from 1064 nm to 1062 nm. The temperature controller is a home-made microcontroller based PCB (see appendix A). There is a minimal set of indicator lights mounted on the PCB itself, but it is primarily operated via USB connection to an Android tablet. A home-made app on the tablet is used to set software output limits as well as implement the lock itself via an internal PID loop. The parameters of the locking loop were set empirically and yielded a settling time on the order of a few seconds. Hardware limits on the output—max current and max voltage—are also set to match the maxima of the DBR's TEC via the output driver opamp.

Supplying current to the diode are a home-made paired current driver and

controller PCB (see appendix A). Based on a design by the Durfee group at BYU [69, 70], the design first needed to be modified to account for our lower-threshold IR laser diode, and then was further modified to interface with a previously-designed current controller PCB. The output is software limited to the maximum current of the diode specified on the IV curve (70 mA) and is controllable via either PCB mounted controls or USB interface to a modified version of the parent Android app. Connected prior to the laser head itself are two additional circuits: a current modulation circuit board and a diode protection circuit. The modulation circuit is again based on the designs from Durfee [69, 70], but has been modified to include an adjustable modulation range (see appendix A). For a 0-5 V modulation input, the current modulation range is adjustable to 2 mA, 1 mA, 500 μA, or 250 μA—equivalent to frequency scans of 1.6 GHz, 800 MHz, 400 MHz, or 200 MHz, respectively. The protection circuit is another custom-made PCB (see appendix A) and is placed immediately adjacent to the laser head. Based on a design by Stone [71], the circuit is designed to suppress transients and accidental reverse-biasing of the laser diode. The protection circuit design also includes provisions for additional modulation (via a current shunt or bias-T), but they were not implemented for this experiment.

The output of the DBR is free-space coupled, so in order to couple into our amplifier, it first has to be fiber coupled. Due to the geometry of the DBR gain medium, the output beam is astigmatic and highly elliptical, featuring a highly divergent fast axis. The fast axis is collimated by an AR coated aspheric lens with focal length F=4.03 mm, held in a cage-mounted xy-flexure stage. The beam is then optically isolated before being coupled into to a Thorlabs fiber collimator (F=8 mm). Due to the ellipticity of the beam, it suffers several significant losses

along the beam path—particularly a roughly 42% loss through the isolator aperture. The remaining beam is coupled into a polarization-maintaining (PM) optical fiber with an efficiency of about 27% (observed efficiencies ranged from 25-30%). While this coupling efficiency is not particularly high, for the typical operating currents of ∼60 mA, it still provides more than enough coupled power to saturate the amplifier. The fiber-coupled sample of the beam is split a final time by a 90/10 splitter with the 90% sample coupling into the IPG amplifier and the 10% sample being output though an additional Thorlabs fiber collimator (F=10 mm) for miscellaneous diagnostics.

4.1.2 Fiber Amplifier

Generating enough 531 nm light for our experiment requires significantly more power than the DBR can output—we need an amplifier. We chose an IPG fiber amplifier (YAR-10K-1064-LP-SF) to fulfill our needs. The amplifier can output up to 10 W at 1064 nm, delivered via high-power optical fiber. The output is isolated (30 dB), linearly polarized, and collimated by an integral output coupler to a waist diameter of 0.9 mm. The active elements of the amplifier are entirely self-contained and require no user attention aside from ensuring adequate air flow for cooling. The unit is operated via a simple touch-screen interface embedded in the amplifier housing. The amplifier requires 1-5 mW of input seed power supplied via an isolated (30 dB) PM optical fiber input.

To prevent damage to the amplifier, the unit contains several internal interlock mechanisms. Disruptions to the seed input power or excessive back-reflections of the output cause the laser to shutdown automatically and require the user to manually clear the error before restarting. As a redundancy, we added our own

external interlock to the system using the internal photodiode signal from the DBR. If the DBR output power is lower than the minimum required to couple 1 mW into the input fiber, the amplifier was deactivated. The interlock consists of a simple MOSFET gate between two provided interlock pins with the output of the DBR photodiode signal acting as the gate control.

4.2 Frequency Doubling

Conversion from 1062 nm to 531 nm is performed using a second harmonic generation (SHG) crystal in a single-pass configuration. The crystal itself is a 1 cm long magnesium oxide doped, periodically-poled lithium niobite (PPLN) crystal purchased from Covesion (MSHG1064-0.5-10). The crystal is a single slab of lithium niobate measuring 10x10x0.5 mm. The periodic poling of the crystal alleviates the need for exact phase matching between the fundamental and second harmonic frequencies as they propagate. Introducing periodic inversions of the crystal orientation prevents the accumulation of phase between the two frequencies from interfering destructively. Embedded within the material are five active grating regions, each with a 0.5x0.5 mm cross-section and a different poling period. The range of poling periods allow for multiple wavelengths to satisfy the quasi-phase-matching condition required for efficient second harmonic generation. Fine tuning of the wavelengths is accomplished by tuning the temperature of the crystal. Heating for our crystal is supplied by a flat, large area ceramic resistor chip placed underneath the crystal's brass housing. A thermistor embedded nearby monitors the temperature, and the current driving the resistor is controlled with a home-made temperature controller (of the same design as is used to regulate the DBR temperature). We achieve maximum conversion efficiency using a poling

period of 6.90 μm (the center grating), operated at a temperature between 48-52^o C (input power-dependent).

As a single-pass configuration, the optical design of the SHG apparatus is minimal. The amplifier output coupler is held in a rotation mount and two high-reflectors direct the collimated output beam through an aspheric lens towards the PPLN crystal. The lens has a focal length of F=13.86 mm (Thorlabs C560TME-C) and is mounted on a 1-dimensional translation stage (parallel to the beam axis) to allow for precise alignment of the waist location. According to [72], peak theoretical conversion efficiency is achieved when the beam is focused such that for crystal length L, $z_R = 5.68L$, i.e. when the Rayleigh range is nearly six times the crystal length. For our crystal length and input beam, this corresponds to a lens with focal length F=16 mm. Since no such lens was available, we instead tested a range of focal lengths and settled on the one which delivered the highest empirical efficiency.

The crystal itself is mounted (along with the heater resistor) on a small section of bare FR-4 circuit board as a thermal insulator and clamped to a tip-tilt mount which is in turn mounted to a 1-dimensional translation stage. The stage is mounted perpendicular to the beam axis, which allows us to switch between different poling periods in the crystal without realigning the rest of the system. The additional two axes of adjustment provided by the tip-tilt stage are not, strictly speaking, necessary, but help to simplify the process of optimizing the doubler output. In the future, however, the extra stage may be omitted in the interest of simplicity and stability.

After exiting the crystal, the combined 1062/531 nm beam is recollimated by an aspheric lens that is AR coated for 531 nm and has a focal length F=11

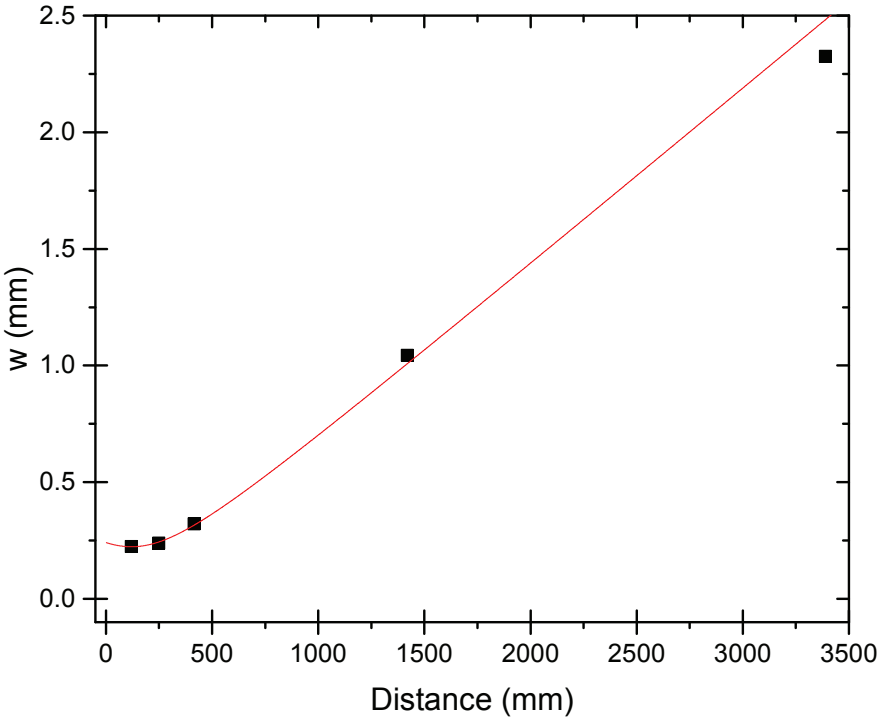

Fig. 4.2: Measured $1/e^2$ beam radius of the 531 nm doubler output as a function of distance from the doubler housing. The solid curve is a theoretical beam profile for a Gaussian beam with waist radius 0.2235 mm located 120 mm in front of the doubler housing.

mm. The collimated beam has a waist diameter of 0.447 mm located ≈120 mm outside the doubler housing and has a measured divergence angle of $\theta_{1/2} = 0.686$ mrad (see Fig. 4.2).

The output power of the doubler scales roughly quadratically with input power (see Fig. 4.3). At low pump power we observe a conversion efficiency on the order of 1.8%, increasing to a maximum of 12.5-13% conversion efficiency—corresponding to outputs of 18 mW at 1 W and 1.25-1.3 W at 10 W pump powers.

The conversion efficiency is governed by the relation

$$P_{out} = \eta P_{in}, \tag{4.2.1}$$

where the conversion efficiency,η, is itself a function of the input power, P_{in}; crystal length, L; and a weakly varying conversion scaling factor, α:

$$\eta = \alpha L P_{in}. \tag{4.2.2}$$

The conversion factors observed for our system were consistent with the factors of 2%/W·cm at low power and 1.5%/W·cm at high power that were observed by Covesion in their internal tests [73]. In addition to input power, these conversion factors are also implicitly dependent on system alignment and optical losses. See appendix E for alignment notes and procedures for the doubler.

4.3 CaF Internal Energy Structure

The energy structure of the $B - X$ transition in CaF is shown in figure 4.4. As stated in Sec. 3.2.1, the (0,0) band of the $B-X$ transition has a Franck-Condon factor (FCF) of 0.999, and for that reason was chosen as our BCF transition. Due to the relatively short interaction time of our experiment, the high FCF alleviates the need for a vibrational repump as essentially no population should be lost into the dark, $X(v = 1)$ state. Within this vibrational band, we excite the closed $N = 1 \rightarrow N' = 0$ rotational transition corresponding to, in Hund's case (a), a combination of the $P_{11}(3/2)$ and ${}^{P}Q_{12}(1/2)$ transitions. Thanks to the $N' = 0$ upper state, this transition is closed by selection rules, but carries with it the complication of higher ground-state multiplicity. Thus, while we do not require a

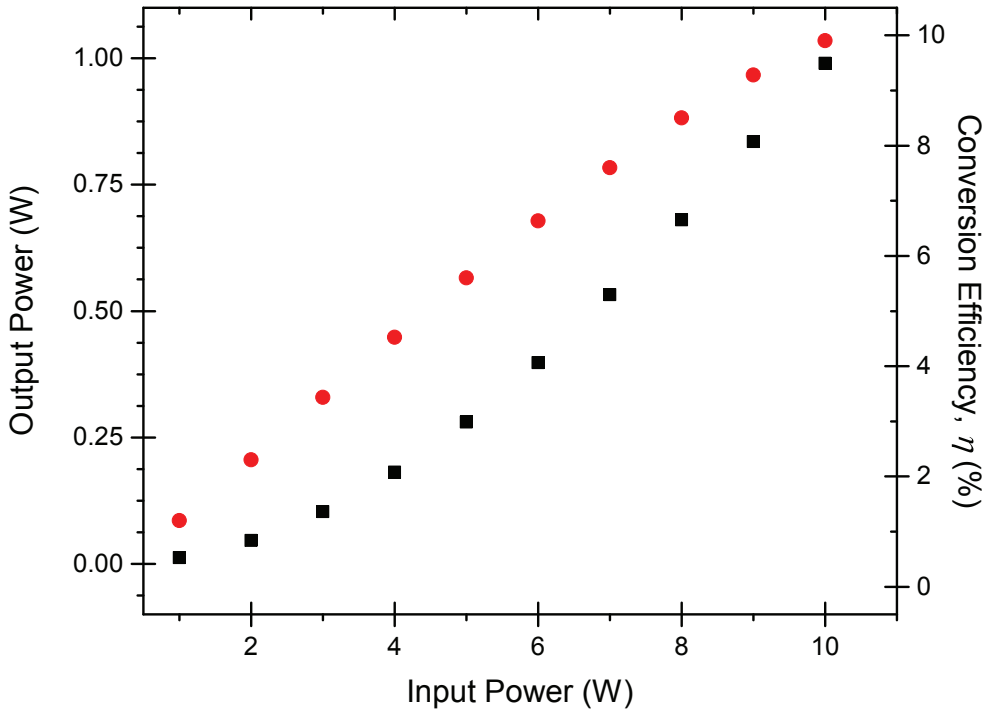

Fig. 4.3: Measured 531 nm output power and conversion efficiency, η, from the doubler plotted as a function of input 1062 nm power. The data were recorded after installation of the F=13.86 mm input aspheric lens, but before the system was fully optimized. With improvements subsequent to this data, the total output power at 531 nm for 10 W of input power is now $\sim$1.3 W, corresponding to a conversion efficiency of 13%.

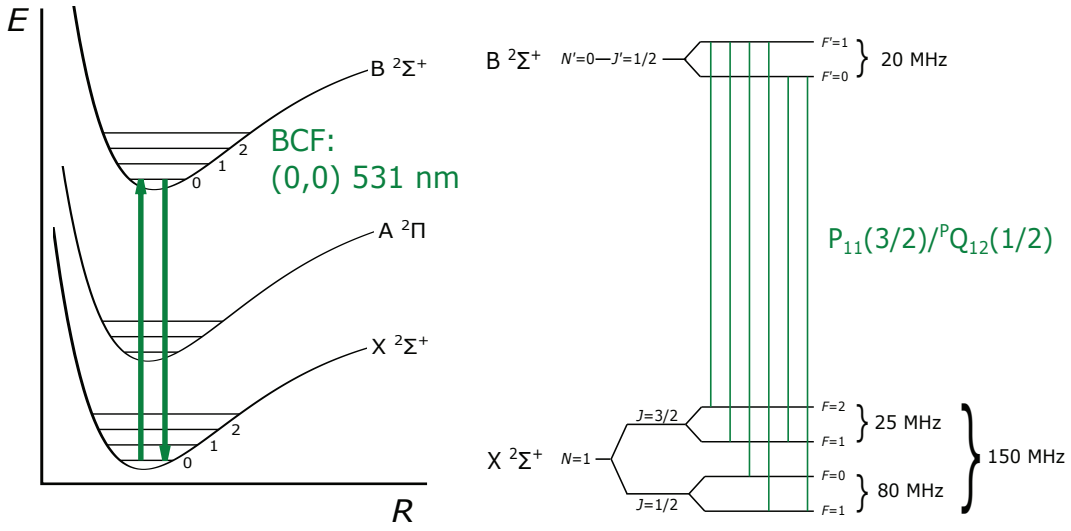

Fig. 4.4: Energy diagram for the CaF $B - X$ transition used for the BCF. The (0,0) vibrational band at 531 nm (at left) is essentially closed due its Franck-Condon factor of 0.999. The $N = 1$ to $N' = 0$ rotational transition ($P_{11}(3/2)/^{P}Q_{12}(1/2)$) is closed due to selection rules, but the higher ground-state degeneracy does give rise to hyperfine dark states.

rotational repump laser, we do need a way to recapture population lost to dark hyperfine states.

For linearly polarized light (as we use in this experiment) the $m_F = \pm 2$ states are inaccessible and thus will accumulate population as a result of spontaneous decays. The simplest solution is to use a skew-angled magnetic field to break the azimuthal degeneracy of the ground hyperfine states. Theoretical modeling of the system [37] suggests that optimal remixing occurs for a magnetic field of 29.2 Gauss set at an angle of 71^o with respect to the laser polarization. To apply the field, we constructed and installed a set of Helmholtz coils. The coil current is carefully calibrated to deliver a field of exactly 29.2 Gauss, as measured in the center of the interaction chamber. To set the skew angle, rather than attempting

to rotate our coil assembly, we instead chose to install the coils with their field parallel to the laser polarization, and then used a $\lambda/2$ plate to rotate the laser polarization by the necessary 71^o.

Due to the relatively large ground-state splitting of 150 MHz [56] (see Fig. 4.4), care must be taken in choice of bichromatic detuning. The lifetime of the B state is 25.1 ns, i.e. $\Gamma = 2\pi(6.34 \text{ MHz})$ [45, 58]. It follows then that the ground-state splitting corresponds to a interval of $\approx 24\Gamma$. Operating in the large detuning limit of the BCF requires a bichromatic detuning larger than this interval, but due to the intensity requirement imposed by Eqs. 2.4.1 and 1.1.6, we are not able to simply increase the detuning freely. As a compromise, we operate at a detuning of $\delta = 30\Gamma = 2\pi(190 \text{ MHz})$ with optimal Rabi frequency $\Omega_r = \sqrt{3/2}\delta = 2\pi(232.7$ MHz). Combining Eq. 1.1.6 with 2.3.4, we find that the Rabi frequency driving each of the four excited-state levels in our transition is given by

$$\Omega_r = 2\pi\sqrt{\frac{I}{3}}(60 \text{ MHz}), \tag{4.3.1}$$

for I in units of W/cm^2 and where, recall from Sec. 2.3, $\Omega_r = \Omega_r^i = \Omega_r^j$. The factor of $1/\sqrt{3}$ is a geometric factor arising from the coupling between the m_F levels within each of the four excited-state transition manifolds. The derivation of this factor is beyond the scope of this dissertation, but details can be found in [37]. For our optimal Rabi frequency of $\Omega_r = 2\pi(232.7$ MHz), we find this corresponds to an intensity of 45.2 W/cm^2 per bichromatic frequency component.

4.4 Bichromatic Frequency Production

After generating the 531 nm light, we then convert our monochromatic beam into a bichromatic beam. A pair of AOMs is used to generate the symmetrically detuned components. Each component is independently resized and refocused before being coaligned and combined on a beamsplitter. The combined beam is refocused by an adjustable telescope before being sent through the experimental chamber. The relative phasing between beatnotes is set by varying the path length via a traveling plane mirror configured as a retroreflector. The frequency of the laser is locked to a molecular iodine resonance via a 3-beam saturated absorption spectroscopy setup, similar to that used for the detection laser.

4.4.1 Cascaded AOMs

We considered several different schemes to generate the symmetrically detuned frequency components necessary for BCF. The solution we settled on was to use a pair of cascaded acousto-optic modulators (AOMs) (see Fig 4.5). This configuration allows us to maximize the power delivered to each frequency component and—turning an eye towards future experiments—gives us two independent bichromatic beams to work with. For now, we only need a single bichromatic beam, which is retroreflected, but the second beam is useful as an alignment tool.

As implied by the description, the cascaded AOMs work in two steps. The first step shifts the frequency of the main beam up by $\delta = 2\pi(190\text{ MHz})$ using the +1st-order of the AOM. The diffraction efficiency in this stage is intentionally attenuated by detuning the angle of the beam away from the Bragg angle. Tuning of the input angle serves two functions. First, it allows us to balance the power delivered to each frequency component of the beam in real time. Second,

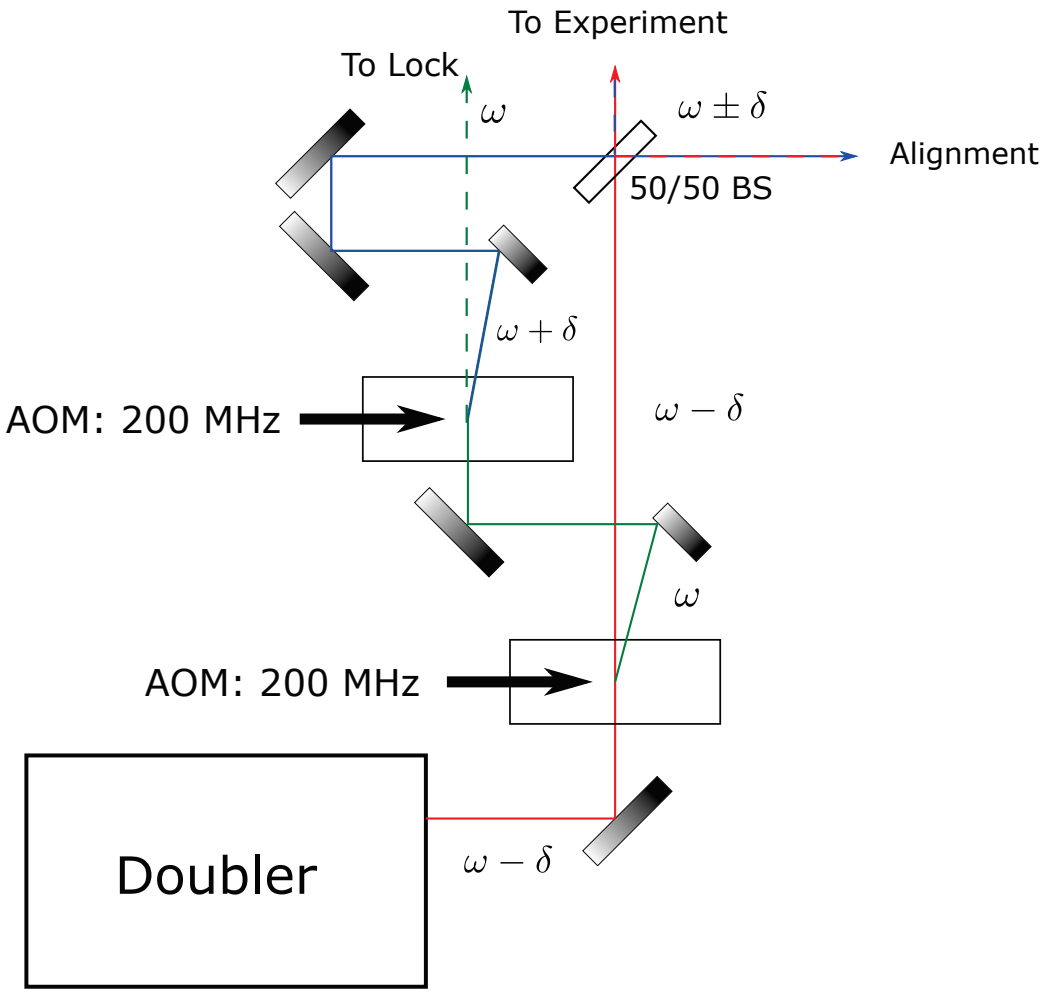

Fig. 4.5: A schematic diagram of the cascaded AOM scheme used to generate the $\omega \pm \delta$ frequency components needed for the BCF. The output of the doubler is set to be $\omega - \delta$ before entering the first AOM. The AOM is driven at the detuning frequency, δ, and intentionally set to a diffraction efficiency of $\sim$50%. The +1st-order diffracted beam (at ω) is upshifted by the second AOM to produce the $\omega + \delta$ component which is combined with the residual 0th-order $\omega - \delta$ from the first AOM to form the beat notes. Residual undiffracted ω from the second AOM is used for locking.

tuning away from the Bragg angle reduces distortion of the 0th-order beam mode structure [9], allowing for better spatial overlap of bichromatic frequency components. The 0th order beam from the first AOM is used as the negatively-detuned frequency component, $\omega_0 - \delta$, and is sent directly to the mixing beamsplitter.

The +1st-order diffracted beam from the first AOM—at frequency ω_0—is directed into the second AOM. The second AOM upshifts the input frequency by the detuning, δ, again to produce a +1st-order beam with frequency $\omega_0 + \delta$. Unlike the previous AOM stage, this AOM is tuned to have maximum diffraction efficiency—on the order of 85-90%—in the +1st-order beam. The positively detuned beam is then directed by a series of mirrors to the mixing beamsplitter. The residual 0th-order beam at ω_0 is used for frequency stabilization (see Sec. 4.4.4).

The AOMs are driven by a common frequency synthesizer with independent amplifiers. The frequency synthesizer is a home-made design (see appendix A) which outputs a 190 MHz signal at 13 dBm. The output is split by a Mini-Circuits RF splitter and each of the split outputs is sent to a Mini-Circuits amplifier. The amplification is adjusted for each AOM individually to maximize diffraction efficiency. The amplifier gains are set by yet another home-made microcontroller-based circuit (see appendix A). The adjustable output voltage source has dual independent outputs, is adjustable from 0-5 V with 1 mV resolution, and has a selectable coarse/fine adjustment range.

4.4.2 Beam Sizing

Concurrent with the power balancing of the two frequency components, the stringent intensity requirements of the BCF also mean that close attention has to

be paid to the sizing of the combined bichromatic beam. An adjustable telescope is used to regulate the size of the beam as it enters the interaction chamber. The telescope assembly can be moved, as a whole, along a dovetail rail to adjust the location of the beam waist. The spot size of the bichromatic beam is then adjusted by tuning the telescope lens spacing via a micrometer adjustment on the front lens. This arrangement allows the intensity in the interaction region to be tuned in real time to compensate for fluctuations in the doubler output power. In order to maintain the 45.2 W/cm^2 required for our $\delta = 30\Gamma$ detuning, typical beam sizes are on the order of 0.5x0.8 mm, oriented along the y- and z-axes, respectively (as shown in Fig. 4.6).

4.4.3 Phase Adjustment

Setting the relative phase between beat note trains is relatively straightforward. The phase is adjusted using a delay line to vary the travel time between the left-going and right-going pulse trains. Experimentally, this is accomplished by putting a retro-reflecting mirror on a dovetail rail and adjusting the path length.

While sound in principle, in practice this setup conflicts with the Gaussian properties of our laser beam. Due to space restrictions, the beam waist ends up just outside the entrance window to the interaction chamber such that by the time the beam has completed its round trip the returning beam had expanded slightly. For short path lengths, corresponding to phases $\chi \sim 90^o$ or less, this slight intensity asymmetry has a minimal effect on the realized BCF force. However, for larger phase differences, this intensity imbalance becomes non-negligible. In particular, for $\chi = 135^o$ the extended delay line results in a return beam that is $\sim$30% lower peak intensity than its counter-propagating partner.

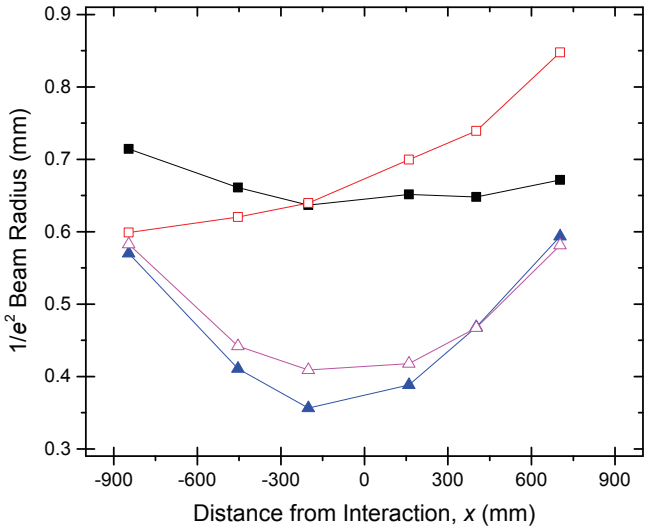

(a)

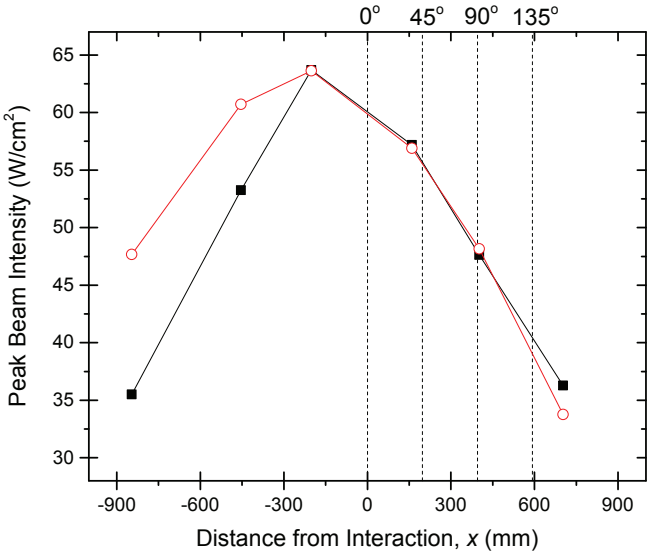

(b)

Fig. 4.6: (a) Measured beam sizes for the $\omega_0 + \delta$ (open symbols) and $\omega_0 - \delta$ (closed symbols) BCF component beams as a function of distance from the center of the interaction chamber ($x = 0$). (b) Peak beam intensities as functions of distance for the $\omega_0 + \delta$ (open symbols) and $\omega_0 - \delta$ (closed symbols) beams computed from the dimensions in (a). The vertical dashed lines show the optical path lengths for the indicated BCF phases.

To ensure overlap of the forward and reverse beams, a series of apertures are set up as guides. The apertures are aligned vertically to the CaF beam using a two-step process. First, the PMT was scanned vertically while the CaF beam was imaged without the internal 0.76 mm slit in place. The PMT was then placed at a height corresponding to the peak density of the molecular beam. The detection beam, tuned to the non-cycling $A - X$ (1,0) band, was then resized and redirected through the interaction chamber to deplete the ground-state beam population. By vertically scanning the depletion beam through the interaction region, the maximum depletion—corresponding to maximum CaF density—can be located. A pair of irises, on the input and output windows of the interaction chamber, are placed to mark the optimal path for the depletion beam through the interaction region, and subsequently used to align the forward-propagating BCF beam. The counterpropagating reverse beam alignment is set by centering the beam on a separate iris, centered on the forward-directed beam, located before the adjustable telescope.

In an effort to counteract the aforementioned expansion-induced imbalance, we explored the possibility of adding a refocusing lens to the retroreflected beam arm. The introduction of the lens, however, led to ambiguity in the alignment of the return beam. Specifically, the alignment of the retroreflected beam became (apparently) insensitive to adjustments to the retroreflector's pointing.

4.4.4 Frequency Stabilization

Thanks in part to the high intensity of the BCF beams and the inherent stability of the DBR oscillator, frequency stabilization of the 531nm light is reasonable straightforward. Using the residual 0th-order from the second AOM means

that our locking beam is at ω_0 and thus we maintain a fixed lock-point regardless of detuning. As was the case for our detection beam, we again choose to stabilize our laser via a molecular iodine reference transition.

After leaving the AOM, the 0th-order locking beam is sent through another AOM. This additional AOM is configured in a double-pass configuration and shifts the locking beam frequency higher by 250 MHz each pass. The shifted beam has a frequency coincident with our reference line, and the diffraction through the AOM has the secondary benefit of partially scrambling the spatial mode of the beam. While it does not produce a perfect $\mathrm{TEM}_{0,0}$ mode, the scrambling does help to fill in some of the depletion caused by the previous diffraction stage. The beam is vertically polarized before being used for spectroscopy in a 3-beam setup (duplicating the detection beam locking configuration described in Sec. 3.3.3).

The double-passed AOM is driven by the same type of home-made frequency synthesizer used for the BCF AOMs and the detection locking AOM, amplified by the same type of home-made amplifier used for the detection beam locking AOM. Unlike the detection locking AOM, however, this AOM is driven with a fixed frequency of 250 MHz. The frequency dither required for locking is supplied to the DBR oscillator itself via a modified version of our lock-in circuit (see appendix A). This version makes use of the spare instrumentation amplifier to add an adjustable modulation clock on top of the scanning/locking ramp sent to the DBR. Using a 10 kHz dither rate, the magnitude was empirically adjusted to maximize the lock signal-to-noise ratio. The final modulation depth of 2 MHz is negligible compared to the BCF detuning.

The iodine transition that we lock to is a combination of the I_2 $B - X$ (32,0) band $R(11)$ and $P(8)$ rotational transitions near 18832.460 cm^{-1}, shown in

Fig. 4.7. It is a fairly weak transition, and thus requires a fair bit of intensity to properly saturate it. Empirically, a pump beam of at least ∼5 mW is typically required to generate sufficient error signal to establish a reliable lock. Small fractions of the pump beam are picked off to generate the probe and normalization beams, as usual, before being loosely focused by a long focal length lens. The lens focuses the beam near the center of the iodine cell where it crosses the probe beam at a small angle. To collect the spectrum, we use a New Focus Nirvana auto-balancing gain photodiode (Newport Model 2007). The Nirvana is a commercial version of the home-made auto-balancing detector we use to generate our detection lock error signals. The difference signal from the Nirvana is used as the input to our dither-enabled lock-in detector. The internal PID capabilities of the lock-in circuit lock the DBR frequency based on empirically set PID loop gains. No quantitative measurements of stability have been performed on this lock, but it has been observed to maintain lock for hours at a time.

4.5 Data Acquisition

Experimental data is acquired using an NI-6063E data acquisition card via a BNC-2020 terminal block. Initial experiments used a dual-boxcar scheme to collect the peak LIF signal, averaged over a period of 300 shots. This scheme was later discontinued in favor of direct acquisition of the LIF time-of-flight (TOF) signal. Coincident with the switch to TOF acquisition was a corresponding switch of acquisition programs.

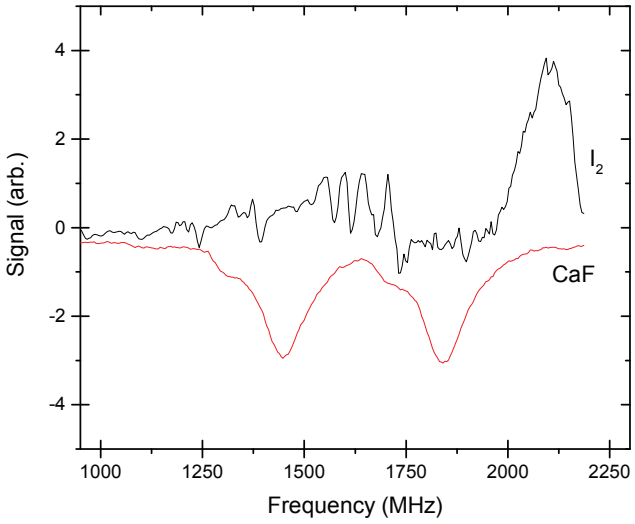

(a)

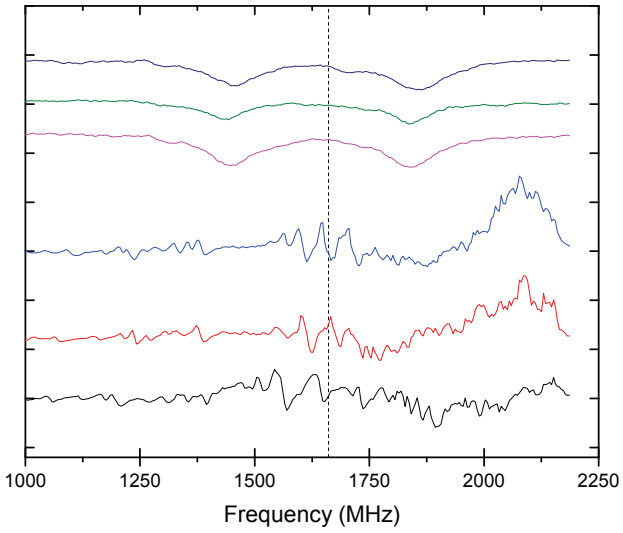

(b)

Fig. 4.7: (a) An average of 6 frequency scans of the CaF $B - X$ (0,0) $P_{11}(3/2)/{}^{P}Q_{12}(1/2)$ transition and the I_2 reference line we use for locking. The reference line is a combination of the $R(11)$ ($J = 11 \rightarrow J' = 12$) and $P(8)$ ($J = 8 \rightarrow J' = 7$) rotational transitions within the $B - X$ (32,0) vibrational band, located at 18832.4416 cm^{-1}. The peaks in the CaF signal are the $\omega_0 \pm \delta$ components of the BCF beam. (b) Raw scans of the same transitions, offset for clarity. The vertical dashed line indicates the approximate lock point used for frequency stabilization.

4.5.1 Original Scheme

Initial experiments used a pair of boxcars (SRS-250) for LIF acquisition. The gate of one boxcar was set to coincide with the maximum of the LIF signal ("signal"), and the gate of the other was set at a time long after the signal disappeared ("background"). Both signal and background boxcars were setup with identical parameters: 15 μs gate width, 300 shot average, and no DC offset. Input sensitivities were also matched and adjusted day-to-day to account for signal fluctuations. The LIF signal and background were collected along with several accessory signals: detection lock error signal, detection probe absorption, fiber-coupled detection power, BCF lock error signal, and BCF probe absorption.

The front-end user interface for the acquisition process was a LabWindows program originally meant for collecting spectral scans. The program collected a single data point from each input channel on every shot and wrote it (live) to a scrolling chart display. After completing acquisition, the data were written to a TDMS file format.

The principal flaw of this scheme lies in the limited gate width of the boxcars. The original 15 μs gate window was far too narrow to collect the full 200 μs signal, and fluctuations in arrival time of the CaF pulse added significant fluctuation to the collected data. Even after modifying the boxcar circuitry to allow a 150 μs gate, timing jitters on the order of tens of microseconds still made single-point boxcar acquisition too noisy to reveal clear results.

4.5.2 Revised Scheme

Getting around the issue of signal timing jitter is simply a matter of collecting a wider signal window—the logical extension of this being to collect the entire

signal. Instead of collecting a narrow signal window via boxcar, we switched to acquiring the full TOF signal. Hardware-wise, the change is more-or-less trivial. Rather than feeding the PMT output into the boxcar input, the output of the PMT TIA is directly connected to a DAQ input. A second amplifier stage was eventually added to boost the signal, but no changes were actually required to the acquisition hardware. As stated previously, the TOF signal has a width on the order of 200 μs and occurs approximately 1 ms after the pulsed valve fires. Using the pulsed valve sync signal as a trigger, we collect 3 ms worth of data. This acquisition scheme allowed us to define an arbitrarily large digital averaging "gate" in post-processing such that we can ensure collection of the full LIF signal. Full TOF acquisition also gives us a much larger sample of background data to consider, and thus a more accurate picture of the steady-state behavior of the system. Though it was not our original intent, perhaps the biggest benefit of TOF acquisition was that it allowed us to much more easily examine the behavior of the signal fluctuations on an individual-shot basis.

4.5.3 LabView Program

In concert with the change of acquisition scheme was also a change in acquisition program. The older program was never intended to acquire multiple datapoints per trigger and had no provisions for modifications of that type; any modifications would have to be done on an ostensibly fundamental level. Rather than tear apart an existing program, it proved faster to simply build a new program from scratch. Using a program for acquiring metastable helium data [9] as a rough template, I wrote a new LabView program to acquire CaF TOF data. A full description of the program is available in appendix C, but the framework is

as follows.

Since the TOF signal is time-sensitive, it is the first data to be acquired after the trigger signal. The amplified PMT output is directly sampled by the DAQ over a 3 ms period following the trigger and written to an internal (pre-allocated) data array. By configuring collection on a single channel, it allows access to the full sampling speed of the DAQ card. After the TOF data have been collected, the remaining inputs are sampled once per channel. These signals are accessory diagnostic data that are not time critical. Just as was the case in the previous detection scheme, monitors of detection beam power, detection/BCF lock error signals, and detection/BCF probe absorption signals are all collected for future reference (if necessary). Optionally, shots can be averaged together to compress the dataset, but single-shot acquisition was found to be more useful. After the data trial has completed, the data are written to a user-specified output TDMS file.

With the boxcars no longer in use for primary signal collection, they were repurposed for collection of a normalization signal. The hope was that a shot-by-shot normaliztion would help to account for CaF flux variations and improve the signal-to-noise ratio of the data. A secondary detector, a SensL silicon photomultiplier (SiPM), was added to the detection region, perpendicular to the beam axis (along y). By imaging the area in front of the spatial filter slit, it should be able to acquire the full spatially independent LIF signal for each shot. This data could then be used as a normalizing factor. The boxcars are configured on the secondary detector in much the way as they had been previously on the PMT: one gate located at the signal peak, the other long after the signal is gone. The boxcars are configured for single-shot (non-averaging) acquisition and the outputs fed

into a differential amplifier before being collected by the DAQ. Unfortunately, the signal collected by the normalization detector proved to be too low and too noisy to correlate signal fluctuations with CaF flux variations. Without the time to devote any significant development/debugging time to the normalization detector, it became more of a curiosity than a useful signal metric.

4.5.4 Beam Shutter

As a final measure to attempt to reduce signal fluctuations, a shutter was added to the BCF beam line to alternate between deflected and undeflected shots. Prior to the shutter's installation, data was collected in complete runs of deflected vs. undeflected. The combination of the shutter and single-shot acquisition would allow us to compensate for long-term signal magnitude and timing drifts by collecting nearly-simultaneous shots of each parameter set. In addition, this would also allow us to bin shots in post-processing in order to isolate fluctuations on different time scales. To ensure the collection remained synchronized, the sync output from the shutter driver is collected. An internal counter within the program writes to a binary breakout output—using the least significant bit as a sync pulse to the driver allowed the shutter to be switched every-other shot.

The anticipated benefits of this scheme could not be fully realized, however, due to the small number of photons collected per shot. Photon counts on the order of 1 per shot mean that random shot-noise variations in the photon count will dominate the noise spectrum. Since these variations are time-independent, no amount of time binning will be able to properly isolate them, defeating the purpose of the binning altogether.

Chapter 5

Deflection Experiment: Analysis

In order to test the performance of the BCF on our molecular beam, we perform deflection tests on the beam under three different phase conditions while holding the other bichromatic external field parameters constant. The expected periodic variation of force with respect to phase is a unique identifying characteristic of the BCF, not present in radiative or dipole forces, which will allow us to positively identify the action of BCF on the molecular beam.

The bichromatic detuning was chosen to be $\delta = 30\Gamma = 2\pi(190\text{ MHz})$ for all of the experiments performed. This detuning was chosen because of a combination of technical and theoretical considerations. The detuning of $\delta = 30\Gamma$ is sufficiently high that we are able to operate in the large-detuning regime of the BCF (as discussed in Sec. 2.4.2,4.3), but the intensity required to maintain the condition $\Omega_r = \sqrt{3/2}\delta$ is low enough, given our power budget, to allow a force which would address a significant fraction of the molecular beam. From a more practical standpoint, this detuning is also compatible with the 200 MHz AOMs we already had in stock in the laboratory, which made it an appealing starting point.

The peak intensity of the field is set to 60 W/cm^2 per frequency component for a total intensity of 120 W/cm^2 incident on the molecular beam from either side. This peak intensity is above the ideal intensity for the BCF. Recall from

section 2.4.2 that for the large detuning regime the force is maximized when the Rabi frequency meets the condition $\Omega_r = \sqrt{3/2}\delta$ (Eq. 2.4.1). From Sec. 4.3, we note that the optimal Rabi frequency for $\delta = 30\Gamma = 2\pi(190\text{ MHz})$ is given by $\Omega_r = \sqrt{3/2}\delta = 2\pi(232.7\text{ MHz})$ which, according to equation 4.3.1, corresponds to an intensity of 45.2 W/cm^2. Thus, if the force beams were uniform, an intensity of 60 W/cm^2 would result in a less than optimal applied force on the molecular beam. The force beams are, however, not uniform, but rather have Gaussian spatial modes. This leads to a strong spatial dependence of the intensity and thus, the force. As discussed in Sec. 2.4.3, for a Gaussian beam, matching the peak intensity to the ideal condition means that only a very small area of the beam is at ideal intensity, and maximizing the force over the entire interaction volume requires overshooting the ideal intensity. Through modeling of a two-level system, we found that the effective force was maximized for a peak intensity exceeding the ideal intensity by 33%, i.e. 60 W/cm^2.

With this fixed input intensity, we test three phases: $\chi = 45^o$, $\chi = 90^o$, and $\chi = 135^o$. These phases correspond to maximum force, no force, and inverted maximum force, respectively. The phase is set by adjusting the distance between the molecular beam and a retroreflector: 98.6 mm for $\chi = 45^o$, 197.2 mm for $\chi = 90^o$, and 295.7 mm for $\chi = 135^o$, corresponding to delay line lengths of 197.1 mm, 394.3 mm, and 591.4 mm, respectively.

5.1 BCF Deflection Results

Results for the different phases are seen in Figure 5.1. These data are aggregated averages over many days of acquisition. Each day consists of 10000 shots at each position, gathered over multiple trials in a random sequence to

avoid systematic signal drifts. Our earlier data were acquired using rounds of 5000 shots at each condition—with BCF at a given phase or phases and without BCF—at each position. The positions are cycled through in a random order and after every position is sampled once, acquisition is repeated in a new random position sequence. The data are combined in post-processing into a single 10000 shot dataset and statistics are computed on the aggregate data. Our later data were acquired with a slightly-modified collection scheme. An electronic shutter is used to switch between blocking and passing the BCF beams on alternating shots within a single 5000 shot period. These datasets collect 5000 total shots at each deflection phase condition—2500 shots without BCF, 2500 shots with BCF at a given phase—at each position, and is repeated 4 times with random sequences of positions. The net result after combining the datasets in post-processing is a total of 20000 shots at each position for the undeflected beam data, and, again, a total of 10000 shots at each position for each BCF deflection phase condition. Since the repetition rate is fixed at 10 Hz, the long acquisition time for each dataset limits the number of phase conditions which can be collected in a given run, to $\sim$3 BCF phase conditions (plus undeflected) for the older static acquisition scheme or $\sim$2 BCF phase conditions (plus undeflected) for the newer shuttered acquisition.

The data from each day are compiled together into a single dataset and statistics are computed across the full dataset as a function of position. The average signal values at each position, for each condition are plotted in Figs. 5.1(a)-(c); the accompanying error bars are the standard deviations of the mean values, also computed across the total compiled dataset. Due to the time constraints involved with the acquisition process, we are not able to take data for every condition on every day. The undeflected beam data, which is collected every day, is an aggre-

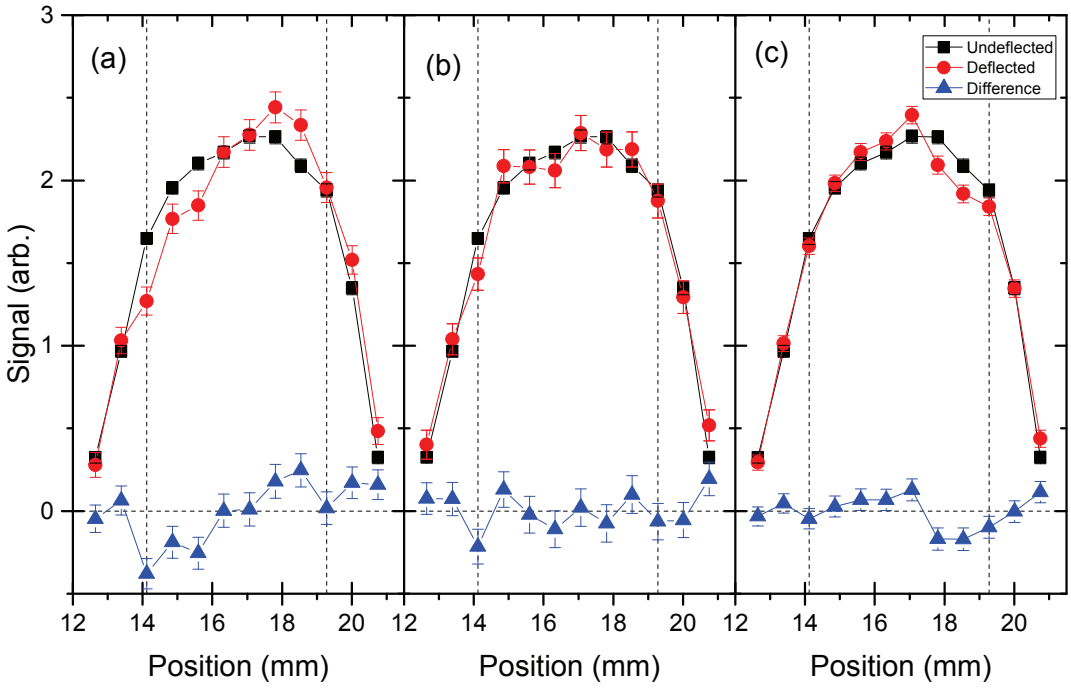

Fig. 5.1: The measured CaF beam profiles for three different deflection conditions: (a) $\chi = 45^o$, (b) $\chi = 90^o$, and (c) $\chi = 135^o$. The signal at each position is given by the average signal from every day of collected data. Error bars are the standard deviation of the mean value at the given position. The profiles qualitatively agree with our expectations. Namely, the $\chi = 45^o$ shows positive deflection, $\chi = 90^o$ shows no deflection, and $\chi = 135^o$ shows negative deflection.

gate of 23 days of acquisition. The other BCF conditions are aggregates of data collected over 9, 8, and 11 days for $\chi = 45^o$, $\chi = 90^o$, and $\chi = 135^o$, respectively.

A cursory examination of the data reveal behavior largely consistent with our expectations. We note from Figure 5.1(a) that comparison of the beam profile for BCF with $\chi = 45^o$ shows a clear shift relative to the undeflected profile. Furthermore, the shift is in the $+x$-direction, as defined for our experiment, indicating a force which is aligned parallel to the input beam. For $\chi = 90^o$, depicted in Fig. 5.1(b), the nominally-deflected beam profile shows excellent agreement with the undeflected profile. This is again consistent with our expectations for the BCF with a relative phase $\chi = 90^o$ but is not in and of itself a conclusive demonstration that the BCF is present. The case of $\chi = 135^o$, as shown in Fig. 5.1(c), is not as clear. For this case we expect a shift equal and opposite of what is observed for $\chi = 45^o$ (Fig. 5.1(a)). This is not illustrated in the data, however. There is certainly evidence in Figure 5.1(c) of a shift present in the $-x$-direction, but the magnitude is obviously attenuated. One factor in this reduction is the significant intensity imbalance between the beat trains at this phase, as discussed in Sec. 4.4.3. This is discussed further in Sec. 5.3. Despite the lack of exact quantitative agreement, the figures do show qualitative agreement with our expectations for the BCF. In order to verify quantitative agreement, further analysis is necessary.

5.1.1 Control Conditions

In addition to the BCF conditions discussed above, we also test several control conditions. The purpose of these additional tests is to help verify that the observed deflections are in fact due to BCF and not a different or secondary phenomenon. The primary control conditions we test are for a single-frequency

standing wave and for a bichromatic traveling wave. We also collected some limited additional data for the BCF with $\chi = 45^o$ at reduced intensity.

Our data for the primary control cases are a combination of older data, taken during the initial testing phase, and 2 additional trials collected with the most recent generation of acquisition schemes. We ran out of experimental time so we were only able to collect a single dataset under the low intensity condition, but it is included for completeness.

5.2 Analysis

Table 5.1, below, summarizes the measured and modeled shifts for the conditions tested in the experiment. We find that at phases of $\chi = 45^o$ and $\chi = 90^o$ our theory and experimental measurements agree well. For the case of $\chi = 45^o$ in particular, we note that the average deflection is consistent with exact balancing between the beat note trains and exceeds what would be expected for the ordinary radiative force by a factor of $\sim$4. The case of $\chi = 90^o$ also shows excellent agreement with our modeling. As was noted for the raw data in Fig. 5.1(c) previously, the case of $\chi = 135^o$ agrees qualitatively with our modeling but does not show quantitative agreement. The deflection measured for $\chi = 135^o$ is in the correct direction, but the magnitude is reduced by a factor of ~ 3 from the ideal case model or a factor of ~ 2 from our dynamic imbalance model (discussed in Sec. 5.3.1). Coincidently, the deflection measured for $\chi = 135^o$ is consistent with a radiative force applied in the retroreflected beam direction, though this is highly unlikely to have occurred.

The control cases we examined are also in reasonable agreement with our modeling. The single frequency standing wave (SF) deflection is consistent with

Table 5.1: A summary of the experimental and simulated shifts for the BCF and control conditions tested. The measured BCF shifts at $\chi = 45^o$ and $\chi = 90^o$ as well as the control conditions for the single-frequency standing wave (SF) and bichromatic traveling wave (NR) agree well with the simulated shifts. The observed shift at $\chi = 135^o$ agrees with the simulated direction, but the magnitude of the shift is reduced by a factor of ∼2-3, depending on the particular model. The reduced intensity (RI) control point shows coincidental agreement with the simulated shift, but the large margin of error on the measured value makes comparison somewhat speculative.

	Experimental		Simulation		
Condition	Shift (mm)	Error	Ideal	Flat Imb	Dyn Imb
BCF, 45	0.145	0.029	0.130	0.112	
BCF, 90	0.021	0.031	0.000	-0.007	
BCF, 135	-0.045	0.019	-0.122	-0.106	-0.087
Control, SF	-0.007	0.030			
Control, NR	0.048	0.015	0.035		
Control, RI	0.094	0.124	0.093		

zero deflection and the bichromatic traveling wave in the no-retroreflector tests (NR) produces a shift consistent with the calculated radiative force. Thus, we are able to rule out either of these individual phenomena as being responsible for the shifts observed in the BCF data. Due to a time shortage, we were only able to acquire a single day of data for the reduced intensity (RI) BCF condition. As a direct consequence, the margin of error on our measured deflection—resulting from propagation of uncertainties of the individual position data points—is sufficiently large that no definitive conclusions can be drawn from the data. It is worth noting that the average measured deflection is very nearly equal to the modeled deflection, but this is almost certainly coincidental.

Based on this information, the data suggest that we are in fact able to deflect our molecular beam through the application of BCF. In doing so, we demonstrate not only that the BCF can be applied to molecular systems, but also that it

can be done with a magnitude that—when tuned to the correct parameters—can significantly exceed that of the radiative force.

5.2.1 Detector Imaging Function

During our analysis, careful attention was paid to the spatial region over which our signal is obtained. The LIF signal from the molecular beam is collected with a 1:1 telescope, meaning that our imaged region should be equal to the full 8 mm diameter active area of our detector. However, despite having matched lenses on either end, the telescope is not in the correct 2F spacing configuration. This degrades image quality away from the optical axis as non-axial rays are clipped by the finite system dimensions, thereby limiting our field of view. Even if this were not the case, it is clear from Fig. 5.1 that data are collected over a wider range than the 8 mm detector width. This was done intentionally in order to compensate for uncertainty about the location of the center of the molecular beam.

In order to determine where and how to constrain our data, we measured the imaging function of our detector. The results of the measurement are shown in Figure 5.2. We affixed a ground glass slide in the plane defined by our detection laser and illuminated it from behind via diffused flashlight sources. We then translated the slit across the full width of the detector, noting the response at each of the positions used for our deflection measurements. Using a combination of different light sources and diffusers, we construct an average response curve for our LIF detection as a function of slit position. In tandem with our measurements, we also performed rudimentary ray tracing modeling of the system as a verification. The measurements show a reasonably flat response centered at $x \approx 16$ mm, with a FWHM of ~ 6 mm. The ray tracing model agrees well with the measurements.

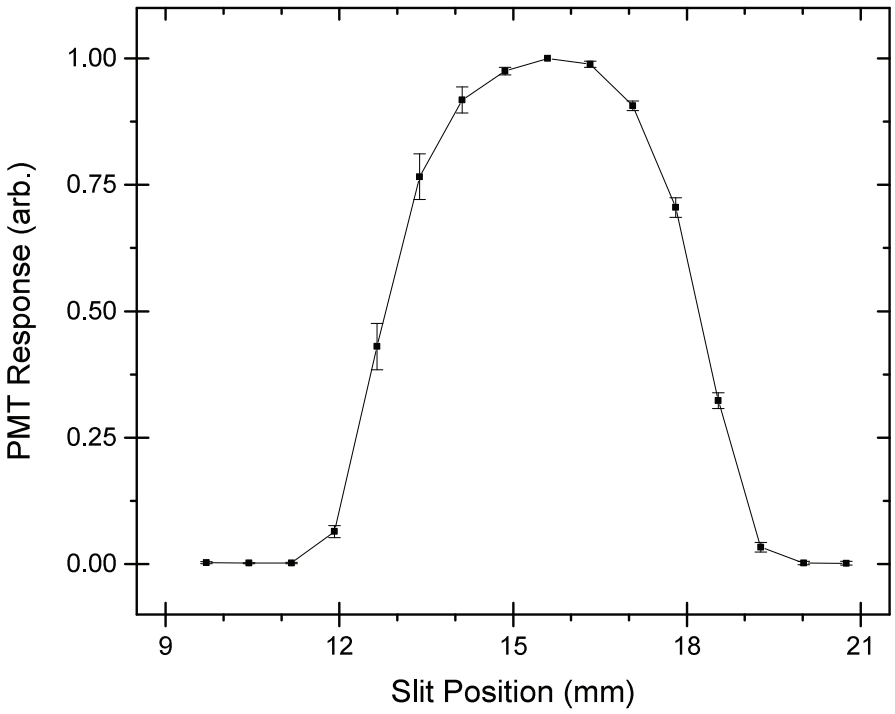

Fig. 5.2: The measured response of our detector as a function of position. The central region has fairly uniform response which drops off quickly at the edges. The width of this response area is approximately 6 mm, which sets the window over which we consider our beam deflection data.

Following this conclusion, we limit our analysis to the central 8 data points where the detector response is known, strong, and reasonably flat. This region is denoted by the dashed vertical lines in Figs. 5.1(a)-(c).

5.2.2 Computed Shifts

For each test condition, the shift is measured by computing and comparing the center of the deflected and undeflected beam profiles. Note that as discussed in Sec. 5.2.1, the data are restricted to the central 8 positions. The centers are

computed as a weighted average of the positions where the weights are given by the signal at each position, i.e.

$$\bar{x} = \frac{\sum_i S_i x_i}{\sum_i Si}, \tag{5.2.1}$$

where x_i is the slit position for the measurement and S_i is the signal at that position. The error for each center was computed as

$$\sigma_{\bar{x}}^2 = \frac{1}{\left(\sum_i S_i\right)^2} \sum_i \sigma_{S_i}^2 (x_i - \bar{x})^2, \tag{5.2.2}$$

where x_i is again the slit position for the measurement, $\bar{x}$ is the center position computed from Eq. 5.2.1, and $\sigma_{S_i}^2$ is the standard deviation of the mean for the signal at position x_i. The shift is then defined as the center of the undeflected beam subtracted from the center of the deflected beam (at a given condition), with error computed in the usual way for subtraction. The shift for each tested condition is shown in Figure 5.3 (squares).

5.3 Numerical Simulations

In order to contextualize the measured shifts and draw quantitative conclusions, we need to take into account the non-uniform intensity—and thus non-uniform force—which occurs within the experiments. To do this, we perform numerical simulations of our experiments under several different levels of approximation (see Sec. 5.3.1). For each phase condition of interest, force vs. velocity profiles are calculated at intensities ranging from 0 to 60 W/cm^2. At each intensity, the force is averaged over the relevant range of velocities corresponding to the collimation of the molecular beam, $\pm 1.5\Gamma/k \approx \pm 5$ m/s. When computing

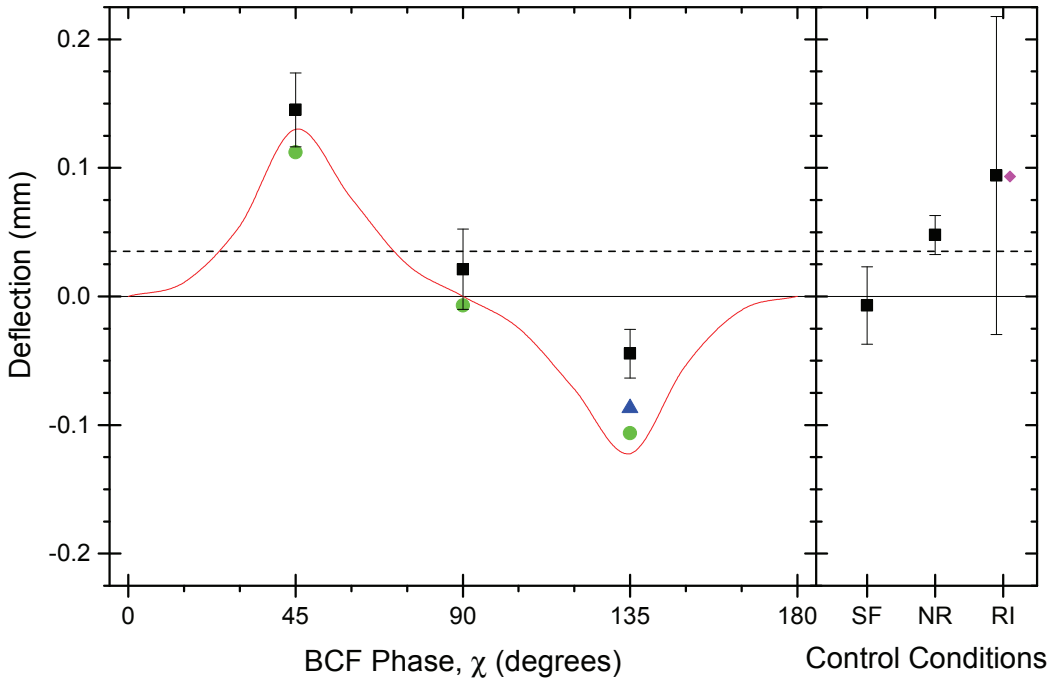

Fig. 5.3: The measured deflection as a function of relative BCF phase, χ is plotted (squares) and compared to various simulated models. The ideal model (solid curve) assumes perfectly matched BCF beams in the $+x$ and $-x$ directions, the flat model assumes equally sized BCF beams with a fixed peak intensity imbalance (circles), and the dynamic model uses measured BCF input and retroreflected beam intensities to take into account the changing imbalance over the span of the Gaussian BCF beams (triangle). The shifts measured for our control conditions are shown at right. The dashed horizontal line shows the calculated deflection for a radiation pressure force, computed as the 100% imbalance limit of our BCF force models.

this average, we choose to ignore the sharp positive-going features of the profile, reasoning that they would push molecules off of themselves before being able to impart a significant momentum transfer. To justify this choice, we estimate the time to move off of a spike, $\Delta t_{p\to b}$, and the time to move between spikes, $\Delta t_{p\to p}$, based on the force profile of optimized BCF at $\chi = 45^o$. We find that $\Delta t_{p\to b} \sim 0.4\mu$s while $\Delta t_{p\to p} \sim 4\mu$s is comparable to the BCF interaction time of $\sim 3.5\mu$s, indicating that the spikes likely contribute little to the total momentum transfer. Negative-going peaks were, by the inverse argument, retained.

To trim these peaks, we first compute an average, $\bar{F}$, and standard deviation, σ_F across the region of interest as normal. Any points within the region with magnitude $\geq \bar{F} + \sigma_F$ are clipped to $\bar{F}$, and the statistics are recomputed. This procedure is repeated until the average value converges. Averaging in this way results in an average force which is typically $\sim$10% lower than one which is computed directly.

The average force at each intensity generates a mapping, $F(I)$, which allows us to translate our measured input Gaussian beam profile, $I(z, y)$, into a force profile $F(I(z, y)) = F(z, y)$. The force profile, $F(z, y)$, is integrated over time using the substitution $t = z/v_{beam}$ on the interval $z \in [-2w, 2w]$, where w is the $1/e^2$ radius of the BCF beam in the interaction region. This yields the total change in x-momentum across the beam as a function of height in the molecular beam (y), i.e.

$$\Delta p_x(y) = \int_{-2w}^{2w} F(z, y) \frac{dz}{v_{beam}}. \tag{5.3.1}$$

A uniform coordinate grid is generated at the detection region, matching the size of the imaged area, and propagated backwards to the interaction region according to the parameters of the molecular beam divergence. The net momentum shift

was converted into a velocity shift vs. height and applied to the coordinate grid before re-propagating the now-deformed grid as well as a copy of the uniform grid back to the detection region.

Using the undeflected beam data, a population distribution is generated on the same uniform coordinate grid which had been propagated back to the interaction region. The distribution is given by $P(x,y) = P(x)P'(y)$, where $P(x)$ is the undeflected beam data and $P'(y)$ is a symmetrized version of $P(x)$. This distribution is mapped onto the deflected (warped) and undeflected (uniform) coordinate grids before being interpolated onto a uniform detection grid. The detection grid is integrated over height, y, in order to generate simulated signals: undeflected, $S(x)$, and deflected, $S'(x)$. Essentially, we perform the following operations:

$$\begin{aligned} S(x) &= \int I(x,y)dy = \int P(x)P(y)dy, \\ S'(x) &= \int I'(x,y)dy \\ &= \int P(x - F(y))P'(y)dy = \int P\left(x - \frac{\Delta p_x(y)\tau_f}{m}\right)P'(y)dy, \end{aligned} \quad (5.3.2)$$

where τ_f is the time of flight between the interaction and detection regions and m is the mass of CaF. From these simulated signals, the deflection is computed in the same way it was for the measured data (see appendix D for the complete code).

The deflection is plotted in Figure 5.3 as a function of phase for three different force models along with the experimental data. The same simulation procedure was also used to model the control condition case of no retroreflector—equivalent to the deflection from the radiative force. This deflection is plotted as

the horizontal dashed line across Fig. 5.3. The reduced-intensity control condition was also simulated and is indicated by the diamond in Fig. 5.3.

5.3.1 Imbalance Models

As a starting point for our modeling, we assume an essentially perfect experimental system with identical incident and retroreflected beams—exactly the same size and exactly the same intensity profile, regardless of phase. While this assumption is not a particularly realistic one for our experiment, it provided a baseline theory which we could later augment. This model—termed the "ideal" model—uses force vs. velocity profiles computed using the code taken directly from [37]. Using this model, deflection is simulated for phases ranging from $\chi = 0^o$ to $\chi = 180^o$ in 15^o intervals. The points were used to create the theoretical curve in Figure 5.3 (solid line), which illustrates the quasi-sinusoidal χ-dependence of the BCF.

In addition to the ideal model, we also consider the effects of non-ideal conditions on the BCF. In particular, we consider the effects of intensity imbalance between the input and retroreflected beams. The input beam is focused to a waist at the interaction region, and since it is Gaussian, it expands as it propagates away from this waist. Due to this expansion, even assuming no losses from the retroreflector optics, the retroreflected beam will always be slightly larger than the input beam and, therefore, will always have a lower average intensity. As the relative phase increases, the retroreflector delay line gets longer, and the imbalance is exacerbated. For the first two phases tested, $\chi = 45^o$ and $\chi = 90^o$, this expansion is a small perturbation. For $\chi = 90^o$ the imbalance is on the order of 15% which, according to a two-level model, should retain upwards of 90% of

the applied force (as calculated at $\chi = 45^o$ with ideal input intensity). Moving out to $\chi = 135^o$, however, the force begins to degrade much faster and imbalance becomes a potentially serious obstacle to the proper application of the BCF. Using the same two-level model with an estimated 30% imbalance—estimated from the measured beam sizes—the force drops by nearly 50% (as calculated at $\chi = 135^o$ with ideal input intensity). In an attempt to account for these detrimental effects, we modeled the imbalances within the system in two ways: the "flat" assumption and the "dynamic" model.

In the flat assumption, we make the approximation that the returning retroreflected beam is the same size as the input beam, but the intensity is reduced by the measured percent reduction caused by the beam expansion. This relationship is shown schematically in Figure 5.4. For $\chi = 45^o$, 90^o, and 135^o this corresponded to imbalances of 6.3%, 17.3%, and 30.7%, respectively. This approximation allows us to use the same input intensity profile, $I(z, y)$, in our simulation, and apply the imbalance through the force profiles used to generate the force map, $F(I)$. These profiles are computed using a modified version of the code taken from [37]; a summary of the modifications is presented in appendix B. The results of the simulation are shown in table 5.1 as well as in Fig. 5.3 (circles).

The flat model yields a force reduction of $\sim$10% for each of the phases examined. It is interesting to note that the $\chi = 135^o$ case, despite having significantly higher imbalance than $\chi = 45^o$, has roughly the same reduction in force. This arises from a subtle variation in the mapping $F(I)$ for each case. At the optimal intensity, the force for $\chi = 135^o$ is indeed reduced significantly more than the force for $\chi = 45^o$. However, the force map, $F(I)$, at $\chi = 135^o$ has a much flatter overall profile with more force at high intensity than the force map at $\chi = 45^o$, as

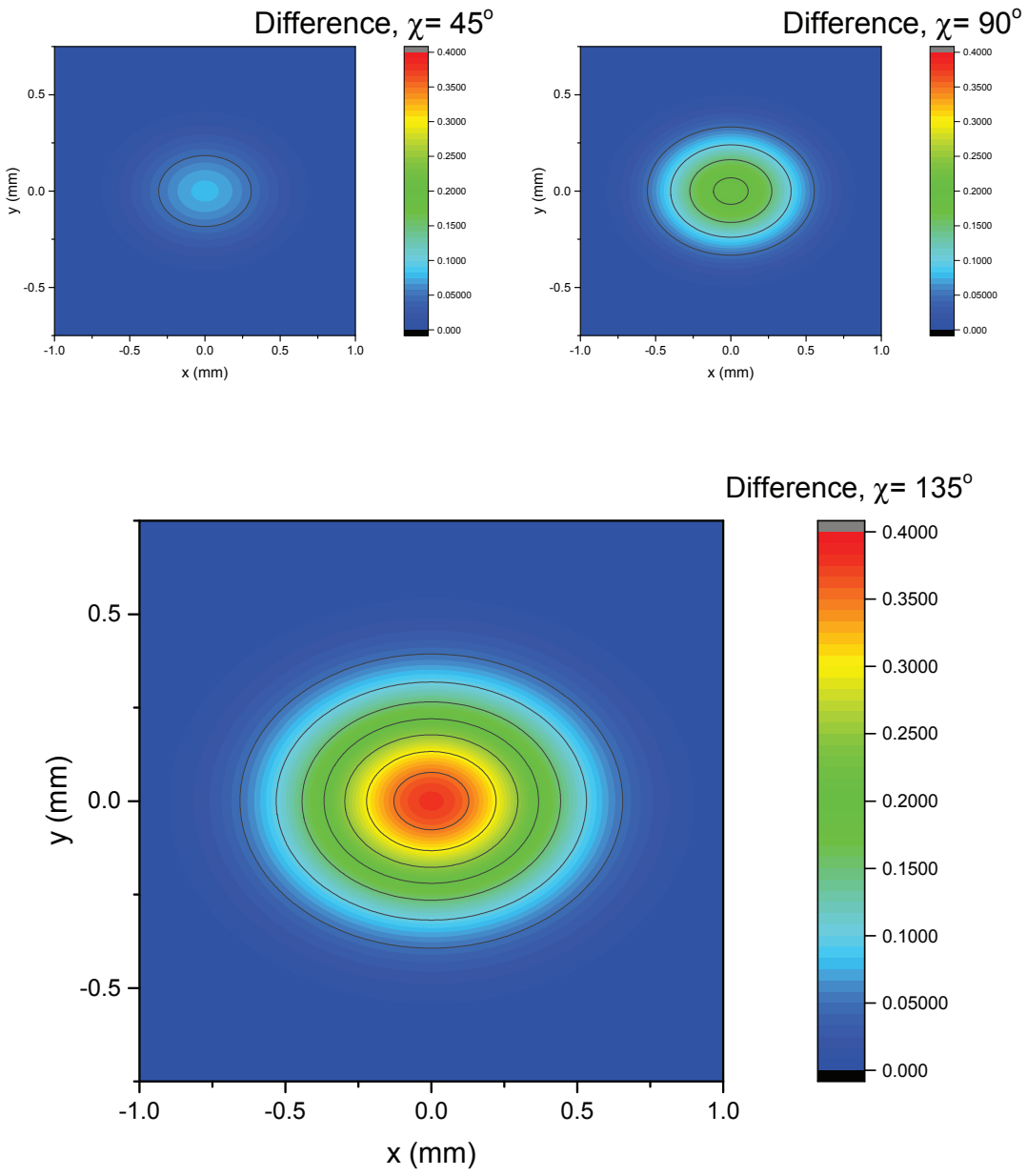

Fig. 5.4: Beam profile differences representing the assumptions of the flat imbalance model. The retroreflected beam is the same size as the input beam, but has its intensity reduced by a fixed percentage. The figure shows the difference between the input and retroreflected beams under this assumption for phases $\chi = 45^o$, $\chi = 90^o$, and $\chi = 135^o$ with a fixed color scale. Particularly for the case of $\chi = 135^o$, this is not an accurate model of the actual beam intensity profiles, but still allows us to take into account the effects of reduced BCF magnitudes caused by imbalanced intensities.

shown in figure 5.5. This means that despite having lower peak force, the force delivered by the BCF for $\chi = 135^o$ extends further into the high intensity region of the Gaussian beam. We find that this range extension effectively offsets the lower peak force. Thus, when we average over the full spatial profile of the Gaussian beam, we end up with nearly the same net deflection magnitude in each case.

Due to the apparent lack of explanation for the force reduction at $\chi = 135^o$, we progressed to a yet more realistic model. Upon further examination of the beam imbalances, we note that, particularly in the case of $\chi = 135^o$, the expansion of the retroreflected beam leads to a wide range of imbalances across the spatial profile of the overlapped beams. Near the center of the overlapped pair, the flat approximation is reasonably valid: for a small neighborhood centered on the peak intensities of the beams, the Gaussian profiles maintain a reasonably constant percent imbalance. Moving away from the peak intensity and into the wings, however, the input beam intensity begins to drop off faster than the expanded retroreflected beam intensity. This leads to a point where the intensities actually balance briefly before the sign of the imbalance inverts and the retroreflected beam becomes the more intense beam. As is seen in Figure 5.6, for $\chi = 45^o$ and 90^o the expansion of the retroreflected beam is minimal and can be well approximated by the flat imbalance model. In the case of $\chi = 135^o$, however, the significant spreading of the retroreflected beam leads to a widely varying imbalance across the spatial profile, which the flat model fails to account for.

The dynamic model, rather than using a common fixed-sized Gaussian beam, uses measured sizes of the input and retroreflected beams to compute the local intensity of each beam independently as a function of position. From these intensities we directly generate a force map, $F(z, y)$, based on the actual intensity

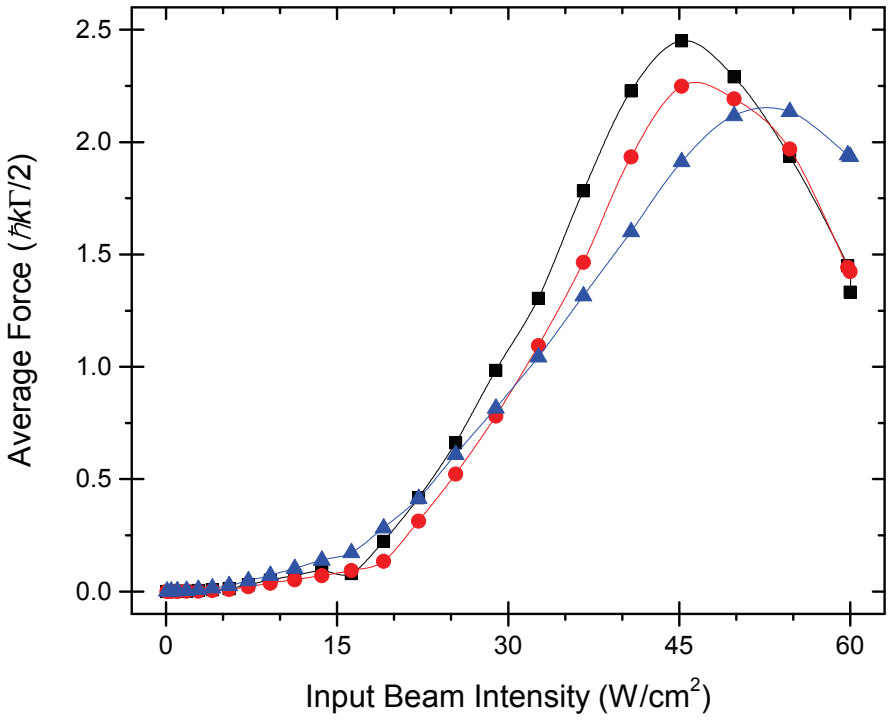

Fig. 5.5: The $F(I)$ profiles for $\chi = 45^o/135^o$ without imbalance (squares), $\chi = 45^o$ with imbalance (circles), and 135^o with imbalance (triangles) are plotted together for the case of their respective flat imbalances. At the optimal intensity, the $\chi = 135^o$ curve shows a much larger reduction in force magnitude due to imbalance than the $\chi = 45^o$ curve, but actually produces a larger, flatter force profile at high intensities. Averaging over the full intensity profile of the BCF beams show that this boost in force at high intensity seems to compensate for the peak force reduction at $\chi = 135^o$.

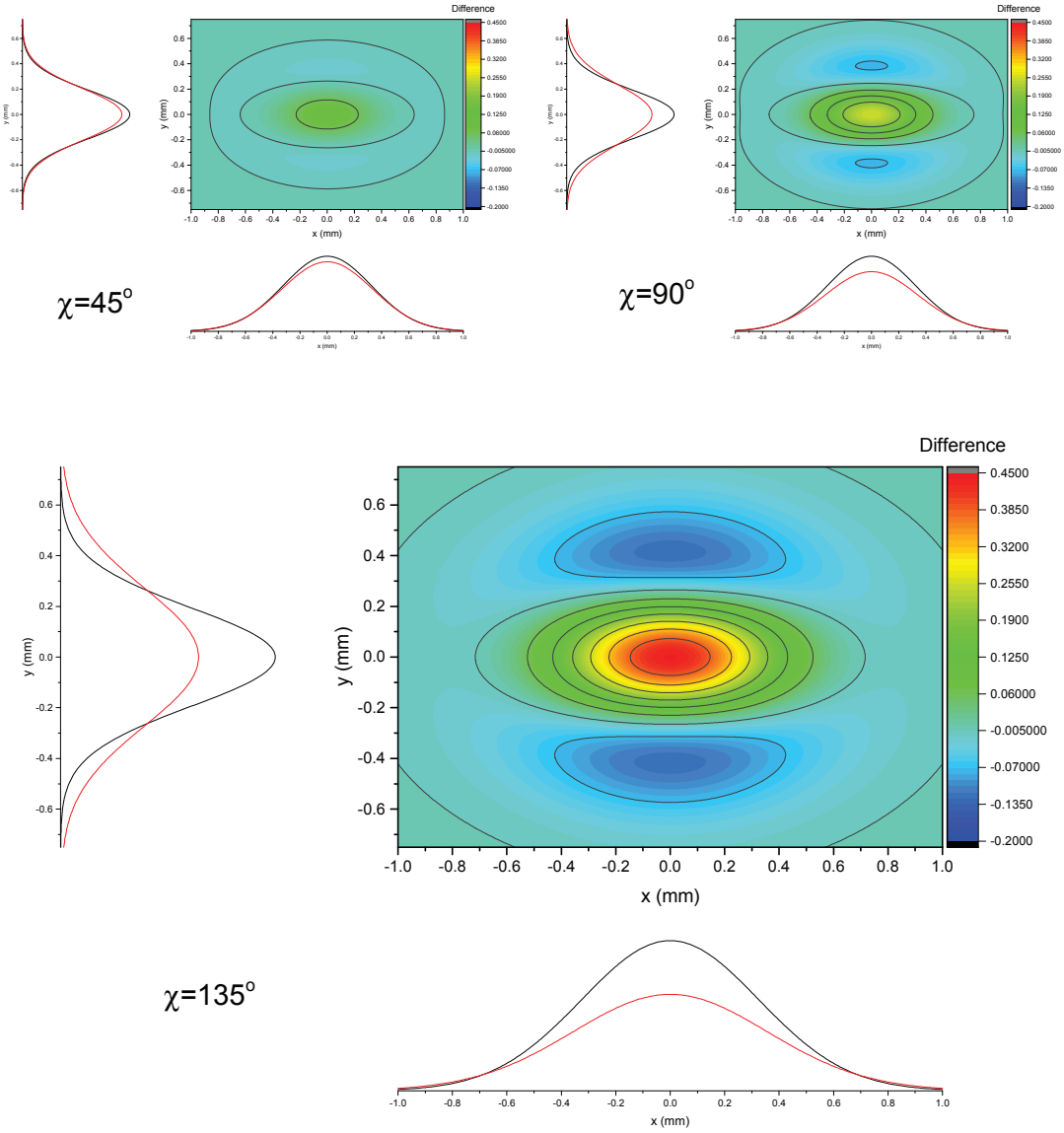

Fig. 5.6: Contour plots showing the difference between the input and retroreflected beams intensities at the center of the interaction region as computed from measured beam dimensions at phases of $\chi = 45^o, 90^o$, and 135^o. All the differences are shown on the same color scale. At left and below are vertical and horizontal slices, respectively, through the center of the input (black) and retroreflected (red) beam profiles. For $\chi = 45^o$ and 90^o, the imbalance is a small perturbation: the beams are very close in size and well approximated by the flat imbalance model. At $\chi = 135^o$ the input and retroreflected beam sizes diverge significantly and the flat model is no longer accurate.

imbalance at each point in space. Using a further modified version of the code taken from [37] (summarized in appendix B), we generate a uniform 20x20 point grid of positions, with corresponding intensities, for the input and retroreflected beams at $\chi = 135^o$. The grid spans one quadrant of the simulations interaction domain and is then tiled to fit the full domain. The deflection simulation is carried out using the directly computed force map, $F(z, y)$; results are found in table 5.1 and plotted in Fig. 5.3 (triangle). The intensive computational time needed to compute the force map—400 force profiles for a given phase in the dynamic model vs. 20 in the flat model—coupled with the apparent accuracy of the flat model for $\chi = 45^o$ and 90^o meant that the dynamic model was only used to compute the deflection at $\chi = 135^o$. The code should be flexible enough to handle any phase if further study becomes warranted.

5.3.2 Experiment vs. Model

In Figure 5.3, we compare the results of the experiment to the results of the simulated experimental models. We see very good agreement for the cases of $\chi = 45^o$ and $\chi = 90^o$, but at $\chi = 135^o$ theory and experiment seem to diverge.

For $\chi = 45^o$, the experimental deflection is consistent not only with the flat imbalance model (as we expected), but also with the ideal model. Within the level of uncertainty of our measurement, the two models are indistinguishable. Implicit in this observation is the fact that the observed shift is also significantly greater than the shift predicted for the radiative force. The deflection from the BCF is $\sim$4.1 times greater than the predicted radiative force deflection when averaged over the full Gaussian intensity profile of the beam. Given that the BCF is so sensitive to intensity, it is likely that this factor could be extended even further

if a more uniformly intense beam was used. In fact, the close agreement of the experiment with the model suggests that the peak force realized by the BCF in our experiment may have been as much as an order of magnitude greater than the saturated radiative force in CaF. Whether or not that is actually the case is difficult to prove definitively with our current apparatus, but in either case, it is clear that the average BCF certainly exceeds the radiative force. With higher detuning and/or a more uniform field, it would be interesting to see how far this enhancement could be extended.

For $\chi = 90^o$ we again note excellent agreement with theory. Since the force is expected to vanish at this phase, however, it does not independently provide a persuasive demonstration of the BCF. It is not conclusive to simply lose the force at this point but when taken in consideration with the deflections demonstrated at $\chi = 45^o$ and 135^o, the vanishing of the force at 90^o does suggest the characteristic periodic behavior of the BCF.

For $\chi = 135^o$, the results become a bit less satisfying. As noted previously for the raw beam profiles (Fig. 5.1), the deflection results show qualitative but not quantitative agreement with theory. Based on our simulations, the flat imbalance model suggests a decrease in deflection magnitude of roughly 13% compared to ideal, and the dynamic model suggests another 18.5% reduction from that—a total reduction of nearly 30% from the ideal deflection. This value is, however, still roughly a factor of 2 higher than the experimental observation—a deviation of $\approx 2.2\sigma$. What can be said about the deflection for $\chi = 135^o$ is that it is: (1) clearly negative and inconsistent with no deflection, and (2) consistent with at least the magnitude of the radiative force. It is highly unlikely that this deflection is actually from a negatively directed radiative force. The input beam is not

adjusted when the phase is shifted, and the presence of the BCF at $\chi = 45^o$ suggests that it was properly aligned for those trials. If any misalignment is introduced by the process of switching phases, it would be in the retroreflected beam, nominally resulting in a $+x$-directed radiative force. Another possible origin for a negatively-directed radiative force is from the non-overlapping regions of the retroreflected beam. Since the retroreflected beam is larger than the input beam, in areas where the two beams do not overlap well the retroreflected intensity could apply a radiative force in the $-x$-direction. However, since we have ruled out misalignment of the beams, when the molecules subsequently enter the overlap region, the $-x$-directed BCF should dominate and only serve to push them further in the $-x$-direction. However, this effect of imbalance is already accounted for in the dynamic model, as we developed it primarily to take into account factors such as these. Whatever the reason for this decrease in force, it is apparently not something that we have considered in any of our models. Further study into the nature of this reduction would be potentially interesting. A more sophisticated retroreflector system, for example, could be employed to ensure a better match with the input beam.

Regardless of how we consider the $\chi = 135^o$ data point, collectively the data strongly suggest the presence of BCF deflection of the CaF molecular beam. The characteristic periodic χ dependence of the deflection, in particular the ability to reverse the direction of the force has been demonstrated. Furthermore, with proper choice of parameters, the average force has been shown to exceed the radiative force by a factor consistent with theoretical models. Even for the case of $\chi = 135^o$ where the deflection is reduced by a factor of $\sim$2 from our modeled behavior, we still observe a deflection in the $-x$-direction with a magnitude at

least that of the radiative force.

5.4 Control Analysis

As described in Sec. 5.1.1, the control data is comprised of a combination of older data and newly acquired data. The older data were collected while the experimental parameters were still being refined, specifically while the BCF beam intensity was being tuned to maximize deflection. The BCF data from these older acquisition trials is invalid because of this, but the control data should not be adversely affected. The radiative force effects considered in the control cases are much less sensitive to the specific intensity of the beams, particularly given that all of the intensities considered during tuning were in a saturated radiative force regime. With the older data properly incorporated, our datasets were expanded from 2 trials at each control condition to 9 trials for the single-frequency control and 13 trials for the no-retroreflector control.

We find that the single-frequency standing-wave data is consistent with no shift, as we'd expect. The roughly equal intensities incident from both the $\pm x$-directions generate a standing wave in the interaction region. If properly aligned, the periodic potential of the standing wave could diffract the molecular beam [74], but without an imposed directional preference, the diffraction would be symmetric. Thus while the presence of the standing wave may cause the molecular beam to expand, it should do so symmetrically and thus produce no net deflection.

For the bichromatic traveling wave condition, i.e. no retroreflector, we find that the data are consistent with the simulated deflection due to a $+x$-directed radiative force. This simulation was computed as the extreme limit of intensity imbalance, i.e. zero retroreflected intensity. The two-frequency beat note traveling

wave can be considered by decomposing it into its Fourier components as $\omega - \delta$ and $\omega + \delta$. Each of these components will act independently on the molecules in the beam, applying a radiative force. Despite being significantly detuned from resonance, the high intensity of the beams should still saturate the radiative force action on the molecular beam.

As mentioned previously, due to time constraints we were only able to take a single round of data at reduced intensity. The peak intensity was reduced by 20% such that the region of the beam formerly at the optimal intensity of 45.2 W/cm^2 would be reduced to ≈36.2 W/cm^2. Based on modeling of our system, this intensity should deliver ≈50% of the peak BCF force. We find that the measured average value of the shift—0.0941 mm—is within $< 1\%$ of the modeled shift value of 0.0934 mm, but the large margin of error on this measurement makes this more a curiosity than a conclusive demonstration.

5.5 Limitations and Shortcomings

As illustrated by the low-intensity control condition, the margin of error on individual measurements proved to be a significant limitation to the experiment. The low signal-to-noise ratio for individual shots necessitates a large amount of data to be averaged in order to draw useful conclusions. Several factors contribute to this, mostly in the form of contributions to the noise levels in the experiment. Several key noise sources were identified from the analysis and are addressed below.

5.5.1 Signal Fluctuations

The largest source of random error in the experiment is due to fluctuations in shot-to-shot molecular flux from our CaF beam source. As a direct consequence of our detection scheme, variations in the beam flux are mapped directly into variations in signal, putting an effective lower limit on the shot-to-shot signal fluctuations. In addition, because of the low number of photons collected in a given shot, the flux fluctuation noise becomes coupled with the fundamental shot noise limit of the system. The net result is that long acquisition times are necessary to generate useful data.

It follows from this averaging requirement that the signal cannot accurately be monitored in real-time. Until the full dataset has been collected and averaged, it is difficult to determine the quality of the data. This leads to further time spent repeating trials, which only serves to limit the parameter space that can be explored.

An attempt was made to track and compensate for these fluctuations by acquiring deflected and undeflected data on alternating shots. This data collection scheme, outlined in Sec. 4.5.4, uses a remotely triggered shutter to alternate between passing and blocking the BCF on alternating shots. This would have allowed us in principle to acquire the deflected and undeflected data nearly simultaneously. By binning the data appropriately, we would be able to isolate and account for data fluctuations on different timescales. Due to low signal levels, however, this attempt was unsuccessful. Since so few photons are collected each shot, fluctuations in signal due to shot noise will dominate the noise spectrum. Because these fluctuations are random they cannot be properly isolated and thus cannot be removed from the signal.

5.5.2 Scattered Light

Further exacerbating the noise problem is the presence of scattered light within the system. The small signal count of our experiment means that the shot noise for even just a few hundred scattered light photons is enough to potentially eclipse our signal. As a result, a great deal of time was spent working to reduce external source of scattered light. Baffles were added internally and externally to physically block light sources from reaching the detector, and while we never achieved order-of-magnitude improvements from any given step, we are able to accumulate enough factors of 2 to make a difference. That being said, the scattered light remains our baseline noise level for the experiment. We eventually were able to get the scattered light counts down to roughly our signal counts, but there is more still that can be done to improve things further (see Sec. 7.3).

Further reductions of the scattered light could also allow for the use of an alternative transition for LIF excitation. If the $A - X$ (0,0) band could be used for detection it would allow for the possibility of cycling the detection transition, thereby increasing the number of photons emitted per CaF molecule. The switch to a cycling transition would increase the photon yield with only very minimal changes to the current apparatus required. Results reported from other groups that use cycling LIF transitions suggest signal increases of an order of magnitude could be possible [31]. However, since the fluorescence signal is at the same wavelength as the excitation laser, spectral filtering is not possible and scattered light must be carefully controlled.

5.5.3 Molecular Beam Collimation

From our analysis of our imaging, we find that the narrow field of view of the detector is roughly commensurate with the width of our molecular beam. Generating a narrower molecular beam in the x-direction would potentially allow for imaging of the complete beam profile, making shifts much easier to identify and quantify. Better collimation in the y-direction would allow the molecular beam to sample a more uniformly intense region of the BCF beams.

There was a proposition during the design phase for the addition of a secondary collimating slit to follow the primary skimmer, but it has never been implemented. While such an addition would be potentially beneficial to the resolution of the experiment, it would have to occur in concert with an increase in the molecular beam flux. The signal is currently low enough that further reduction in the molecular flux would almost certainly cause the signal level to fall below the noise floor. If the molecular flux density were to be increased, either by increasing the total flux or by somehow externally collimating the existing beam, then the addition of a collimating slit would greatly help to improve the experimental resolution.

Chapter 6

Extensions of the BCF: 4CF and Beyond

In conjunction with the BCF deflection experiment, we perform detailed modeling of potential extensions to the BCF. In particular, we consider the effect that additional colors would have on the behavior of the force. The addition of two equal, symmetric components at $\pm 3\delta$ produced a marked increase in force magnitude and velocity width as well as a decrease in average excited-state fraction, as described in [38]. The addition of yet more colors further improves performance, but with diminishing returns, thus making them unrealistic given the additional experimental complexity they would require.

6.1 Numerical Modeling

Our exploration of BCF extensions is based on modeling of different forces in a closed two-level system. The primary reason for using such a simple model is that this modeling was performed before the completion of the CaF molecular beam, while we were still considering experimental applications for our existing metastable helium apparatus. The $2\ ^3P_2 - 2^3S_1$ transition used by Chieda [8, 9] is a nearly closed 2-level system, and multi-level effects need not be considered when modeling it. Using this significantly simplified system also allows for much faster calculations, thereby permitting us to explore a more diverse parameter

space than would be possible for a multi-level treatment. Despite the grossly simplified system, it should also be noted that the two-level model does still bear qualitative resemblance to fully multi-level simulations [36], indicating that the conclusions drawn from atomic treatments of BCF extensions should similarly apply to molecular systems as well.

6.1.1 Optimal Parameter Searching

In tests on the BCF, we note that the parameters Rabi frequency amplitude, Ω_r, and relative BCF electric field phase, χ, are effectively independent and define the properties of the resultant force. For simplicity and speed of computation, we assume a similar independence would carry over for different models. Thus, for each of the field models we test, we perform an extensive search of the (Ω, χ) parameter space. Starting with the Rabi frequency fixed at the ideal BCF value, $\Omega_r = \sqrt{3/2}\delta$, we first scan χ to find both the maximum force (peak and average) as well as the minimum average excited-state fraction (at zero velocity). After optimizing χ, the Rabi frequency is then scanned at the optimized χ to see if further optimization can be achieved.

6.2 Polychromatic Field Models

Our motivation for exploring extensions to BCF is to find a way to generate a force that performs more like the ideal π-pulse model. The spatial/temporal overlap between adjacent BCF pulses means that it inevitably deviates from the idealized isolated pulses of the π-pulse model. In an effort to resolve the overlapping, we considered the effect of adding additional frequencies in order to shape the electric field beats and make them narrower in time. Representations of the

tested fields are shown in Figure 6.1.

6.2.1 Square Wave

The first model we tested was an approximation of a square wave. A pair of symmetric frequencies at the ±3rd harmonic of the principal detuning are added to the BCF field. The 3rd harmonic components have opposite phase and 1/3 the magnitude of the fundamental components. In short, we constructed a 2-term Fourier series approximation of a square wave. We began with a square wave pulse model under the impression that a more uniformly intense π-pulse would produce better force performance. In reality, however, we find that the squared-up pulses actually degraded performance of the force. Under re-optimized conditions, the peak force delivered by the square pulses was reduced by approximately 38% compared to the purely bichromatic case. The average excited-state fraction of the system increased under the square-pulse field as well.

Upon examining the dynamics of the Bloch vector, the reason for the performance degradation becomes apparent. The lower peak amplitude of the beat pulses means that more time is needed in order for the system to integrate a pulse area of π. The extended accumulation means that the system spends a greater amount of its evolution cycle with significant excited-state character. The sharp edges of the pulses also mean that the system has little time to relax between adjacent pulse cycles, reducing the time it spends with low excited-state character. These factors increase the average excited-state fraction of the system which causes a greater fraction of the system to decay spontaneously. More spontaneous decays increase the fraction of the system with an inverted pulse sequence and, as a result, decreases the net force on the system.

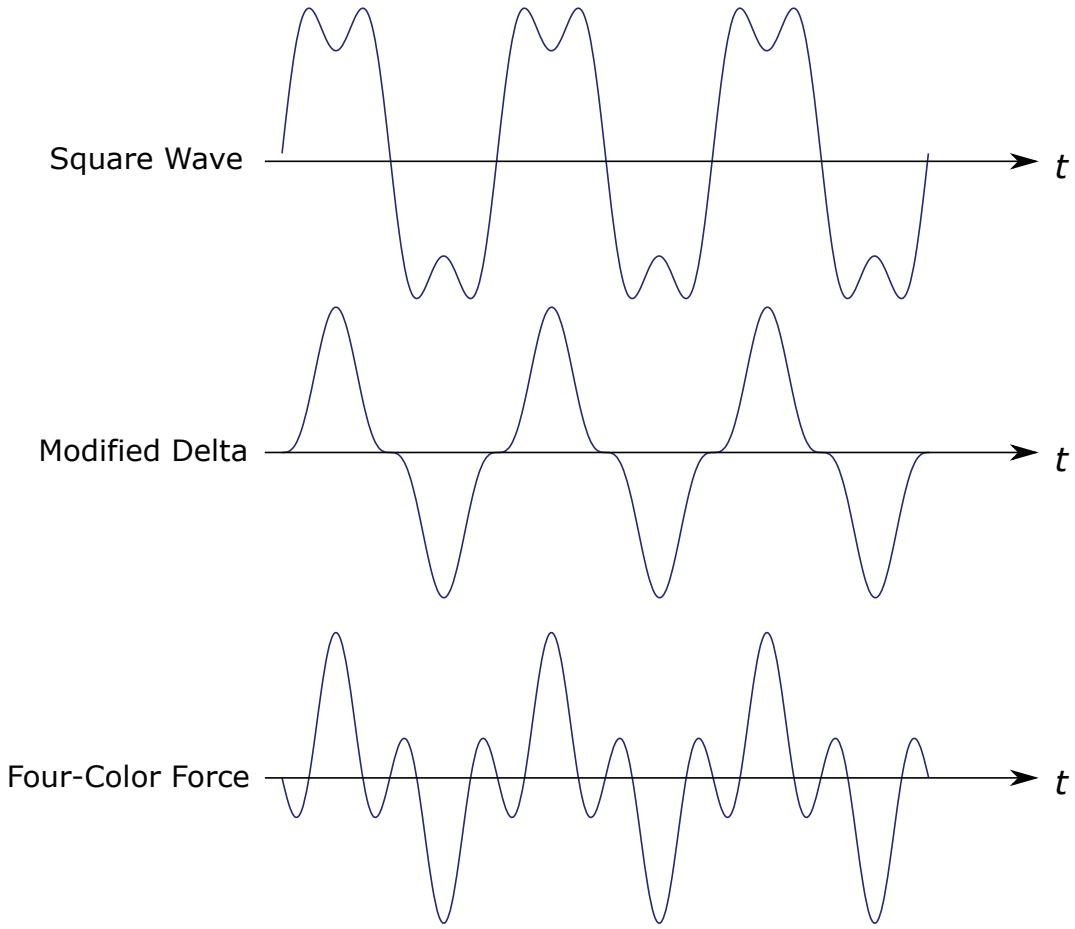

Fig. 6.1: The three polychromatic force field configurations tested are shown. The first, termed "square wave", destructively adds in third harmonic frequencies of the fundamental detuning to produce a more uniform field shape. The second and third are both variations of what is termed a "delta wave" field. These both add constructively (in different magnitudes) the third harmonic to the fundamental detuning field to produce narrower beat note pulses.

6.2.2 Delta Wave

Having no success with the square wave approximation, but being unwilling to give up that quickly, our second test model was to simply reverse the phase of the ±3rd harmonic components: from destructive interference to constructive interference. Even before fully optimizing the system, initial tests of the narrower pulses already outperform the square pulse model. Once fully optimized, the taller, narrower pulses of this model outperform the bichromatic force as well. Examination of the system evolution reveals that the narrower, higher amplitude pulses cause the evolution of the Bloch vector to move very rapidly through the excited state, much faster than the square pulse or bichromatic models. In addition, the narrower pulses could be spaced closer together in time and with less overlap than the bichromatic field–exactly as we hoped they would.

With this insight, we perform a more extensive optimization of the polychromatic parameter space. We separately vary the amplitudes of each frequency component as well as relative phasing between the left- and right-going pulse trains. We find that the system is optimized when the ±1st and ±3rd harmonic detuning components were included in equal proportion with a common Rabi frequency amplitude equal to the (fundamental) detuning. In this configuration, force is no longer maximized at the BCF's relative beat phase of $\chi = 45^o$, but rather at a phase of $\chi = 31^o$. With the force fully optimized, we find the performance of the polychromatic force goes beyond what is achievable with the BCF [38].

The first, most striking, feature is the increased magnitude of the force, as seen in Figure 6.2. The 4-color polychromatic force (4CF) yields a roughly 50% increase in realized force compared to the BCF. To some degree, this should not

come as a surprise, as implicit in the inclusion of additional frequency components is the inclusion of additional laser power. However, the gains in force far outweigh the cost of additional input power. For a given peak force, the lower detuning of the 4CF requires only ∼64% of the total power needed to achieve the same level of force via BCF at a higher detuning. The velocity width of the force increases for the 4CF as well. Compared to a BCF force profile with equivalent fundamental detuning, the 4CF force profile has nearly twice the velocity width. In addition to the surface-level improvements to the force performance, there is another benefit of the 4CF which is less readily apparent. The excited-state fraction of a two-level system under 4CF is decreased from 41% for the BCF down to 24% [38]. Examining the evolution of the Bloch vector reveals the reason for the decrease. As shown in Figure 6.3, the Bloch vector deviates significantly less from the ground state than for BCF (see Fig. 2.3). In addition, since the plotted points represent equally-spaced time intervals, the find that the increased space between points in the 4CF evolution near $w = 1$ suggests that the 4CF also progresses through the excited-state faster than the BCF. This 41% decrease in excited-state fraction relative to the BCF, 41% vs. 24%, results in a value less than half of that for the saturated radiative force. For closed (atomic) systems, this is a useful but non-essential boon. For molecular systems, this decrease in the excited-state fraction more than doubles the average interaction time that can be achieved compared to the radiative force. When coupled with the increased force magnitude and wide capture range, the 4CF presents itself as a nearly ideal tool to help load a molecular trap.

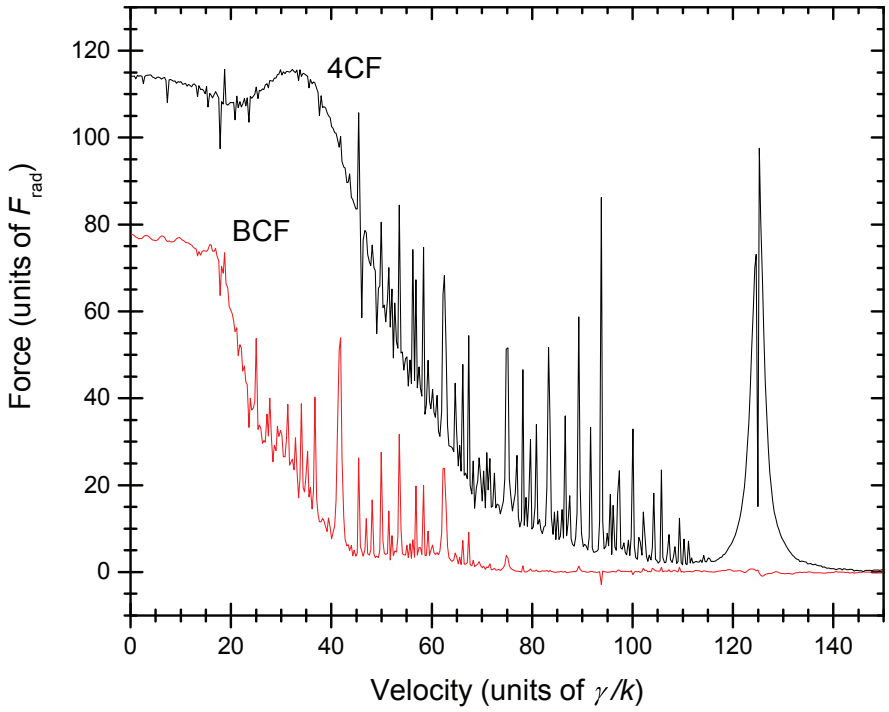

Fig. 6.2: A direct comparison of BCF and 4CF force profiles computed at the same fundamental detuning under their respective ideal conditions. The 4CF produces significantly higher force over a significantly wider velocity range than its BCF counterpart. Generating the optimized 4CF requires ∼33% more laser intensity than the BCF, but to reproduce the same force magnitude via BCF would require more than 40% higher intensity than used in 4CF.

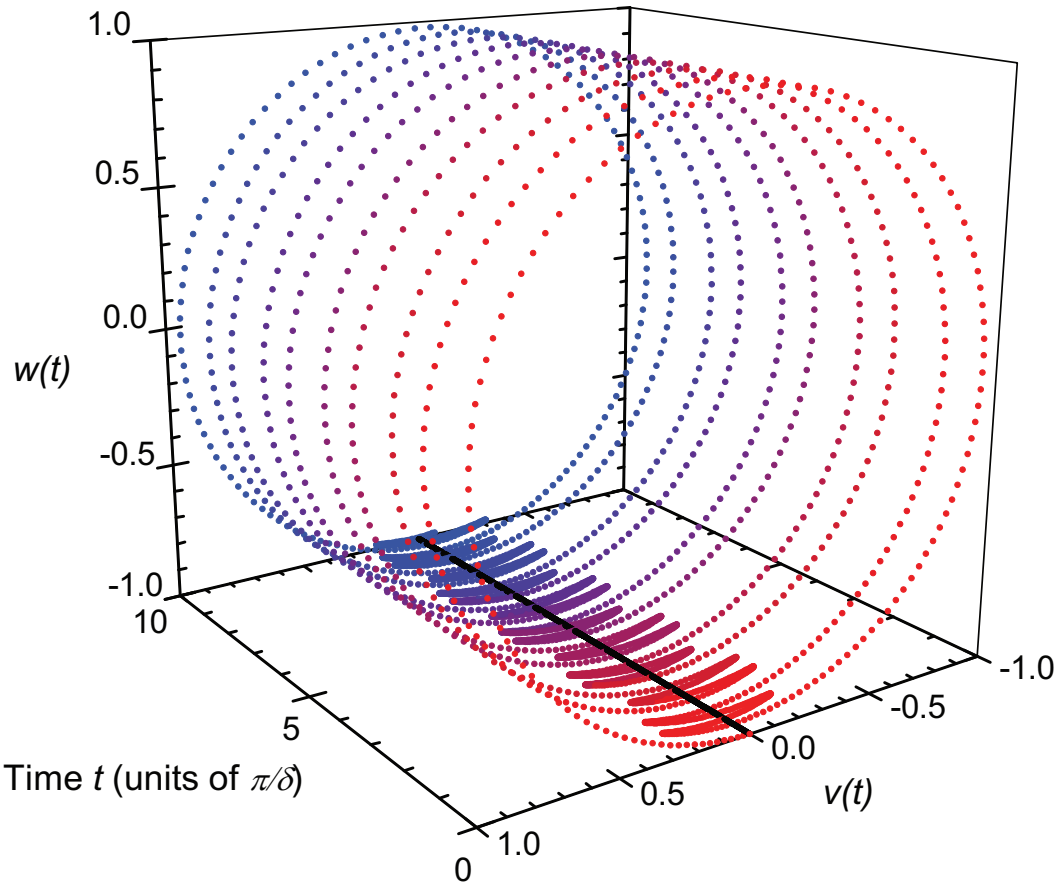

Fig. 6.3: The evolution of the Bloch vector visualized for the case of an optimized 4CF field. The points represent equally-spaced time intervals, thus showing that the Bloch vector spends a significant time near the ground state. This helps to reduce the excited-state fraction even lower than it is for BCF, to an average value of 24%.

6.2.3 Additional Models

After the success of the 4CF, we consider other logical extensions of the concept for the sake of academic curiosity. In particular, we note that, similar to the square wave model, the 4CF is essentially a 2-term Fourier series for a Dirac comb (albeit one with alternating phase). To that end we consider the addition of other harmonics to the series.

We first test the addition of the 2nd harmonic instead of the 3rd. Under these conditions we find the performance of the force to be very poor. Further testing with other even harmonics reveals the same result. We did not explore carefully enough to determine a root cause, but empirically, the addition of even harmonics to the field destroys the performance of the polychromatic forces.

We find, however, that the addition of odd harmonics improves the performance of the force. We tested the effect of additional harmonics: first adding the 5th, then the 7th, etc. to the existing 4CF field. Each time we assume the ideal Rabi frequency condition remains constant and perform a quick optimization of the relative beat phase. We find that as we add more harmonics and the pulses approach delta functions, the force asymptotically approaches $2\hbar k\delta/\pi$ and the phase approaches 0^o. This is to be expected: with zero width, a pair of perfect delta function pulses can be arbitrarily close to each other, thereby reducing the excited-state fraction to zero. Without spontaneous decays to invert the pulse sequencing, the force will instantaneously remove $2\hbar k$ momentum at the pulse frequency, δ/π, i.e. $F = 2\hbar k\delta/\pi$. Despite the obvious benefits of additional colors, it is a case of diminishing returns. The BCF can deliver around half of the theoretical maximum force, and the 4CF delivers $\approx$50% more force than that–bringing the force to roughly 3/4 of the theoretical maximum. In short, despite

the improved performance, we determine that the additional experimental complexity required to implement higher harmonics would be far greater than the benefits that would accrue. In particular, generating short pulses at high peak powers from cw lasers is not very efficient, but it is necessary to exclude even harmonics from the pulse trains in order to retain the beat-note phase oscillation which gives rise to the 4π periodicity (as discussed in Sec. 2.2). The exclusion of even harmonics isn't possible for short-pulse laser systems and thus they require much more careful matching of their pulse train parameters [28–30].

Chapter 7

Conclusion: Next Generation BCF Experiments

Based on the results of the proof-of-concept experiment we performed, the use of the BCF in future experiments appears to be a promising prospect. The design of a second-generation experiment would likely require several changes to the current apparatus, and would provide an excellent opportunity to implement improvements on the existing experimental design. The next logical experimental extension of the current system would be the implementation of a molecular beam slower for our existing supersonic beam source. Undertaking such an experiment would require improvements to the existing laser system, concurrent with a reconfiguration of the BCF optics. The most obviously necessary change is the conversion from transverse to longitudinal directing of the BCF beams. The central frequency of the BCF beams will also need to be Doppler shifted to address the non-zero central velocity of the supersonic beam, and a new adjustment mechanism to control the relative beat note phase will have to be developed. The losses brought on by these additional stages will also likely require more laser power, which could be provided by upgrading to a longer PPLN crystal in the frequency doubler.

The modifications to the BCF optical system will require non-negligible development time, during which the molecular beam will be otherwise idle. This

presents a perfect opportunity to begin implementing measures to improve the supersonic beam source as well. The present experiment was limited primarily by the source performance, and improving this would go a long way towards improving the experiment as a whole. Finding and installing a new pulsed valve is perhaps the most pressing issue with the beam source at the moment. As discussed in chapter 3, the current PZT valve is no longer supported commercially and as such is essentially operating on borrowed time. Several alternative designs are available, most notably the Series 9 valve from Parker which has been used to great effect in other source of similar design. There are also several improvements that could be made to the calcium target rod in order to improve the stability and lifetime of the output flux. Alternatively, the supersonic beam could be exchanged entirely for a cryogenic source such as the one used in [11, 16, 18, 31, 53]. Sources of this type produce slower molecular beams, and often at much higher flux, than their supersonic predecessors.

7.1 CaF Decelerator

The long-term plan of study for the BCF has always included the implementation of a decelerator. The deflection experiment was intended as a stepping stone upon which a decelerator would be constructed. To that end, during the setup of the deflection experiment, many of the components were designed and selected to be either directly compatible with a longitudinal slower, or easily modified to serve that purpose. After completion of the deflection experiment, we can now re-visit that plan and explore the potential of BCF slowing for a supersonic beam.

7.1.1 Feasibility Estimates

In the case of a 45^o beat phase, we are able to realize an average deflection of $\sim$ 0.145 mm. This deflection is consistent with an average force of 7.9x10^{-21} N across the $1/e^2$ diameter of the Gaussian profile of the force beams. Applying these results to the case of a longitudinal slower, and considering a uniform beam acting with the average BCF force, we find that a supersonic beam of CaF would be slowed to rest in $\sim$5.1 μs, covering an interaction length of approximately 2 cm. Importantly, this short distance would minimize density loss due to divergence of the molecular beam. Also, it is short enough that the BCF phase, χ, can be considered constant across the interaction region, greatly simplifying the setup. For a crossing angle of $\sim 1^o$, achieving an interaction length of 2 cm would only require a BCF beam with a $1/e^2$ diameter of $\sim$0.35 mm. Thus we already have sufficient laser power to produce the average intensity we need for efficient BCF slowing. Despite the low excited-state fraction and high Franck-Condon factor for the $B - X$ transition, the extended interaction time over this slowing region would, however, likely require the use of a repump laser to capture population lost to vibrational dark states.

7.1.2 Required Modifications

In order to implement a BCF decelerator, several changes will have to be made to the existing transverse deflection apparatus. By design, the number of modifications to the beam line apparatus should be minimal. The construction of a longitudinal slower was anticipated during the construction of the deflection experiment, and the chamber was designed to be accommodating to either configuration. To wit, the flight tube and detection chamber were chosen to allow for

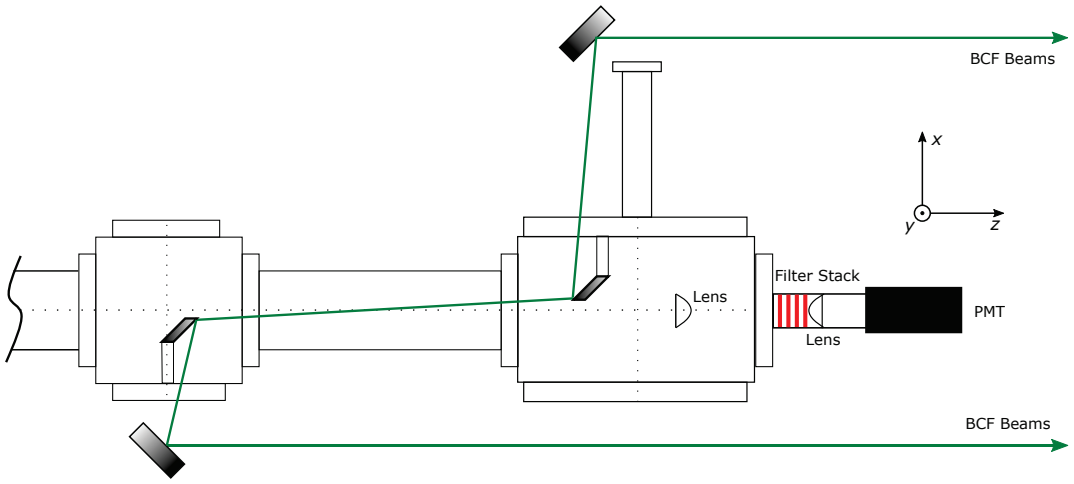

Fig. 7.1: Diagram of the experimental apparatus configured for BCF deceleration. The only major modification that would be necessary is the inclusion of a pair of fixed internal mirrors to point the BCF beam (nearly) colinear with the CaF beam. The experimental chamber was purposely designed to be flexible enough to accommodate slowing as well as deflection.

the passage of a BCF slowing beam with a $\sim 1^o$ crossing angle relative to the CaF beam via a single pair of fixed, in-vacuuo turning mirrors. This configuration is shown in Figure 7.1. The more extensive set of modifications involves the optical setup for BCF generation.

The single most significant change to the optical system is the need for two independent bichromatic beams: one co-propagating with the molecular beam and the other counterpropagating. In the transverse deflection case, the BCF is addressing a population with (nominally) zero-velocity, thereby requiring no inter-beam Doppler shift to address the system. That is no longer the case in a longitudinal system, and a simple retroreflector no longer suffices to generate our counterpropagating beam. This, however, has already been considered. The deflection experiment only makes use of a single retroreflected bichromatic beam,

but with longitudinal slowing in mind, the optical system, as it stands, generates two bichromatic beams already. In addition to the beam used for deflection, the beam used for co-alignment of the frequency components is also a bichromatic beam. During early versions of the optical system, the alignment beam was originally planned as the counterpropagating component beam, but for the sake of simplifying phase adjustment we opted for the retroreflector instead.

In the case of longitudinal slowing, the non-zero velocity of the beam requires the central frequency of the BCF beams to be Doppler shifted to remain resonant. Since the BCF beams need to be counterpropagating, the Doppler shift is mirrored in each beam: the BCF beam counterpropagating with the molecular beam is red-shifted, the copropagating BCF beam is blue-shifted. In order to achieve this mirrored shift, we need to shift each of the two beams independently. For the $B - X$ transition at λ=531 nm, with a mean CaF beam velocity of 415 m/s, we find the required shift in each direction is approximately $kv = 2\pi(782\text{ MHz})$. The simplest way to handle this experimentally is with an AOM driven at the shift frequency. The counterpropagating beam is deflected into the -1st-order, the copropagating beam is deflected into the +1st-order. This is shown conceptually in Figure 7.2.

Switching from a single beam to a pair of beams also brings with it the complication of setting the relative phase between the beat pulse trains. Since the beats are formed when the two beams are generated by the beamsplitter, there is not an easy way to code the phase into their formation in the same way it was done in the He* experiment [9]. Instead, the phase must be set by an asymmetric modulation of one of the beam lines. Since the doubler's output power limits us to modest detunings, an optical delay line likely remains the easiest method of

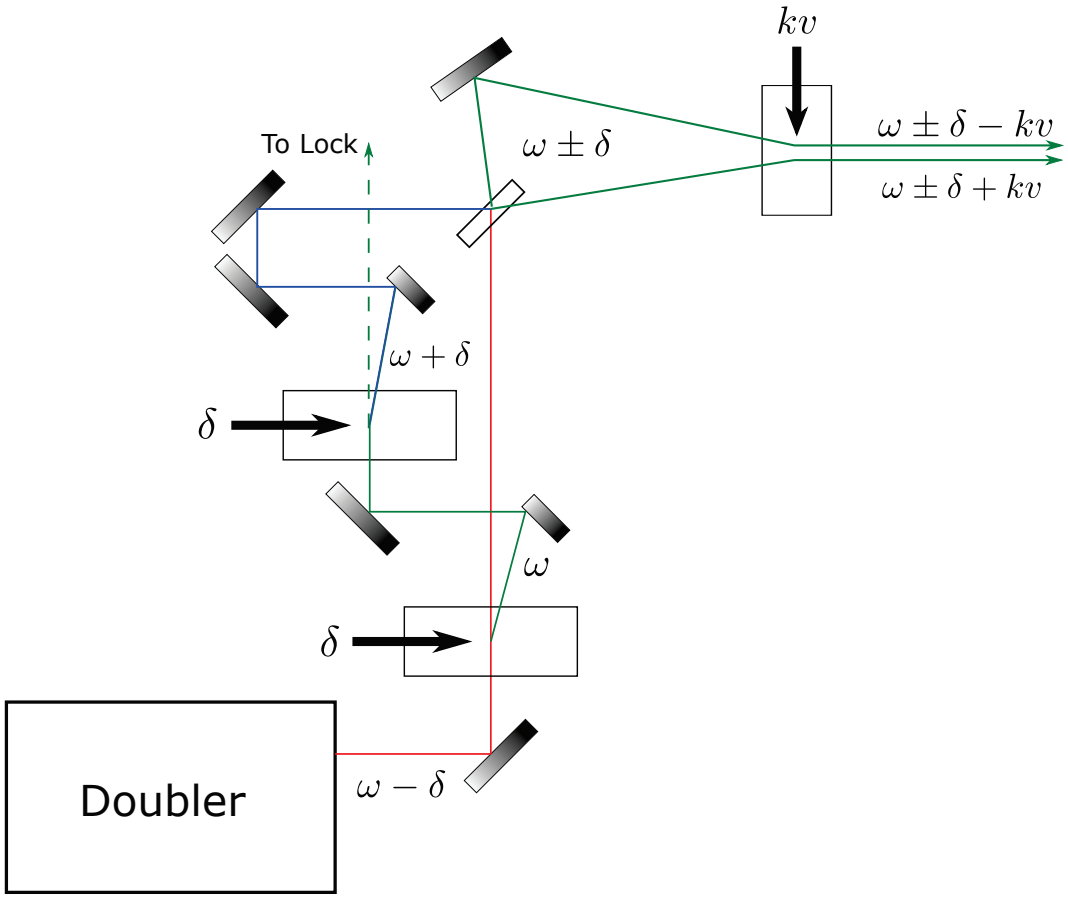

Fig. 7.2: Schematic diagram of the changes needed to the AOM setup to accommodate the Doppler shift needed for BCF slowing. With careful aiming, it should be possible to generate the $\pm kv$ beam components from a single AOM tuned to the shift frequency. Alternatively, two separate AOMs could also be used in a double-passed configuration, driven at half the Doppler offset frequency.

setting the relative beat phase. Even a detuning of $\delta = 100\Gamma$, which would require an intensity of 503 W/cm^2, has a beat wavelength of $\sim$47 cm, i.e. $\sim$1 mm/1^o. Adjustments on this scale are easily achievable by physical delay lines, especially if a micrometer adjustment stage is used.

Alternatively, if the optical system is reorganized to generate beats after Doppler shifting, as in Figure 7.3, it may be worth considering an active beat control mechanism like the one used by [8, 9]. Full details can be found in [9], but in short, the RF frequencies provided to the two AOMs used to generate the $\pm\delta$ beat note frequencies were locked together via a phase-locked loop (PLL) which actively monitored the beat note heterodyne. This method has proven to be effective, but suffered from occasional stability issues. Several improvements and alternatives are presented in [9], and are also worth consideration if major overhauls to the optical system are being considered anyway.

The second most pressing improvement to the optical system is increasing the output power of the doubler. Increasing power would allow the use of larger BCF beams, which, for both transverse deflection and longitudinal slowing, would let us address a larger fraction of the molecular beam and, hopefully, yield larger signals. Increasing power would also allow us to explore a larger region of the detuning parameter space. Since the required intensity scales as the detuning squared, the doubler's current output power and the present beam sizes limit us to the single detuning of $\delta = 30\Gamma$ that we used for deflection. The solution to this issue is another fairly simple one: buy a longer doubling crystal. The 1 cm crystal that is currently installed was intended as a starting point. Once we had the doubler operating well, we had planned to upgrade to a longer crystal, but time and financial issues made that impractical for the deflection experiment.

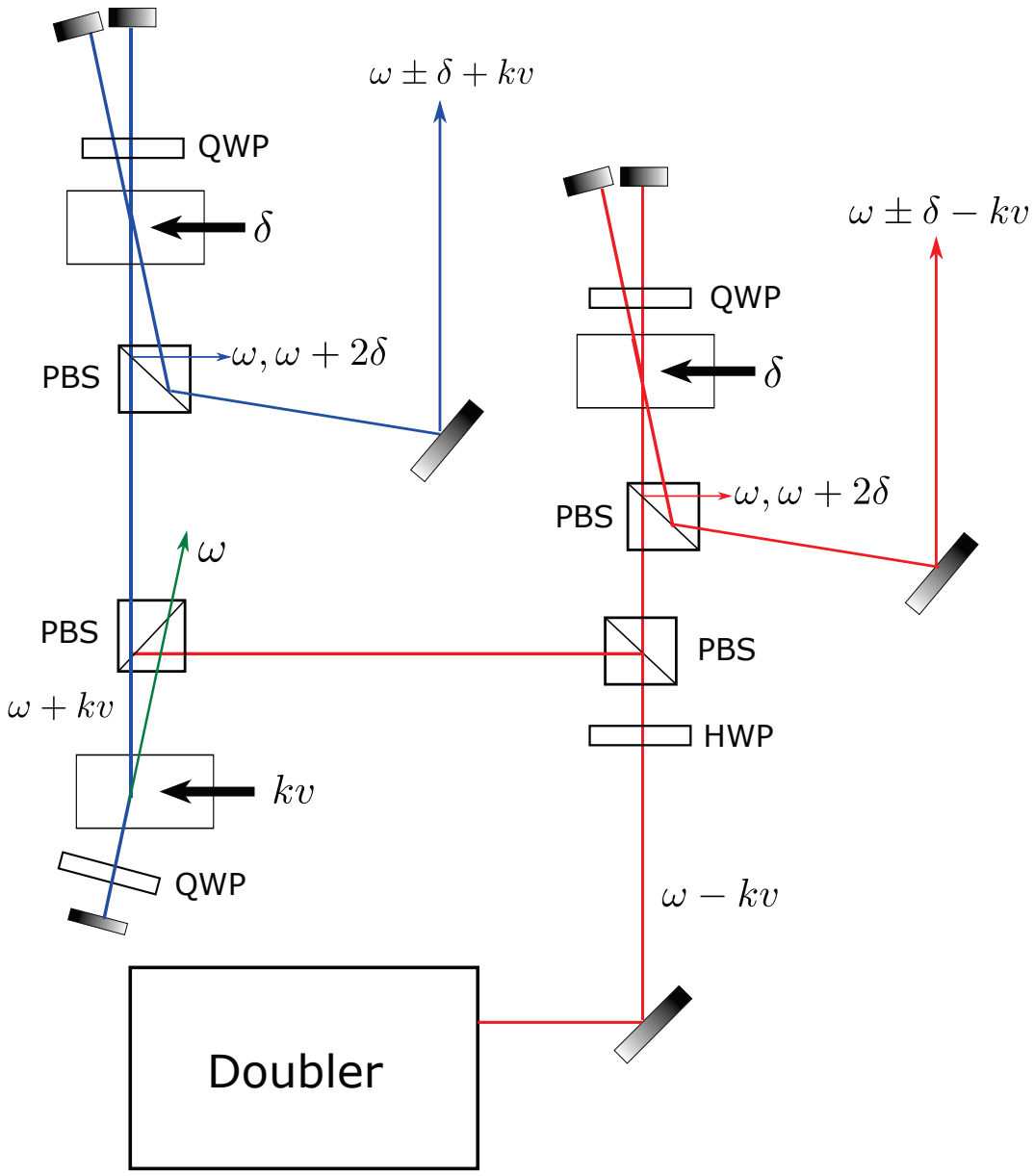

Fig. 7.3: If the optical chain is reorganized to produce the $\pm kv$ Doppler shifts first, then the BCF phase can be actively controlled (as was done in [9]). By monitoring the residual $\omega, \omega + 2\delta$ beams, the heterodyne signal between them can be monitored and used to actively set the RF phase going to the beat-note AOMs. Using a double-passed AOM for $+kv$ generation has the advantage of producing a residual beam at ω which can be used for locking.

According to the manufacturer, when properly installed and aligned, doubled output power should scale (roughly) linearly with crystal length. With our crystal length of 1 cm and an input power of 10 W, we are able to regularly achieve outputs of $\geq$1.3 W at 531 nm, i.e. a conversion factor of $\sim$1.25%/W·cm. While not quite up to the 1.5%/W·cm reported in the manufacturer's application notes (3 W of 531 nm light with a 2 cm crystal at 10 W input), it does suggest that switching to a longer crystal could potentially yield powers up to 5 W for the case of a 4 cm crystal.

7.2 Source Improvements

The part of the experiment that consumed the most development time was maximizing the flux of the molecular beam source. Though we eventually reached an acceptable flux to begin experiments, generating enough molecules to produce a reliable signal at a resolvable signal-to-noise ratio was the primary factor limiting the resolution of the experiment and limiting the number of parameter sets we were able to try. Due to this limitation, before any further experiments are performed, it would be highly beneficial to spend more time working to improve the performance of the CaF beam source. The three factors which are most likely to improve flux magnitude and consistency are: a new pulsed valve, improvements to the target rod rotation mechanism, and improvements to the target rod/valve positioning mechanisms. A more ambitious upgrade would be to switch to a cryogenically cooled beam [31, 53] which would provide increased brightness and a lower average beam velocity.

7.2.1 Pulsed Valve

Of the potential improvements that could be made to the molecular beam source, the change to a different pulsed valve mechanism is perhaps the most pressing. As has been mentioned previously, the valve currently installed in the chamber is an old Lasertechnix PZT pulsed valve which is no longer supported by the manufacturer. Since it is no longer supported, if/when the actuator stops working properly, the valve becomes useless. In order to prevent that from happening at an inopportune time, it would be best to replace the valve as soon as possible.

The most obvious replacement for our valve is a Series 9 pulsed valve from Parker. These valves have been used for a variety of different pulsed gas applications, including in the molecular beam source used by the Field group at MIT (upon whose source ours was based) [49–52]. Series 9 valves use a solenoid-based mechanism rather than a PZT actuator, making them more reliable and easier to repair. Series 9 valves are also in active production, are available in a variety of configurations, and are supported by the manufacturer in the event that more complicated repairs or spare parts are needed. The convenience of the Series 9 does come with its own complications, however. The trade-off for the reliability of the solenoid mechanism is speed. Solenoid valves typically require pulses on the order of 100 μs to fully open, but given that our pulse duration is on this order anyway, this should not be a major concern. In addition, the commercial controllers for Parker pulsed valves, the Iota One, is expensive and famously unreliable. Designs exist for a home-made controller that would work in the Iota One's stead, but this would require time to build and test before operating. The form-factor of the Series 9 also differs from that of our PZT valve, meaning there

would be further down-time required to design and build a mount before it could be installed in the vacuum chamber.

Another option is a relatively new design from Amsterdam Piezo Valve. The eponymous Amsterdam Piezo Valve (APV) is a spiritual successor to our PZT valve, operating via a cantilever PZT actuator. It claims to be able to produce high-flux pulses as short as 20 μs at a repetition rate of up to 5 kHz, and comes in a variety of nozzle configurations. No pricing information is currently available, but the price for this level of performance is almost certainly higher than that of the Series 9 valve. Though not strictly necessary for our molecular beam, an APV would certainly be worth considering as a replacement if it could be repurposed for future projects.

7.2.2 Calcium Target Rod Mount

During optimization of the molecular beam flux, the position and orientation of the calcium target rod was found to have a large effect on the net molecular flux. In order to improve the flux magnitude and reliability, several changes should be made to the target rod mechanism. The simplest change that should be made is to improve the reliability of the motor switching circuit.

On several occasions, the rod motor was found to be malfunctioning due to an error in the switching mechanism. In particular, the flip-flop in charge of switching the motor direction was found to be operating incorrectly. I suspect the root cause of the unreliability is a poorly laid out circuit board. In its current configuration, it is possible that back EMF from the relay switching and/or the motor coils could cause the common ground plane to float high enough (if momentarily) to force the directional flip-flop into a bi-stable or otherwise inoperable

state. Re-wiring the circuit with an improved layout, carefully isolating the logic components from the power-driving components, would likely go a long way to improving the performance of the switching mechanism. In addition, switching from a physical relay switching mechanism to a solid-state H-bridge would likely reduce transient switching spikes in the circuit, thereby helping to further alleviate interference between circuit sub-components. As a final change, while the circuit is being re-wired anyway, it would be highly advantageous to include a manual switching over-ride to the circuit, just in case future errors do still arise.

Ensuring even wear on the target rod is important to source reliability and, at the same time, it also helps improve the lifetime of the target. The drive on which the target rod rotates is a length of 1/4"-20 threaded rod. While the threaded rod does translate the target from end to end, it does not do so particularly efficiently. Through a combination of thread pitch and ablation laser spot size, only $\sim$50% of the rod's active length is actually ablated. The ablation laser wore a deep track into the rod, but left a bare area between adjacent valleys. Switching to a finer-pitch screw would likely alleviate this issue and allow for more even wear of the calcium target rod. Based on what was observed at 20 threads-per-inch, a pitch of at least 40 threads-per-inch should suffice. Such a change should be a more-or-less trivial matter of swapping out one rod/mount pair for another.

Despite the importance of the position of the target rod relative to the pulsed valve, the current apparatus only has provisions for very coarse adjustments to these distances. Further improvements to the molecular flux will likely require a finer and more repeatable way of adjusting the position of the target rod. Thanks to the extended length of the rod, the vertical position of the target relative to the

valve orifice is more-or-less trivial, but the transverse and axial dimensions remain critical adjustments that should be improved. In order to accommodate these adjustment parameters while still providing a stable mounting, it makes sense to combine all of the adjustments into a common mount incorporating both the target rod positioning mechanics and the pulsed valve. An example schematic is shown in Figure 7.4. The assembly can then be aligned by centering the pulsed valve on the molecular beam axis, and the rod adjusted independently without changing the alignment of the beam. The rod adjustments should be repeatable, but do not necessarily need to be either precise or indexed–a simple set screw adjustment should be more than enough to optimize the beam flux. The Field group has noted a "sweet spot" for the ablation spot in their apparatus of ∼1-3 mm from the beam axis transversely, and as close to the valve orifice as possible axially [52]. We had trouble reproducing these spacings, but found that moving the target rod closer to the valve orifice increased the observed CaF flux. The logical extension of this is to provide sufficient adjustment range to go from fully blocking the valve orifice to ∼5 mm away in both the axial and transverse dimensions.

7.2.3 Collimation

Provided that these measures do in fact increase the flux of the molecular beam, the next improvement is, oddly enough, to attenuate the beam: trading off signal for resolution. In addition to struggling with absolute signal-to-noise ratio, we also ran into issues with the spatial resolution of our detection optics. This arose primarily from the fact that the size of our molecular beam is comparable to the size of our detector's field of view. The simple solution is the addition of a secondary aperture further down-stream from the primary skimmer. Since it

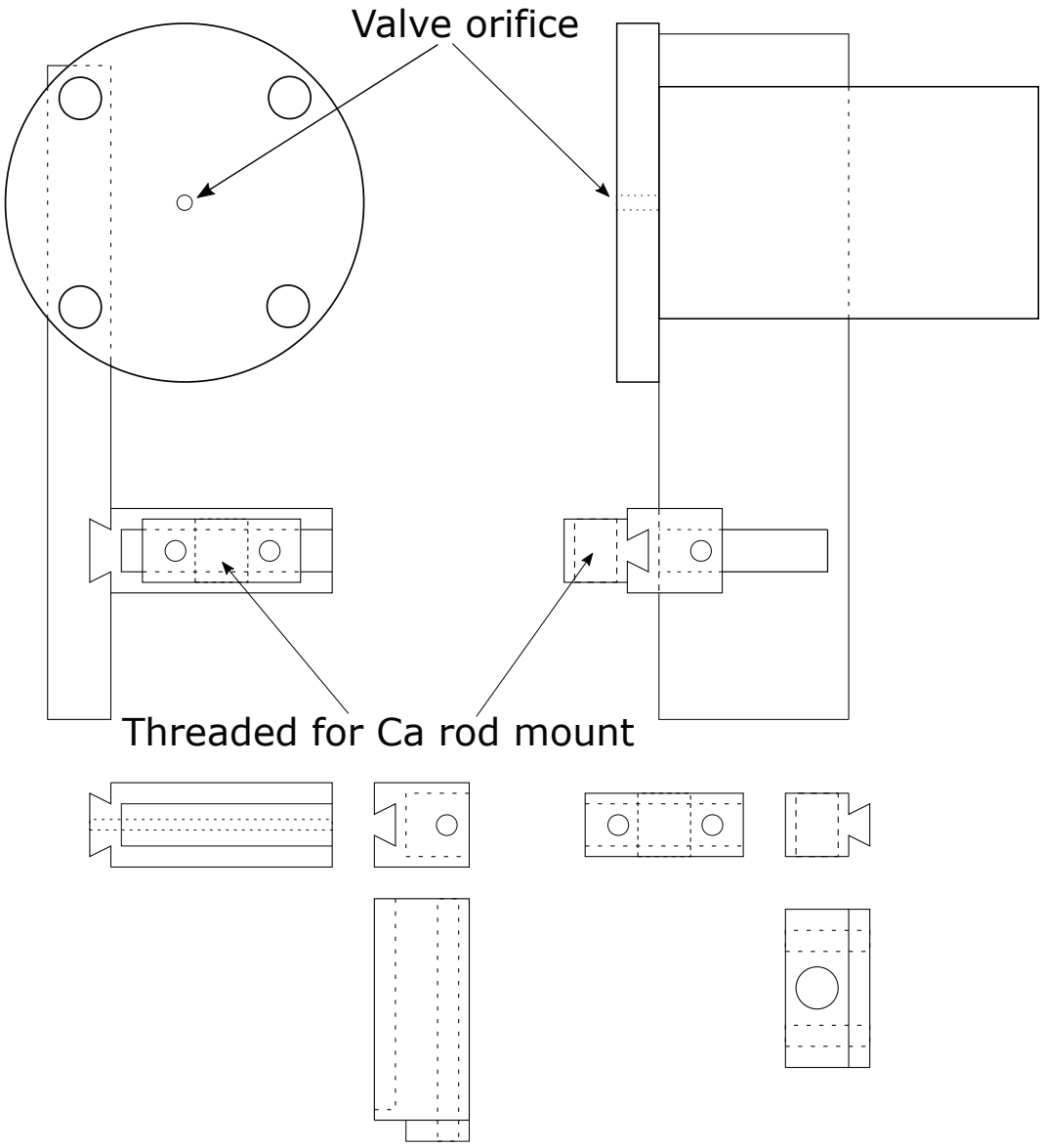

Fig. 7.4: A possible alternative to the current calcium rod mounting hardware (front view and side view). A pair of dovetails provide the 2-axis adjustments needed to properly position the Ca rod relative to the valve orifice. Set screws can be used to clamp the sliding mechanism to prevent slipping, and direct measurement of position relative to the mount itself provides repeatability.

would be in a low-pressure region, theres no need to have anything as sharp or precisely defined as an actual skimmer–a simple slit or orifice should suffice. More important is the placement, orientation, and width of the aperture. The aperture needs to be narrow enough to generate well-defined beam edges at the detector. A slit with a width on the order of 0.25 mm should produce a detected beam size on the order of 2-3 mm full-width at half maximum, which would be ideal. The aperture must also be very carefully aligned to the molecular beam axis, and placed before the BCF acts on the beam. The logical placement is thus in the entry of the interaction chamber. The Kimball Physics chamber is already fitted with internal mounting grooves which should provide a convenient attachment point for a collimating slit, though centering it will still require care.

7.3 Scattered Light Reduction

In tandem with increases to the signal, there are further efforts that can be taken to reduce the dominant noise source in the experiment: scattered light from the detection beam. Externally, switching from a normal-incidence input window to a Brewster window should help reduce the amount of scatter that makes it into the chamber in the first place. A previous generation of detection beam optics required a planar input window, but since that constraint has been lifted it should be possible to incorporate a Brewster window on the input flange. Care must still be taken to leave sufficient room for the existing cylindrical telescope, however.

Inside the chamber, there are further steps that can be taken to prevent scattered light from making it to the detector. Despite the many beneficial features of Kimball Physics, they have the specific flaw (in this instance) of having a highly polished interior. Some crude painted baffles were added to help cut down

on scattered light, but there is still room for improvement. Replacing the current painted baffles with more efficient absorbers–Acktar metal velvet or the copper oxide dendrite materials developed at Yale [75]–would help to reduce the scattered light reaching the detector. Adding further baffling to the interior chamber walls would likely improve things further, however care must be taken to avoid overloading the vacuum pumps with outgassing components.

7.4 Enhanced Detection Schemes

Aside from increasing the molecular flux in the beam, another strategy for increasing measured signal size would be to change the method of detection. As described in chapter 3, our current detection scheme relies on optically pumping our population from the X, v=0 to the X, v=1 vibrational state. Since the decay transition is so much stronger than the excitation, each molecule only emits one photon, thereby limiting our signal. One way to avoid this limitation would be to switch to a cycling transition. If scattered light could be reduced sufficiently, simultaneous excitation and detection on the $A - X$ (0,0) band would allow for cycling, yielding multiple photons per molecule. Care must of course still be taken in choosing the particular rotational transition, however, otherwise optical pumping into dark rotational or hyperfine states will once again limit achievable signals. When implemented carefully, cycling schemes used by other groups have yielded order of magnitude increases in signal compared to non-cycling transitions [31].

An alternative approach would be to increase the detection efficiency. Rather than increasing the number of signal counts (photons) generated per molecule, increasing the number of existing counts that are collected would also serve to

increase the signal. One way to increase detection efficiency would be to change from LIF to charged particle collection. If the molecules could be ionized, the overall signal would still be limited to a single count per molecule, but the ions can be collected much more efficiently than photons and with no scattered light background to worry about. How exactly the molecules would be ionized is still something that would need to be investigated. The ionization energy of CaF is approximately 5.8 eV [76], requiring a deep-UV photon to ionize directly. A more practical method would be resonance-enhanced multiphoton ionization (REMPI) or some other multiphoton process, but the feasibility of these methods has not yet been investigated.

Appendix A

Circuit Diagrams

Many of the instruments used during the course of the experiment were designed, tested, and built in-house. Most of the designs are based on a handful of microcontroller-based motherboards with customizable daughter boards which can be added to fit particular applications. Most notable of these homemade boards were:

1. Temperature controller board:

   Used for temperature stabilization of the DBR diode laser and PPLN doubling crystal. Can be modified to function as a PZT driver by swapping the output stage opamps for a higher-voltage model (fitted to an adapter board).

2. Lock-in amplifier/laser locking board:

   Used for acquiring SAS signals and locking of the A-X dye laser transition and B-X BCF laser transitions in I2.

3. Current driver board:

   Used to drive the DBR oscillator. Based on the design of Durfee, et. al.

4. Diode laser driver interface board:

Universal interface card, originally designed to control a commercial Wavelength-7500 diode current driver. Used to interface between the current driver and Android tablet control program.

5. RF synthesizer board:

   Used to generate the RF driving signal to AOMs

6. RF amplifier board:

   4W RF amplifier used to drive AOMs

7. General purpose lab interface board:

   Base circuit used for several applications. Often used as a precision adjustable voltage control unit.

8. General-purpose photodiode:

   Basic transimpedance circuit based around the AD8606 opamp and originally intended for use with FDS100 (or similar) photodiodes. Circumventing the photodiode allows it to be used as a general purpose transimpedance amplifier.

Documentation for many of these circuits (among others) exist on Prof. Edward Eylers microcontroller electronics webpage (http://www.phys.uconn.edu/ eyler/microcontrollers/) and/or his published microcontroller papers in RSI [77, 78]. The diagrams for the above circuits are included below (in the order presented above).

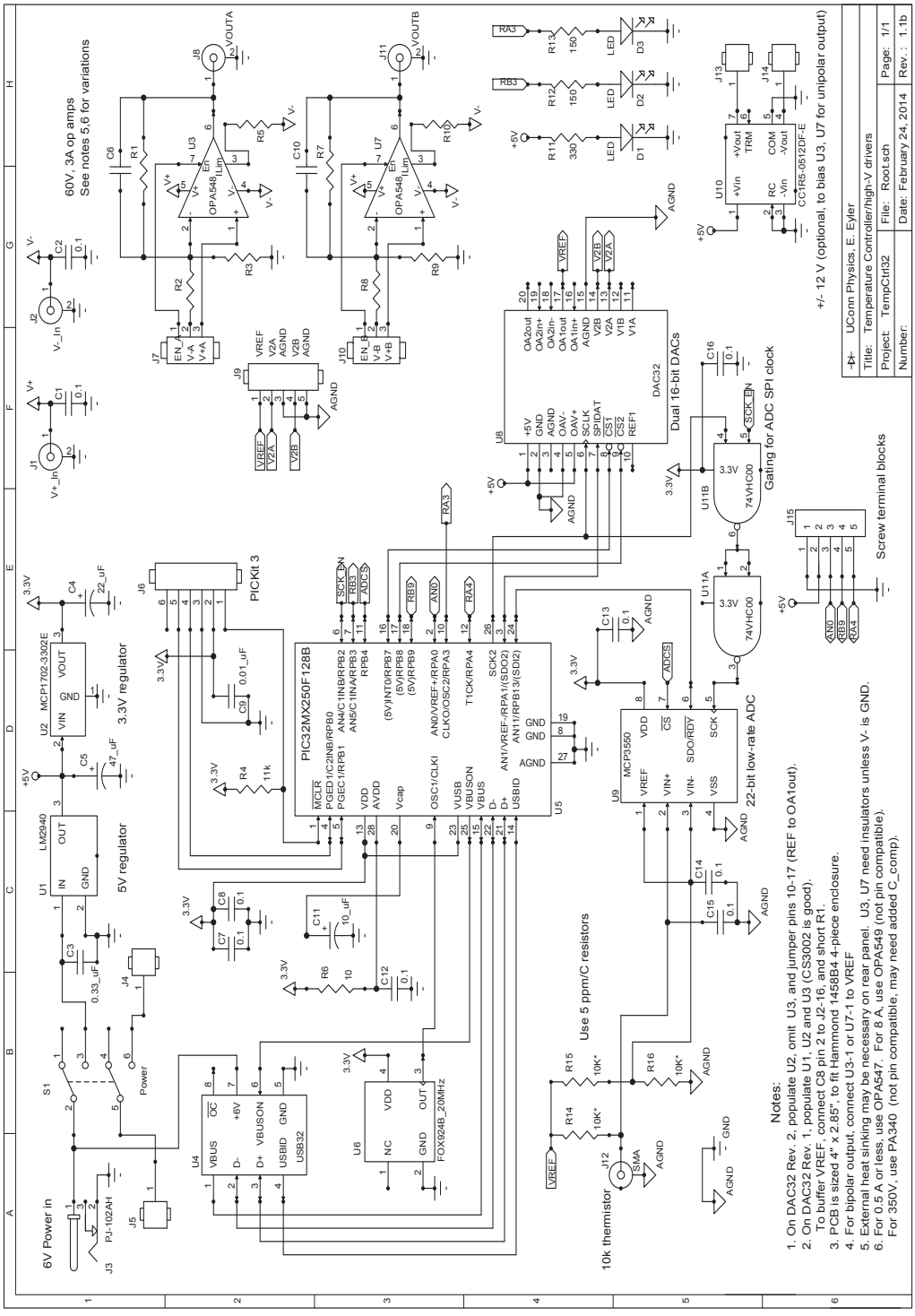
6V Power in
5V regulator
3.3V regulator
PICKit 3
60V, 3A op amps
See notes 5,6 for variations
Dual 16-bit DACs
Gating for ADC SPI clock
22-bit low-rate ADC
Use 5 ppm/C resistors
10k thermistor
+/- 12 V (optional, to bias U3, U7 for unipolar output)
Screw terminal blocks
Notes:
1. On DAC32 Rev. 2, populate U2, omit U3, and jumper pins 10-17 (REF to OA1out).
2. On DAC32 Rev. 1, populate U1, U2 and U3 (CS3002 is good).
To buffer VREF, connect C8 pin 2 to J2-16, and short R1
3. PCB is sized 4" x 2.85", to fit Hammond 1458B4 4-piece enclosure.
4. For bipolar output, connect U3-1 or U7-1 to VREF
5. External heat sinking may be necessary on rear panel. U3, U7 need insulators unless V- is GND.
6. For 0.5 A or less, use OPA549 (not pin compatible).
For 350V, use PA340 (not pin compatible, may need added C_comp).
UConn Physics, E. Eyler
Title: Temperature Controller/high-V drivers
Project: TempCtrl32
File: Root.sch
Page: 1/1
Number:
Date: February 24, 2014
Rev.: 1.1b

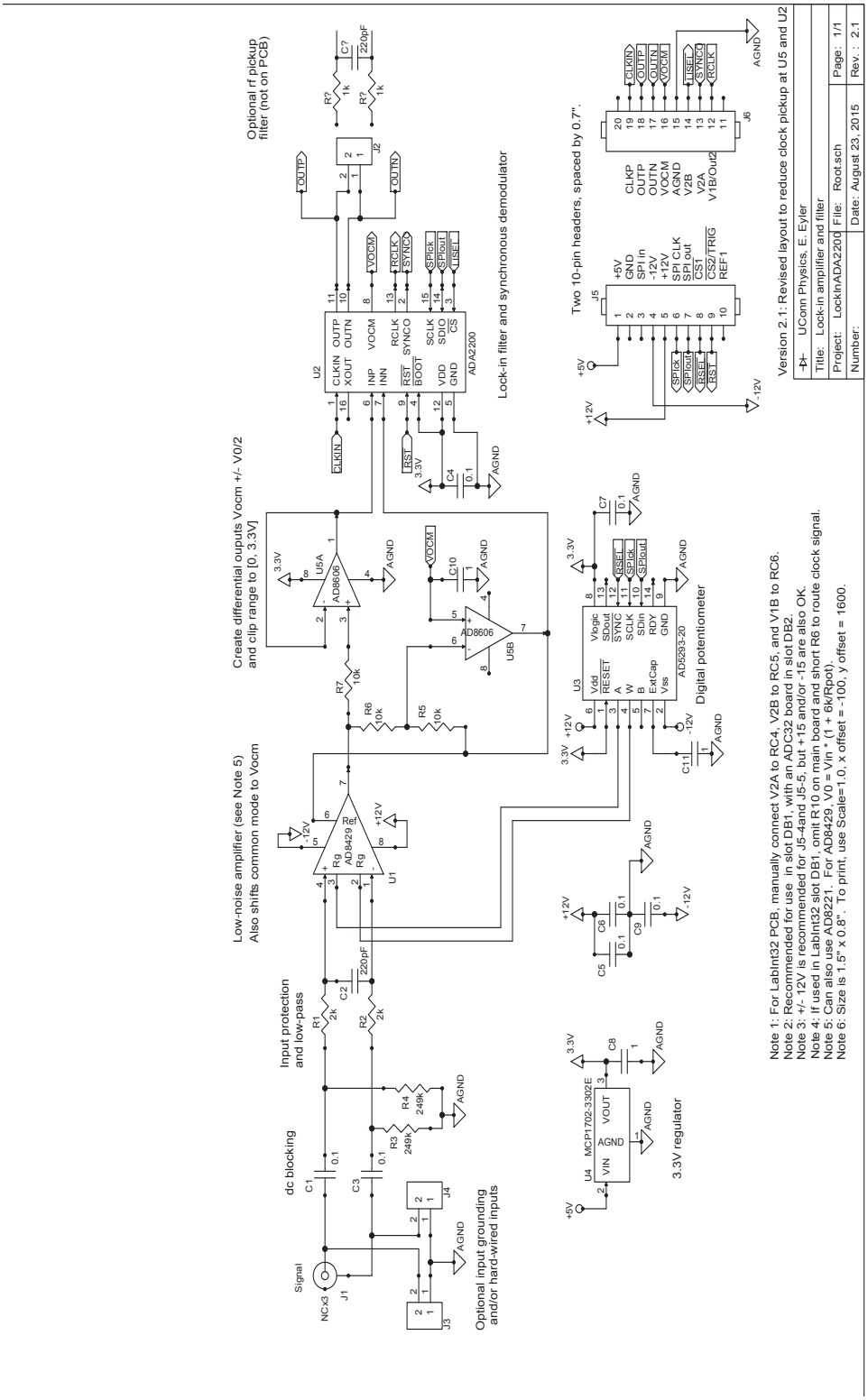
Low-noise amplifier (see Note 5)
Also shifts common mode to Vocm
Create differential ouputs Vocm +/- V0/2
and clip range to [0, 3.3V]
Optional rf pickup
filter (not on PCB)
Input protection
and low-pass
dc blocking
Optional input grounding
and/or hard-wired inputs
3.3V regulator
Lock-in filter and synchronous demodulator
Two 10-pin headers, spaced by 0.7".
Digital potentiometer
Signal
AD8429
AD8606
ADA2200
AD5293-20
MCP1702-3302E
Note 1: For LabInt32 PCB, manually connect V2A to RC4, V2B to RC5, and V1B to RC6.
Note 2: Recommended for use in slot DB1, with an ADC32 board in slot DB2.
Note 3: +/- 12V is recommended for J5-4and J5-5, but +15 and/or -15 are also OK.
Note 4: If used in LabInt32 slot DB1, omit R10 on main board and short R6 to route clock signal.
Note 5: Can also use AD8221. For AD8429, V0 = Vin * (1 + 6k/Rpot).
Note 6: Size is 1.5" x 0.8". To print, use Scale=1.0, x offset = -100, y offset = 1600.
Version 2.1: Revised layout to reduce clock pickup at U5 and U2
UConn Physics, E. Eyler
Title: Lock-in amplifier and filter
Project: LockInADA2200 File: Root.sch
Page: 1/1
Number:
Date: August 23, 2015
Rev.: 2.1

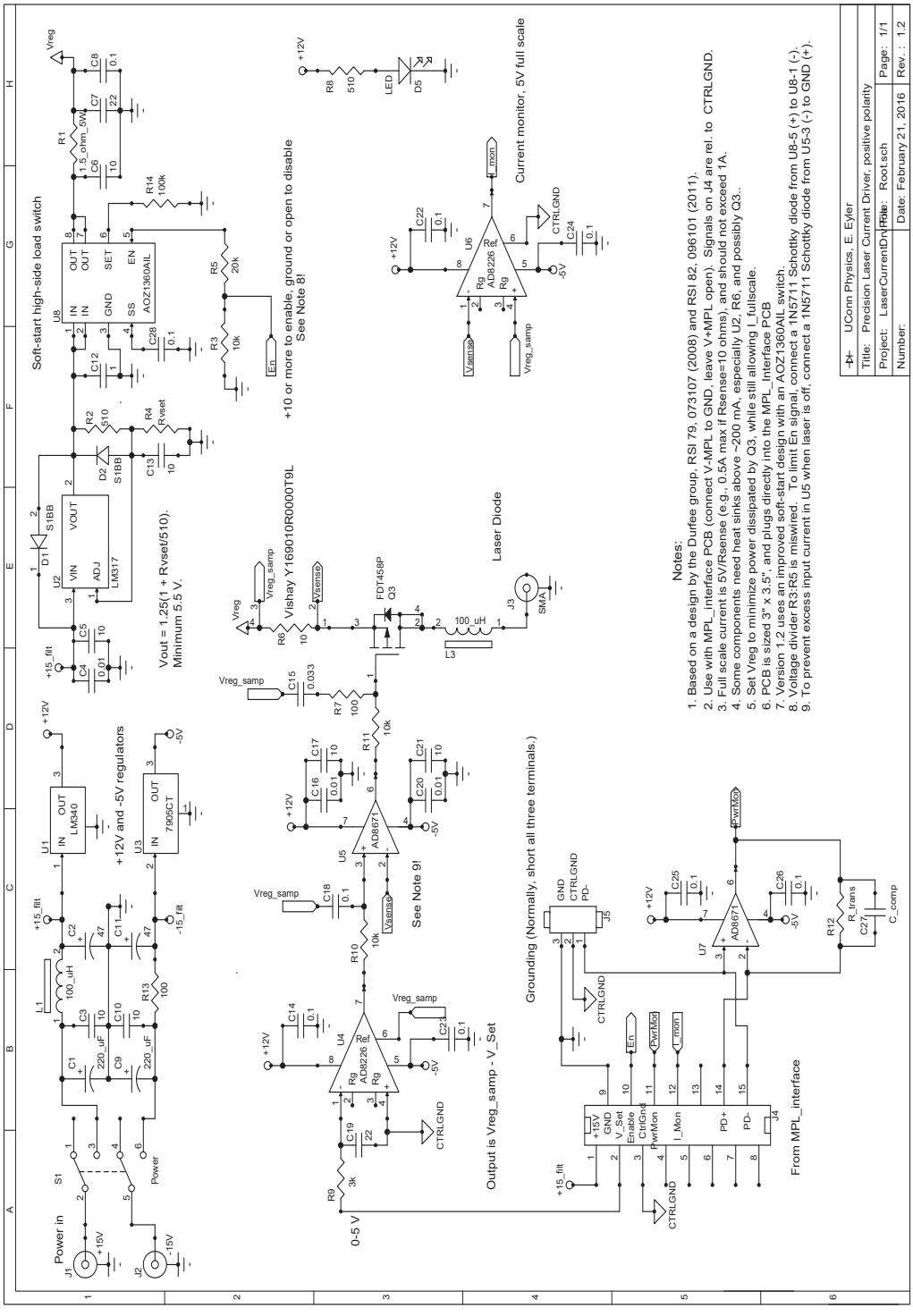
Soft-start high-side load switch
Vout = 1.25(1 + Rvset/510).
Minimum 5.5 V.
+10 or more to enable, ground or open to disable
See Note 8!
Vishay Y169010R0000T9L
Laser Diode
Current monitor, 5V full scale
+12V and -5V regulators
Power in
Power
From MPL_interface
0-5 V
Output is Vreg_samp - V_Set
See Note 9!
Grounding (Normally, short all three terminals.)
Notes:
1. Based on a design by the Durfee group, RSI 79, 073107 (2008) and RSI 82, 096101 (2011).
2. Use with MPL_interface PCB (connect V-MPL to GND, leave V+MPL open). Signals on J4 are rel. to CTRLGND.
3. Full scale current is 5V/Rsense (e.g., 0.5A max if Rsense=10 ohms), and should not exceed 1A.
4. Some components need heat sinks above ~200 mA, especially U2, R6, and possibly Q3..
5. Set Vreg to minimize power dissipated by Q3, while still allowing I_fullscale.
6. PCB is sized 3" x 3.5", and plugs directly into the MPL_Interface PCB
7. Version 1.2 uses an improved soft-start design with an AOZ1360AIL switch.
8. Voltage divider R3:R5 is miswired. To limit En signal, connect a 1N5711 Schottky diode from U8-5 (+) to U8-1 (-).
9. To prevent excess input current in U5 when laser is off, connect a 1N5711 Schottky diode from U5-3 (-) to GND (+).
UConn Physics, E. Eyler
Title: Precision Laser Current Driver, positive polarity
Project: LaserCurrentDrv
File: Root.sch
Page: 1/1
Number:
Date: February 21, 2016
Rev. : 1.2

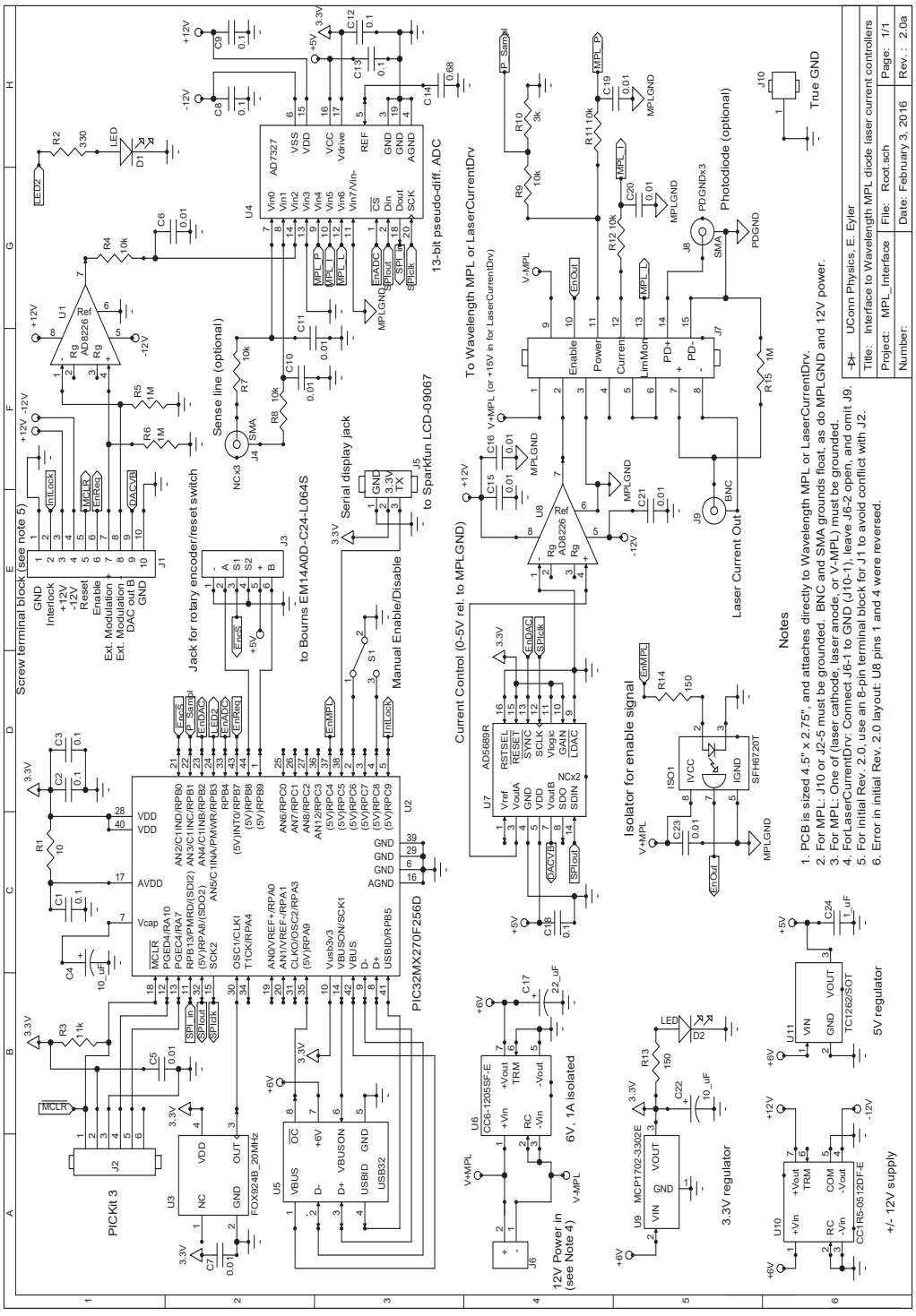
Screw terminal block (see note 5)
GND
Interlock
+12V
-12V
Reset
Enable
Ext. Modulation +
Ext. Modulation -
DAC out B
GND
PIC32MX270F256D
PICKit 3
Jack for rotary encoder/reset switch
to Bourns EM14A0D-C24-L064S
Sense line (optional)
Serial display jack
to Sparkfun LCD-09067
Manual Enable/Disable
13-bit pseudo-diff. ADC
AD7327
Current Control (0-5V rel. to MPLGND)
To Wavelength MPL or LaserCurrentDrv
Isolator for enable signal
Laser Current Out
Photodiode (optional)
True GND
12V Power in
(see Note 4)
6V, 1A isolated
3.3V regulator
5V regulator
+/- 12V supply
Notes
1. PCB is sized 4.5" x 2.75", and attaches directly to Wavelength MPL or LaserCurrentDrv.
2. For MPL: J10 or J2-5 must be grounded. BNC and SMA grounds float, as do MPLGND and 12V power.
3. For MPL: One of (laser cathode, laser anode, or V-MPL) must be grounded.
4. ForLaserCurrentDrv: Connect J6-1 to GND (J10-1), leave J6-2 open, and omit J9.
5. For initial Rev. 2.0, use an 8-pin terminal block for J1 to avoid conflict with J2.
6. Error in initial Rev. 2.0 layout: U8 pins 1 and 4 were reversed.
UConn Physics, E. Eyler
Title: Interface to Wavelength MPL diode laser current controllers
Project: MPL_Interface
File: Root.sch
Page: 1/1
Number:
Date: February 3, 2016
Rev.: 2.0a

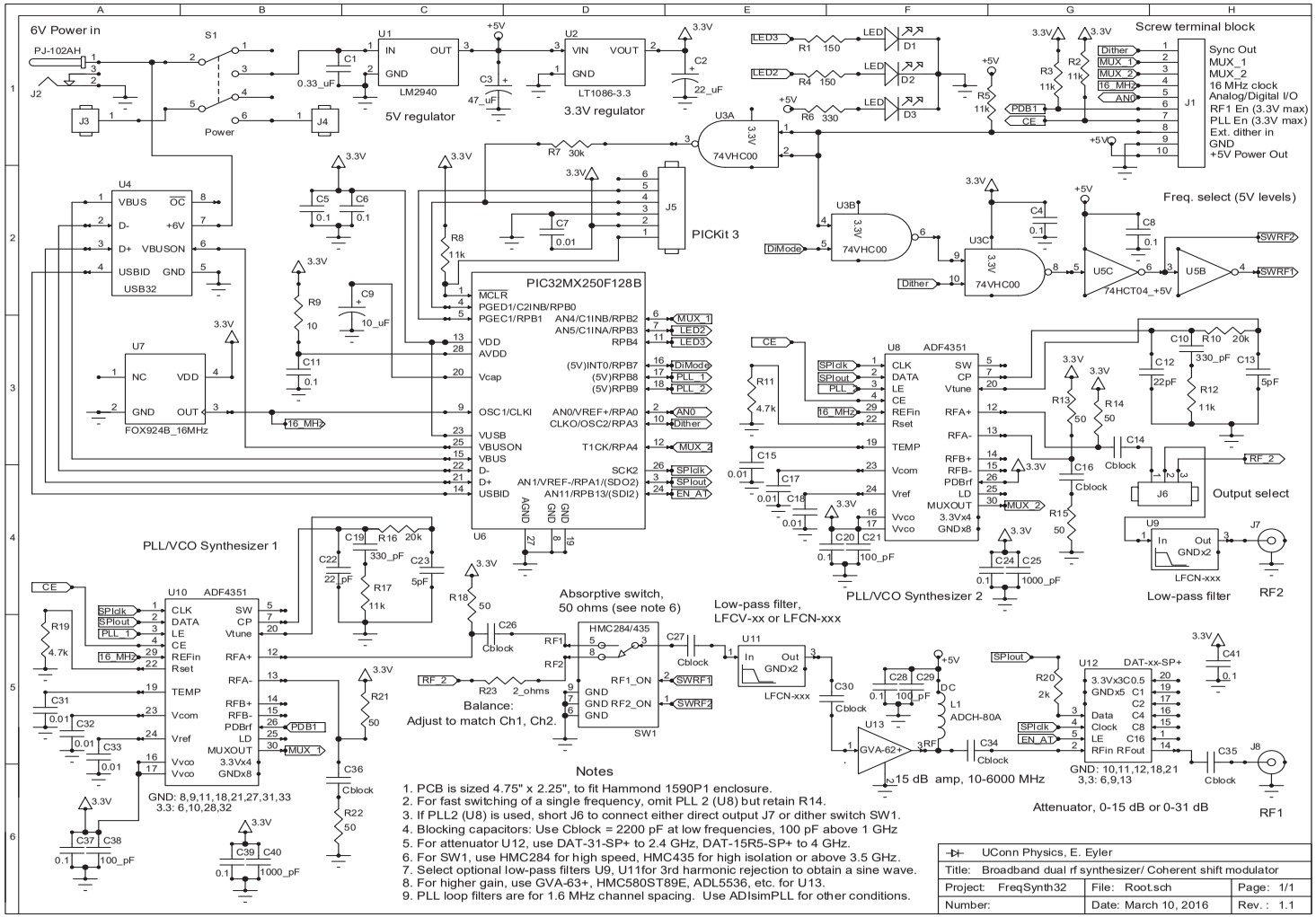

Notes

1. PCB is sized 4.75" x 2.25", to fit Hammond 1590P1 enclosure.
2. For fast switching of a single frequency, omit PLL 2 (U8) but retain R14.
3. If PLL2 (U8) is used, short J6 to connect either direct output J7 or dither switch SW1.
4. Blocking capacitors: Use Cblock = 2200 pF at low frequencies, 100 pF above 1 GHz
5. For attenuator U12, use DAT-31-SP+ to 2.4 GHz, DAT-15R5-SP+ to 4 GHz.
6. For SW1, use HMC284 for high speed, HMC435 for high isolation or above 3.5 GHz.
7. Select optional low-pass filters U9, U11for 3rd harmonic rejection to obtain a sine wave.
8. For higher gain, use GVA-63+, HMC580ST89E, ADL5536, etc. for U13.
9. PLL loop filters are for 1.6 MHz channel spacing. Use ADIsimPLL for other conditions.

UConn Physics, E. Eyler		
Title: Broadband dual rf synthesizer/ Coherent shift modulator		
Project: FreqSynth32	File: Root.sch	Page: 1/1
Number:	Date: March 10, 2016	Rev. : 1.1

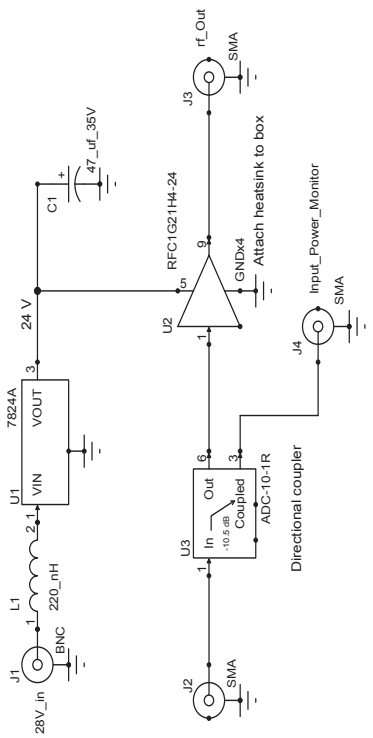

NOTES

1: For 1 W max, use RFC1G22-24. External heatsinking will be required, especially for 4W version.
2: U2 can be omitted and bypassed if not needed.
3: Size is 2.5" x 1.330", to fit Hammond 1590A box. To print, scale =1.2, xoffset -750, yoffset 1200.
4: For L1, use Bourns 9250A-221-RC or similar.

E. Eyler			
Title:	rf Power Amplifier (1W or 4W, 20-1000 MHz)		
Size:	A	Project: RF_PowerAmp	File: Root.sch
Date:	August 14, 2013	Sheet: 1	Revision: 1.0

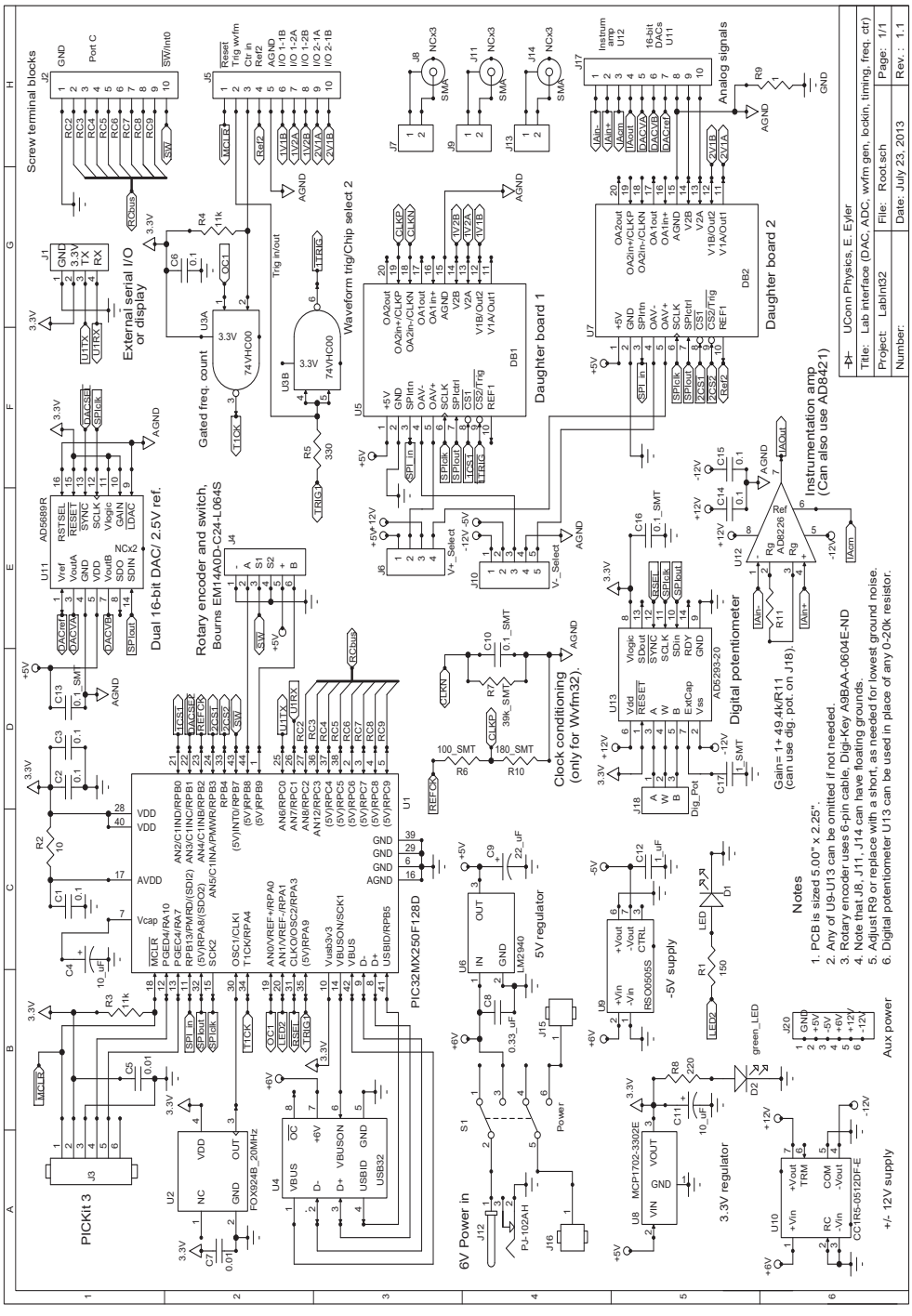
PICKit 3
Screw terminal blocks
External serial I/O or display
Dual 16-bit DAC/ 2.5V ref.
Rotary encoder and switch, Bourns EM14A0D-C24-L064S
Gated freq. count
Trig in/out
Waveform trig/Chip select 2
Daughter board 1
Daughter board 2
Analog signals
Instrumentation amp (Can also use AD8421)
Digital potentiometer
Clock conditioning (only for Wvfm32).
PIC32MX250F128D
5V regulator
-5V supply
3.3V regulator
6V Power in
Notes
1. PCB is sized 5.00" x 2.25".
2. Any of U9-U13 can be omitted if not needed.
3. Rotary encoder uses 6-pin cable, Digi-Key A9BAA-0604E-ND
4. Note that J8, J11, J14 can have floating grounds
5. Adjust R9 or replace with a short, as needed for lowest ground noise.
6. Digital potentiometer U13 can be used in place of any 0-20k resistor.
Aux power
+/- 12V supply
UConn Physics, E. Eyler
Title: Lab interface (DAC, ADC, wvfm gen, lockin, timing, freq, ctr)
Project: LabInt32
File: Root.sch
Page: 1/1
Number:
Date: July 23, 2013
Rev.: 1.1

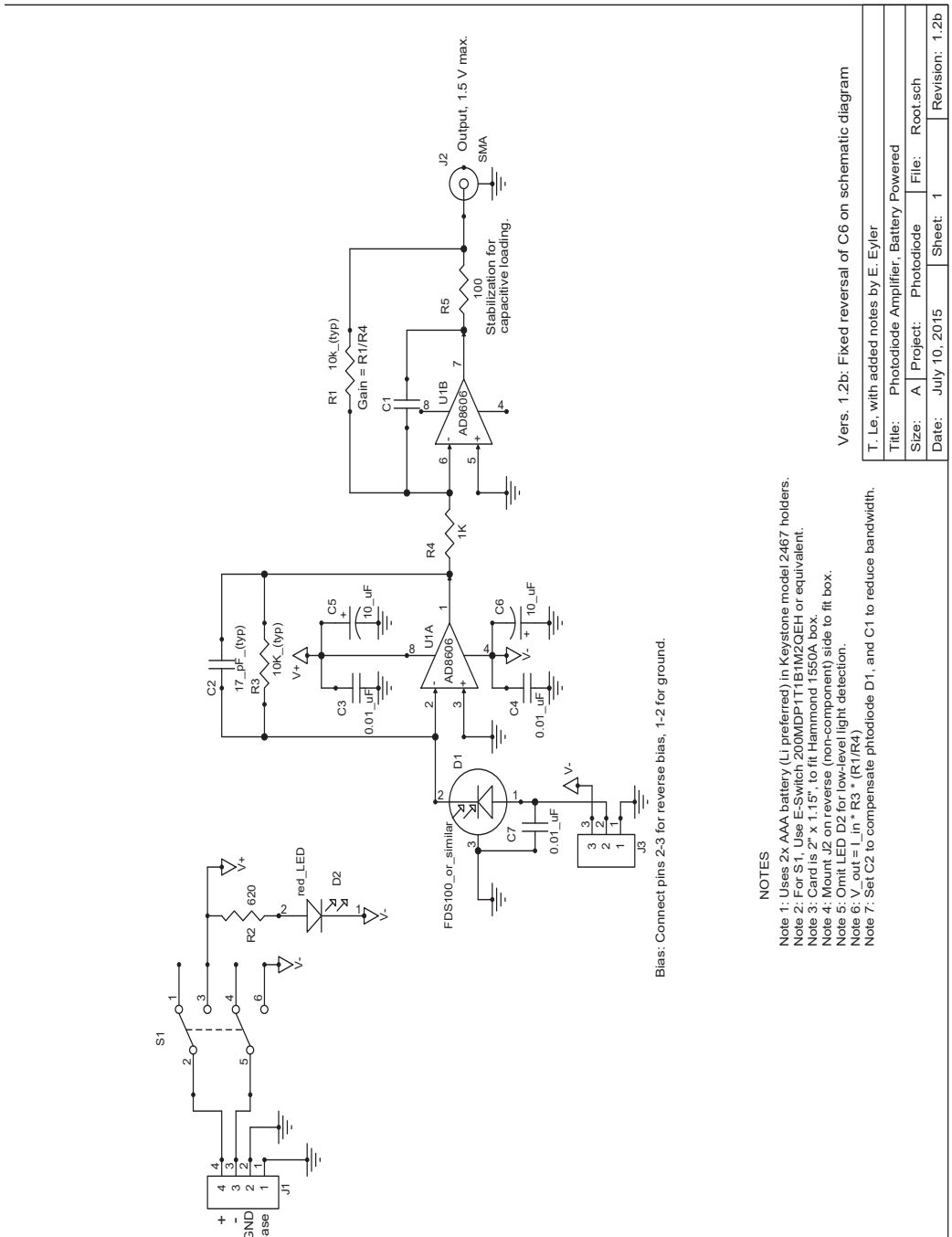
+
-
GND
Case
J1
S1
R2 620
red_LED
D2
V+
V-
FDS100_or_similar
D1
C7 0.01_uF
J3
Bias: Connect pins 2-3 for reverse bias, 1-2 for ground.
C2 17_pF_(typ)
R3 10K_(typ)
C3 0.01_uF
C5 10_uF
U1A AD8606
C4 0.01_uF
C6 10_uF
R4 1K
R1 10k_(typ)
Gain = R1/R4
C1
U1B AD8606
R5 100
Stabilization for capacitive loading.
J2
Output, 1.5 V max.
SMA
NOTES
Note 1: Uses 2x AAA battery (Li preferred) in Keystone model 2467 holders.
Note 2: For S1, Use E-Switch 200MDP1T1B1M2QEH or equivalent.
Note 3: Card is 2" x 1.15", to fit Hammond 1550A box.
Note 4: Mount J2 on reverse (non-component) side to fit box.
Note 5: Omit LED D2 for low-level light detection.
Note 6: V_out = I_in * R3 * (R1/R4)
Note 7: Set C2 to compensate phtodiode D1, and C1 to reduce bandwidth.
Vers. 1.2b: Fixed reversal of C6 on schematic diagram
T. Le, with added notes by E. Eyler
Title: Photodiode Amplifier, Battery Powered
Size: A
Project: Photodiode
File: Root.sch
Date: July 10, 2015
Sheet: 1
Revision: 1.2b

Appendix B

BCF Numerical Simulations

This code was originally developed by Drew Chieda [9], but subsequent modifications made by myself and others have increased the flexibility of the code to explore a more diverse parameter set. Most notably, I modified the code to allow for imbalances between the counterpropagating beams [38]. I also modified to code to allow for the exploration of polychromatic forces such as those discussed in chapter 6 [38]. These modifications were implemented in Mathematica as well as Fortran and are presented here for the case of imbalanced polychromatic forces (so as to prevent overloading the content with computer code).

Note that while I also modified the multilevel code written by Leland for some of my calculations, I am presenting only an annotated description of the modifications here. For the full text of the code, see the appendix of Leland's thesis [37].

B.1 Imbalanced Polychromatic Force

I present the code for the polychromatic force with provisions for left/right intensity imbalance.

B.1.1 Fortran Code

The Fortran code I wrote based on the work in [9] is below. For brevity, the header comments have been edited down for the main file and the ODE solver subroutine has been removed entirely. See the original source code for the full comments and ODE solver documentation.

```
C Original code provided by Hal Metcalf at SUNY Stony Brook
C Modified 10/2006 by Drew Chieda at UConn.
C Modified Feb. 2013 by Scott Galica at UConn for a 4-color
C light field using delta pulses (1st harmonic + 3rd harmonic)
C
C Modified June 19, 2013 by Scott Galica to allow for unequal
C left/right beams
C
C Definitions and formatting of the input file:
C wR     = Rabi frequency of a single beam
C q      = Beam imbalance (%)
C dsym   = detuning delta (g)
C d      = any asymmetry in the detuning, usually zero
C xphi   = phase between of counterpropagating waves (degrees)
C kvmin  = min velocity for calc (g/k)
C kvmax  = max velocity for calc (g/k)
C N      = number of steps between kvmin and kvmax to compute

      implicit real*8 (a-h,o-z)
      dimension F(5000), u(3), du(3)
      dimension work(100+21*3), iwork(5)
      integer n, ndata
      parameter (pi=3.1415926)
      external OBE      !optical bloch equations routine
      external ode      ! ODE numerical solver
      common wR, dsym, d, phi, dF, xkv, tend, q

C Open the input and output files, read ncalcs
      open(unit=11,file='Pforce3a.dat')  ! Input data file
      open(unit=12,file='Pforcurv3a.dat')! Output data file
      read(11,12)ncalcs
 12   format(i5)

C Loop on number of calculations, read parameter set
      do 123 ijk=1,ncalcs
      read(11,10)wR,dsym,d,xphi,xkvmin,xkvmax,n,q
 10   format(6f10.5,i5,f5.2)
```

```
      phi = (pi/180.)*xphi
      wR=wR/dsqrt(1+(q/200))

C Write parameters to output header (file and screen)
      write(6,11)
      write(6,10)wR,dsym,d,phi,xkvmin,xkvmax,n,q
      write(12,11)
      write(12,15)wR,dsym,d,phi,xkvmin,xkvmax,n,q
 11   format (' ',6X,'wR',4X,'dsym',9X,'d',9X,'phi',5X,'xkvmin'
     &,4X,'xkvmax',3X,'n',4X,'q')
 15   format(6f8.3,i5,f5.2)

      vrange=xkvmax-xkvmin
      ndata=0

C     loop on velocities
      do 1 xkv = xkvmin+vrange/(2.*n), xkvmax, vrange/n
         ndata=ndata+1
C      Initialize computational parameters for force and OBE:
        dF = 0.
        u(1) = 0.0
        u(2) = 0.0
        u(3) = -.5
C      Define Relative (rtol) and Absolute (atol) errors:
        rtol = 1.E-6
        atol = 1.E-5
        tstart = -1.
        dt = 1./(max(dabs(dsym), dabs(xkv))*10.)
        tend = 2*pi/dabs(xkv)*idint(1.+200*dabs(xkv)/dsym)

       FF=0.
       icount=0
       iflag=1
       ntime=idint((tend-tstart)/dt)

C     loop on time
          do 2 it=1,ntime
             tstop=tstart+dt
             call ode(OBE,3,u,tstart,tstop,rtol,atol,iflag,
                work,iwork)

             if (tstop.lt.0.0)go to 2
             icount=icount+1

C     Compute the force at t=tstop=tstart+dt
             dF= -2.*wR*(((2+(q/200))*dsin(xkv*tstop)
     &          *(dcos(phi/2.)*dcos(dsym*tstop)
     &          +dcos(3.*phi/2.)*dcos(3.*dsym*tstop))
```

```
     &            +(q/200)*dsin(xkv*tstop)
     &            *(dsin(phi/2.)*dsin(dsym*tstop)
     &            +dsin(3.*phi/2.)*dsin(3.*dsym*tstop)))*u(1)
     &            -((q/200)*dcos(xkv*tstop)
     &            *(dcos(phi/2.)*dcos(dsym*tstop)
     &            +dcos(3.*phi/2.)*dcos(3.*dsym*tstop))
     &            +(2+(q/200))*dcos(xkv*tstop)
     &            *(dsin(phi/2.)*dsin(dsym*tstop)
     &            +dsin(3.*phi/2.)*dsin(3.*dsym*tstop)))*u(2))
               FF=FF+dF
   2         continue

 9993    format(i7,4f15.2)
         F(ndata)=FF/icount
```

B.1.2 Mathematica Code

The corresponding Mathematica notebook is reproduced below. As in the Fortran case, many of the comments have been edited out for brevity. The full documentation is available in the original source notebook.

```
(* Program is based on bichromatic program "BCF ODE Num Model
   1.5"
Input file format given in "Force Input File Key_v1.3" *)

(* Define the functions for the Polychromatic field *)
a[t_]:=-2Sin[kv*t](Ol Cos[p1/2-(d1*t+h1)]-Or Cos[p1/2+(d1*t+h1)
   ]+Ol Cos[p2/2-(d2*t+h2)]-Or Cos[p2/2+(d2*t+h2)]);
b[t_]:=2Cos[kv*t](Ol Cos[p1/2-(d1*t+h1)]+Or Cos[p1/2+(d1*t+h1)
   ]+Ol Cos[p2/2-(d2*t+h2)]+Or Cos[p2/2+(d2*t+h2)]);

(* Select and read input file *)
{FileNameSetter[Dynamic[infile]],Dynamic[infile]}
{Browse,infile}
(* Open the input file, set file directory *)
instr=OpenRead[infile];
indir=DirectoryName[infile];
SetDirectory[indir];

(* Read number of batch calcs to make *)
ncalcs=Read[instr,Number];
dircount=1;
```

```
(* Generate output directory, file for each calc *)
While[DirectoryQ["BCF_"<>DateString[{"MonthShort","-","DayShort
    "}]<>"_"<>ToString[dircount]],dircount++];
outdir=CreateDirectory["BCF_"<>DateString[{"MonthShort","-","
    DayShort"}]<>"_"<>ToString[dircount]];
SetDirectory[outdir];
xkvstepsD=1;
ntimeD=1;
g1 = 1.0;  (* upper state decay rate, g/2 *)
g2 = 1.0; (* phenomenological dephasing rate *)

(* Progress bars for: *)
(* Batch calculations *)
ProgressIndicator[Dynamic[cprog],{1,ncalcs}]
(* Velocity steps *)
ProgressIndicator[Dynamic[vprog],{1,Dynamic[xkvstepsD]}]
(* Time steps *)
ProgressIndicator[Dynamic[tprog],{1,Dynamic[ntimeD]}]

(* Calculation kernel *)

(* Record time to completion (in seconds) *)
Timing[

(* Loop over number of calculations, ncalcs *)
Do[
cprog=calc;

(* Read computational parameters from input file *)
(* Rabi frequency in terms of g *)
O=N[Read[instr,Number]];
(* Percent intensity imbalance between +z and -z *)
a=N[Read[instr,Number]];
(* Symmetric bichromatic detunings in terms of g *)
d1= N[Read[instr,Number]];
d2=3d1;
(* asymmetry in the bichromatic detuning (usually 0) *)
dasym=N[Read[instr,Number]];
(* phase between counterpropagating beats (degrees) *)
xphi=N[Read[instr,Number]];
(* initial phase of waves in degrees *)
xtheta=0;
(* velocity limits of the calculation in terms of ?/k *)
xkvmin=N[Read[instr,Number]];
xkvmax=N[Read[instr,Number]];
(* velocity steps between kvmin and kvmax *)
```

```
xkvsteps=N[Read[instr,Number]];
xkvstepsD=xkvsteps;

(* prepare paramters for calculations *)
p1 = xphi/180*?;
p2=3?1;
h1= xtheta/180*?;
h2= 3?1;
Or=O/Sqrt[1+(a/200)]; (* Rabi frequency of z+ beam *)
Ol=(1+(a/200))*Or; (* Rabi frequency of z- beam *)
vrange = xkvmax-xkvmin;

(* Initialize force data table *)
BCF=Table[{i,0},{i,xkvmin+(vrange/(2xkvsteps)),xkvmax,vrange/
    xkvsteps}];

(* Open the output file and write header *)
(* output file name *)
outstr=OpenWrite["BCFout"<>ToString[calc]<>".dat"];
(* write parameters to the header *)
Write[outstr,"Calculation Number "<>ToString[calc]<>" of "<>
    ToString[ncalcs]];
Write[outstr,"Parameters"];
Write[outstr,"Rabi frequency = " <> ToString[O] <> " delta"];
Write[outstr,"Imbalance = " <> ToString[a] <> " %"];
Write[outstr,"Detuning = " <> ToString[d] <> " gamma"];
Write[outstr,"Asymmetry = " <> ToString[dasym] <> " gamma"];
Write[outstr,"Phase difference = " <> ToString[xphi] <> " deg"
    ];
Write[outstr,"Min kv = " <> ToString[xkvmin] <> " m/s"];
Write[outstr,"Max kv = " <> ToString[xkvmax] <> " m/s"];
Write[outstr,"Velcoty steps = " <> ToString[xkvsteps]];
(* --Add other output header information here-- *)

(* Loop over velocities *)
Do[
vprog=vcnt;
(* Initialize computational parameters for force and ODE *)
dF=0;
(* Define/reset computational rolerances *)
rtol=5; (* relative tolerance *)
atol = 5; (* absolute tolerance *)
tstart=-1;
(* Adjust loop end time, as in Fortran code *)
dt=10/(Max[Abs[d1],Abs[BCF[[vcnt,1]]]*10);
tend=2pi/Abs[BCF[[vcnt,1]]]*(1+200*Abs[BCF[[vcnt,1]]]/d1);
```

```
(* Reset force values to zero *)
FF=0;
icount=0;
iflag=1;
(* initial conditions for OBE *)
utemp=0;
vtemp=0;
wtemp=-0.5;
(* number of time steps *)
ntime=IntegerPart[(tend-tstart)/dt];
ntimeD=ntime;

(* Loop over time steps *)
Do[
tprog=tcnt;
(* assign new tstop *)
tstop=tstart+dt;
(* OBE solver *)
s=NDSolve[{u'[t]==-g2*u[t]-dasym v[t]+a[t] w[t],v'[t]==dasym
    u[t]-g2*v[t]+b[t] w[t], w'[t]==-a[t] u[t]-b[t] v[t]-2*g1*( w
    [t]+1),u[tstart]==utemp,v[tstart]==vtemp,w[tstart]==wtemp},{
    u,v,w}, {t, tstart, tstop},AccuracyGoal-> rtol,PrecisionGoal
    -> atol];
 If[tstop>0,
icount++;
(* calculate force over t?t+dt, add to total force (if t+dt>0)
    *)
dF=-2O((Ol Cos[p1/2-(d1*t+h1)]+Or Cos[p1/2+(d1*t+h1)]+Ol Cos[p2
    /2-(d2*t+h2)]+Or Cos[p2/2+(d2*t+h2)])Sin[BCF[[vcnt,1]]*tstop
    ] u[tstop]-(Ol Cos[[p1/2-(d1*t+h1)]-Or Cos[p1/2+(d1*t+h1)]+
    Ol Cos[p2/2-(d2*t+h2)]-Or Cos[p2/2+(d2*t+h2)])Cos[BCF[[vcnt
    ,1]]*tstop] v[tstop])/.s[[1]];
FF=FF+dF;
];
(* save output parameters for next input cycle *)
utemp=u[tstop]/.s[[1]];
vtemp=v[tstop]/.s[[1]];
wtemp=w[tstop]/.s[[1]];
tstart=tstop;
,{tcnt,1,ntime}];

(* Calculate average force & enter into the output table *)
BCF[[vcnt,2]]=FF/icount;
(* Write[outstr,{xkv[[v]],F[[v]]}]; *)
,{vcnt,1,xkvsteps}]
```

```
(* Save output force vs. velocity data to file *)
Export[outstr,BCF,"TSV"];
Close[outstr];
,{calc,1,ncalcs}]

(* Close the input file *)
Close[instr];
SetDirectory[indir];

] (* end timing call *)
```

B.2 Multi-Level Modifications

The modifications needed to implement imbalanced BCF forces are actually quite modest. The program as-written defines the full time-dependent Rabi-frequency explicitly. In the original version of the code: "mplusn_hamiltonian_v3.nb", the Rabi frequency is defined as a simplified form of the addition of 4 equally intense frequency components. After some algebra, this reduces to:

$$\Omega_{BCF}(z,t) = 4\Omega(\cos(\chi/2)\cos(z)\cos(\delta t+\theta)+i\sin(\chi/2)\sin(z)\sin(\delta t+\theta)), \quad \text{(B.2.1)}$$

where the BCF parameters are defined as usual and θ is an artificial phase parameter used to help speed up computation. The field parameters are read in from an external text file, as usual, and used to evaluate the expression as needed by the program.

In order to incorporate imbalance, this expression is modified to

$$\begin{aligned}\Omega_{BCF}(z,t) = {} & 2(\Omega_L\cos(\chi/2-(\delta t+\theta))+\Omega_R\cos(\chi/2+(\delta t+\theta)))\cos(z) \\ & +2i(\Omega_L\cos(\chi/2-(\delta t+\theta))-\Omega_R\cos(\chi/2+(\delta t+\theta)))\sin(z), \quad \text{(B.2.2)}\end{aligned}$$

where Ω_L and Ω_R are the Rabi frequency amplitude for the left-going and right-

going pulse trains, respectively. These two amplitudes are set independently in the external parameter text file, and thus an arbitrary imbalance can be applied. This modification is incorporated into the code version "mplusn_hamiltonian_v5.nb" which has had its input file similarly modified to read the additional field amplitude parameter.

Appendix C

LabView Program

The LabView program used for data acquisition is presented in full here. The data acquisition sequence is as follows:

1. Initialize parameters
    a. Read the length of acquisition, acquisition channels, pre-averaging, etc.
    b. Initialize the data destination variables
2. Setup virtual channel for acquisition of TOF data
    a. Initialize the channel
    b. Set channel parameters
    c. Wait for trigger
    d. Acquire data
    e. Close virtual channel
3. Wait for the virtual channel to free up the DAQ card
4. Setup virtual channel for acquisition of DC data
    a. Initialize the channel

b. Set channel parameters

c. Record DC channel data

d. Close virtual channel

5. Write data to output file

The user interface contains three primary windows alongside the parameter controls read by the program. The displays are for the last TOF trace acquired (with pre-averaging, if present), every TOF trace acquired (displayed after completing of the dataset), and live feed of the DC signals. The live feed is split into two parts: a fixed-width sub-window that is written to each shot and a scrolling window which features a zoomed-in subsection of the most recent data points in the fixed-width window data.

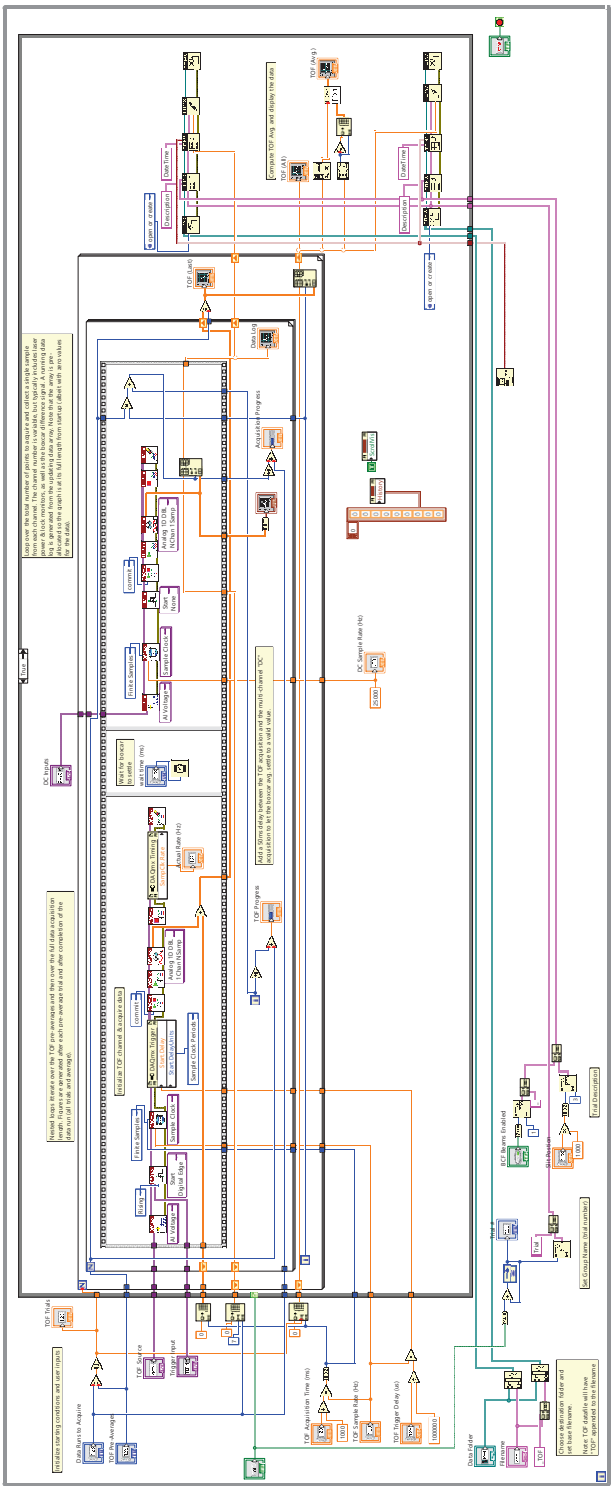

Fig. C.1: The data acquisition program used for the experiment. It can be divided into four subsections (detailed below): (A) initialization of parameters, (B) time-of-flight acquisition, (C) diagnostic acquisition, and (D) data output.

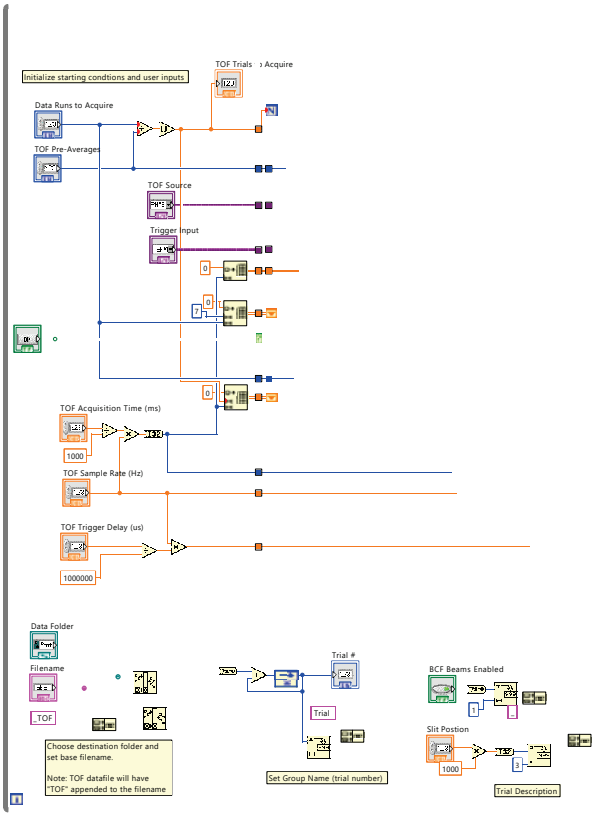

Fig. C.2: (A) Parameter initialization. This section of code is primarily responsible for reading the user input information including file name, number of shots, source channels, and pre-averaging length. This section also generates the header information about number of BCF beams and position which is then written to the output file.

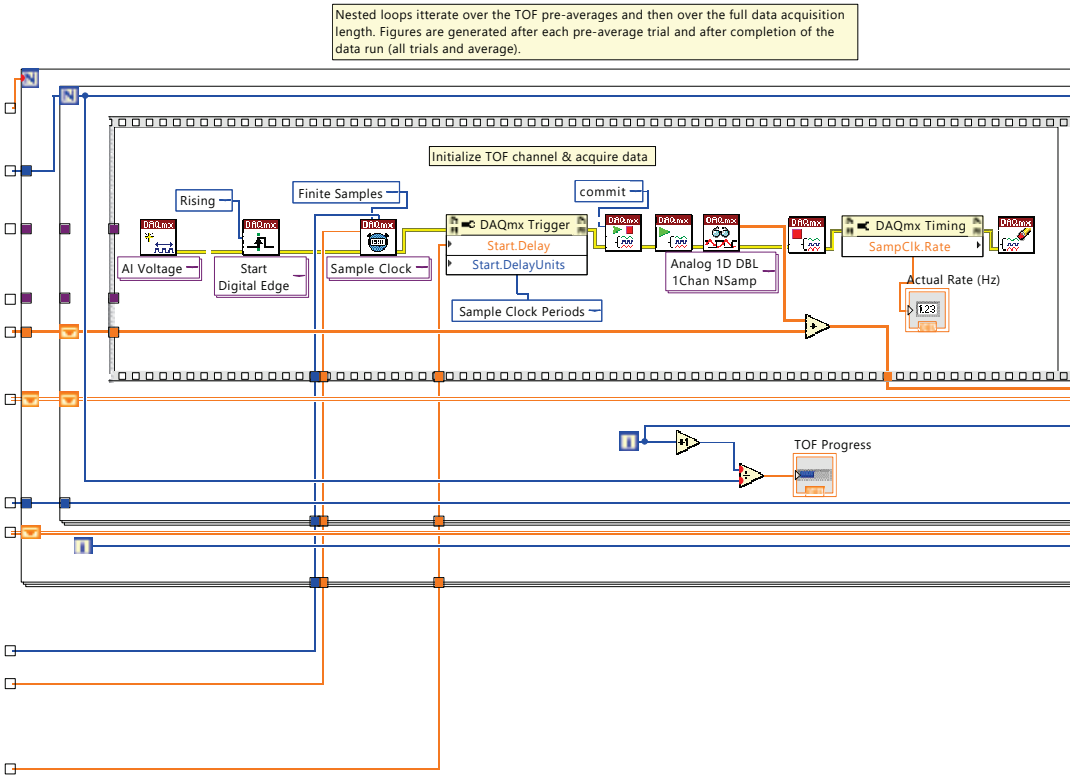

Fig. C.3: (B) Time-of-flight (TOF) acquisition. This section of code initializes the virtual channel necessary for acquisition of TOF data. The virtual channel is configured to collect data from a single input at the maximum sample rate allowed by the DAQ card. Acquisition is triggered by a TTL input signal and lasts for a user-adjustable duration (typically 3 ms). After acquisition has finished, the channel is disabled. Disabling allows us to change the acquisition parameters for the (much slower) diagnostic signals.

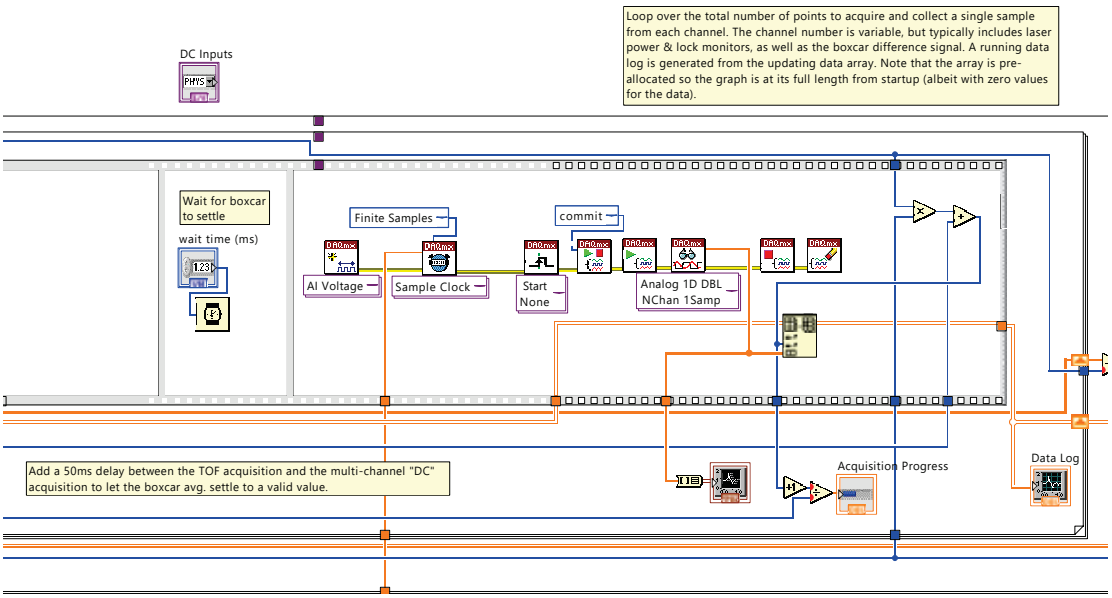

Fig. C.4: (C) Diagnostic signal acquisition. After a user-input wait time, the data input channels are reconfigured to take a single sample from each of the (up to) seven remaining analog signal inputs. Unfortunately, the start of this acquisition stage cannot be explicitly triggered, but given that all of the diagnostic signals are essentially DC values (refreshed at the repetition rate) the exact start time is irrelevant. For the purpose of shuttered acquisition, this section also includes a shutter toggle which is generated by outputting the shot count to a logic output. By using the least-significant bit of the shot count, the shutter can be made to switch state after every shot. Similar to the diagnostic acquisition, the shutter output cannot be explicitly triggered and instead relies on user-tuning of an adjustable delay to set the proper signal timing.

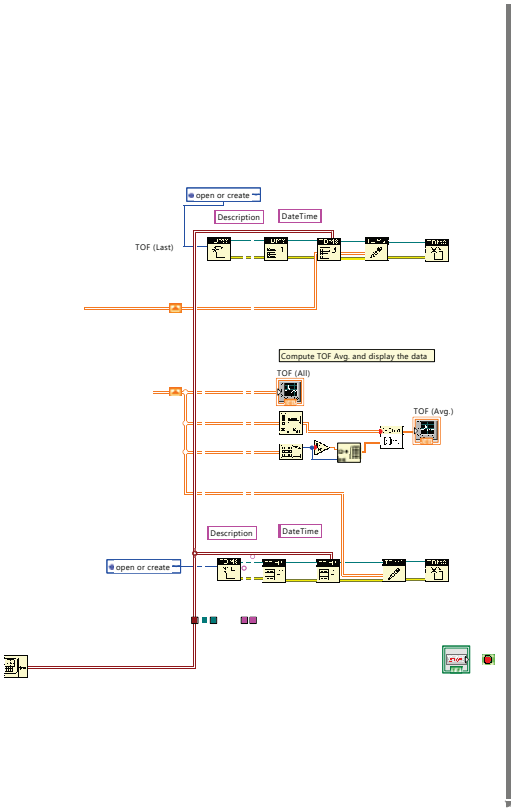

Fig. C.5: (D) Data output writing. After the full acquisition set has concluded, the complete data arrays for TOF and diagnostic signals are written to a TDMS file. The filename is specified in the input parameter section. The TOF file is differentiated from the diagnostic data file by appending "_TOF" to the principal filename. In addition to the data, a header page is included which contains (for each trial) the slit position, BCF beam condition (indicated by a number), time-stamp, and trail number. The header was formatted to match an earlier version of the data acquisition program.

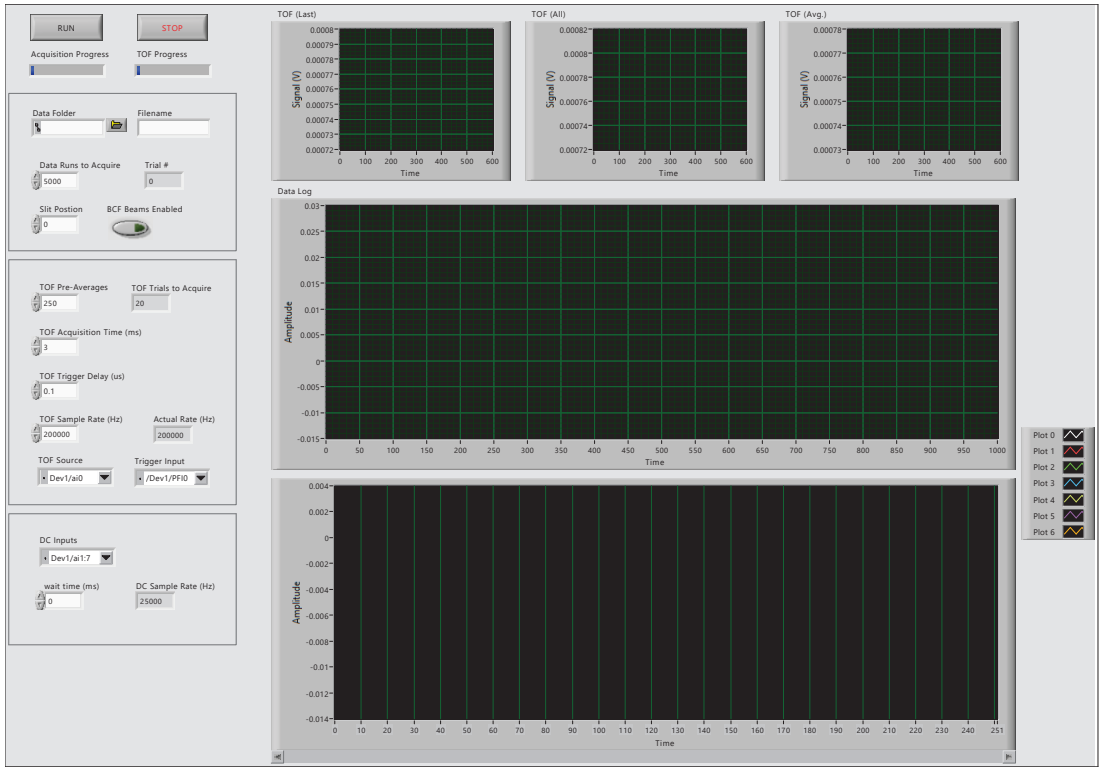

Fig. C.6: The front panel of the data acquisition program is shown here. The data fields at left correspond to the input parameters outlined in block diagram section (A). The plots can be divided into two sections: TOF and diagnostic. The three small plots across the top of the panel are TOF monitors. The leftmost figure displays the last TOF shot acquired (if pre-averaging is enabled it shows the last complete pre-average). The center figure shows all of the individual TOF trials (or pre-averages) after completion of the acquisition trial. The rightmost figure shows the complete TOF average across the full acquisition trial. Below the TOF figures, a fixed-width chart shows the complete diagnostic data for the entire acquisition trial. The plot is updated after every shot. The bottom figure is a strip-chart which shows a zoomed-in view of the total diagnostic data chart. This moving chart stores the last ∼1000 data-points for each channel and displays the per-shot update as a moving 250-point wide display.

Appendix D

Matlab Code

The following is a sampling of the catalog of data processing programs written in Matlab for analysis of the BCF experiment and related setup experiments. Included in this appendix are: a loading program for the TDMS output files generated by the data acquisition program, the experimental deflection simulation program (including haircut averaging sub-function), a Gaussian image fitting program based on code taken from Ryan Carollo and the University of Colorado, and a program to linearize and shift laser frequency scans.

D.1 TDMS Loading Program

This program is based on the example code provided by National Instruments for reading TDMS files into Matlab. It has been modified to read the specific formatting of the TDMS files generated by the LabView data acquisition program shown in C.

```
% TDMSread.m
%
% Edited: 18 Aug 17
%
% Edited version of the example read script from the NI website

function [out, outc]=TDMSread(file)
%% Get file to process and initialize NI library
```

```
% If no file is specified, pull up file selection dialog
if nargin==0
    % Prompt user to pick file to process
    [tfile, tpath]=uigetfile({'*.TDMS';'*.TDM';'*.*'},'Pick a
       file to process');

    % Selection canceled returns zeros
    if tfile==0
        outc=0;
        out=0;
        fprintf('\nThe import was canceled.\n\n')
        return
    end

    % Generate filename
    file=strcat(tpath,tfile);
end

%Recreate needed property constants defined in nilibddc_m.h
DDC_FILE_NAME                                   =       'name';
DDC_CHANNELGROUP_NAME                   =       'name';
DDC_CHANNELGROUP_DESCRIPTION    =       'description';
DDC_CHANNELGROUP_DATETIME       =   'datetime';

% Define the paths to 'nilibddc.dll' and 'nilibddc_m.h'
NI_TDM_DLL_Path='C:\Users\Scott\Documents\MATLAB\nilib_files\
   dev\bin\nilibddc.dll';
NI_TDM_H_Path='C:\Users\Scott\Documents\MATLAB\nilib_files\dev\
   include\nilibddc_m.h';
libname='nilibddc';

% Write the file path to the called variable
Data_Path=file;

%Load nilibddc.dll (Always call 'unloadlibrary(libname)' after
   finished using the library)
loadlibrary(NI_TDM_DLL_Path,NI_TDM_H_Path);

%Open the file (Always call 'DDC_CloseFile' when you are
   finished using a file)
fileIn = 0;
[~,~,~,file]=calllib(libname,'DDC_OpenFileEx',Data_Path,'',1,
   fileIn);

%Read and display file name property
```

```
filenamelenIn = 0;
%Get the length of the 'DDC_FILE_NAME' string property
[err,~,filenamelen]=calllib(libname,'
    DDC_GetFileStringPropertyLength',file,DDC_FILE_NAME,
    filenamelenIn);
if err==0 %Only proceed if the property is found
    %Initialize a string to the length of the property value
    pfilename=libpointer('stringPtr',blanks(filenamelen));
    [~,~,filename]=calllib(libname,'DDC_GetFileProperty',file,
        DDC_FILE_NAME,pfilename,filenamelen+1);
    setdatatype(filename,'int8Ptr',1,filenamelen);
    disp(['File Name: ' char(filename.Value)]);
end

%Get channel groups
%Get the number of channel groups (trials)
numgrpsIn = 0;
[~,numgrps]=calllib(libname,'DDC_GetNumChannelGroups',file,
    numgrpsIn);
%Get channel groups only if the number of channel groups is
    greater than zero
if numgrps>0
        %Initialize an array to hold the desired number of
            groups
    pgrps=libpointer('int64Ptr',zeros(1,numgrps));
    [~,grps]=calllib(libname,'DDC_GetChannelGroups',file,pgrps,
        numgrps);
end

%% Import data arrays

% Initialize the output structure
out=struct('init',cell(numgrps,1));

% Show progress of import, break if cancel
H=waitbar(0,'Importing...','CreateCancelBtn',...
    'setappdata(gcbf,''canceled'',1)');

% Initialize Canceled flag
setappdata(H,'canceled',0)

%For each channel group (trial)
for i=1:numgrps

    % Check for canceled flag and break if needed
    if getappdata(H,'canceled')
```

```
    fprintf('\nThe import was canceled:\nLoaded %u out of %
        u files\n\n',i-1,numgrps)
    break
end

%Get channel group name property (trial name)
grpnamelenIn = 0;
[err,~,grpnamelen]=calllib(libname,'
    DDC_GetChannelGroupStringPropertyLength',grps(i),
    DDC_CHANNELGROUP_NAME,grpnamelenIn);
if err==0 %Only proceed if the property is found
            %Initialize a string to the length of the
                property value
    pgrpname=libpointer('stringPtr',blanks(grpnamelen));
    [~,~,grpname]=calllib(libname,'
        DDC_GetChannelGroupProperty',grps(i),
        DDC_CHANNELGROUP_NAME,pgrpname,grpnamelen+1);
    setdatatype(grpname,'int8Ptr',1,grpnamelen);
else
    grpname=libpointer('stringPtr','');
end
% Write the group name to the output
out(i).Name=char(grpname.Value);


% Get channel group timestamps
yearIn = 0;
monthIn = 0;
dayIn = 0;
hourIn = 0;
minuteIn = 0;
secondIn = 0;
msecondIn = 0;
wkdayIn = 0;
[err,~,~,~,~,hour,minute,second,msecond,~]=calllib(libname,
    'DDC_GetChannelGroupPropertyTimestampComponents',grps(i)
    ,DDC_CHANNELGROUP_DATETIME,yearIn,monthIn,dayIn,hourIn,
    minuteIn,secondIn,msecondIn,wkdayIn);
if err==0 %Only proceed if the property is found
   % Append 0s if the values are single-digit
    if hour<10
        h=['0' num2str(hour)];
    else
        h=num2str(hour);
    end
    if minute<10
```

```
        m=['0' num2str(minute)];
    else
        m=num2str(minute);
    end
    if round(second+msecond/1000)<10
        s=['0' num2str(round(second+msecond/1000))];
    else
        s=num2str(round(second+msecond/1000));
    end

    % Combine the strings into a complete timestamp
    time=[h ':' m ':' s];
    clear h m s
end
% Write the timestamp to the output
out(i).Time=time;


% Get channel group description property
grpdesclenIn = 0;
[err,~,grpdesclen]=calllib(libname,'
   DDC_GetChannelGroupStringPropertyLength',grps(i),
   DDC_CHANNELGROUP_DESCRIPTION,grpdesclenIn);
if err==0 %Only proceed if the property is found
            %Initialize a string to the length of the
                property value
    pgrpdesc=libpointer('stringPtr',blanks(grpdesclen));
    [~,~,grpdesc]=calllib(libname,'
        DDC_GetChannelGroupProperty',grps(i),
        DDC_CHANNELGROUP_DESCRIPTION,pgrpdesc,grpdesclen+1);
    setdatatype(grpdesc,'int8Ptr',1,grpdesclen);
end
% Save the group description to a temp variable
tmp=char(grpdesc.Value);

% Split the description and write to the output
out(i).Position=str2double(tmp(3:end));
out(i).Green=str2double(tmp(1));
clear tmp


%Get channels (number of shots)
numchansIn = 0;
%Get the number of channels (shots) in this channel group (
   trial)
```

```
[~,numchans]=calllib(libname,'DDC_GetNumChannels',grps(i),
    numchansIn);
%Get channels only if the number of channels is greater
    than zero
if numchans>0
            %Initialize an array to hold the desired number
                of channels
    pchans=libpointer('int64Ptr',zeros(1,numchans));
    [~,chans]=calllib(libname,'DDC_GetChannels',grps(i),
        pchans,numchans);
end

% Initialize an empty matrix to hold the data
chanvals=zeros(0);

%For each channel (shot) in the channel group (trial)
for j=1:numchans

    %Get channel data type
    typeIn = 0;
    [~,type]=calllib(libname,'DDC_GetDataType',chans(j),
        typeIn);

    %Get channel values if data type of channel is double (
        DDC_Double = 10)
    if strcmp(type,'DDC_Double')
        numvalsIn = 0;
        [~,numvals]=calllib(libname,'DDC_GetNumDataValues',
            chans(j),numvalsIn);
                %Initialize an array to hold the
                    desired number of values
        pvals=libpointer('doublePtr',zeros(1,numvals));
        [~,vals]=calllib(libname,'DDC_GetDataValues',chans(
            j),0,numvals,pvals);
        setdatatype(vals,'doublePtr',1,numvals);

        %Add channel values to a matrix. The comment, #ok<
            AGROW>, at
        %the end of the line prevents warnings about the
            matrix needing
        %to allocate more memory for the added values.

        % Append the data for each shot to an array
        chanvals(:,j)=(vals.Value);

    end
```

```
    end

    % Write the trial data array to the output
    out(i).Data=chanvals;

    % Update waitbar
    waitbar(i/numgrps)

end

%% Print a completion message and close the NI library

% Print a message if the import succeeded
if ~(getappdata(H,'canceled'))
    fprintf('The import completed successfully:\n%u files
        imported.\n\n',numgrps)
end

% Delete the waitbar
delete(H)

%Close file
err = calllib(libname,'DDC_CloseFile',file); %#ok<NASGU>
%Unload nilibddc.dll
unloadlibrary(libname);

% Remove initialization field from output structure
out=rmfield(out,'init');

% Convert to a cell array (optional output)
outc=struct2cell(out);

end
```

D.2 BCF Simulation

The following is the code used to compute the theoretical BCF shifts.

```
% ---BCF Simulation, v3.1---
%

%% ---Define Contants-----------------------------------------

% Initialize a structure to hold all the constants
c=struct;

% ---Physical Constants-------------------------------
c.m=(40.078+18.998403)*(1.660538921e-27);          % CaF mass [kg]
c.hbar=1.054571726e-34;                                % h-bar [Js]
c.lm=531.9e-9;                                  % BCF wavelength [m]
c.tau=25.1e-9;                                 % B state lifetime [s]
c.Gamma=1/c.tau;                             % B state decay rate [Hz]
c.k=2*pi/c.lm;                            % wave vector magnitude [1/m]

% ---Experimental Parameters--------------------------
c.del=2*pi*(190e6);                    % Bichromatic detuning [rad/s]
c.ap=1e-3;                          % Pulsed valve aperture diameter [m]
c.dskm=1e-3;                                    % Skimmer diameter [m]
c.hbcf=0.6964;          % Horz. waist radius of BCF beam (5) [mm]
c.vbcf=0.4782;          % Vert. waist radius of BCF beam (5) [mm]
c.Lpre=251.206e-3;                         % Valve-to-BCF length [m]
c.Lpreu=177.374e-3; % Eff. point source (EPS)-to-BCF length [m]
c.Lpost=223.3285e-3;                     % BCF-to-detection length [m]
c.vbeam=415;                            % Mean CaF beam velocity [m/s]
c.dt1=c.Lpreu/c.vbeam;                             % EPS-to-BCF time [s]
c.dt2=c.Lpost/c.vbeam;                           % BCF-to-detection time [s]
c.fwhm=6.3915;          % Undeflected beam FWHM (measured) [mm]
c.mask=1.5;                                % Detection mask width [mm]
c.slit=0.76;                               % Spatial filter width [mm]

%% ---Undeflected Beam Data----------------------------------------

% ---Import the undeflected beam data-----------
ref=load('C:\Users\Scott\Documents\MATLAB\BCF Data Analysis\
    bcf_all.mat','pos','rel');
ref=[ref.pos', ref.rel.avg(:,1)-min(ref.rel.avg(:,1))];

% Find beam center (4)
x_avg=sum(ref(4:11,1).*ref(4:11,2))/sum(ref(4:11,2));
```

```
% Write shifted dimension to ref
ref(:,3)=ref(:,1)-x_avg;

% Generate xi, yi, P(xi) variables centered on x_avg
n=1000;
xi=linspace(-c.fwhm,c.fwhm,n); % [mm]
yi=linspace(-c.mask/2,c.mask/2,round(c.mask*n/(2*c.fwhm)));
Pxi=interp1(ref(:,1)-x_avg,ref(:,2),xi,'linear',0);

% Generate prob. distributions (weights) from P(xi)
Pxi=Pxi/trapz(xi,Pxi);


%---Generate symmetric data for Pyi (2)----------

% Fold Pxi over and average it onto itself
Pyii=mean(cat(1,Pxi(1:ceil(n/2)),flip(Pxi(1+floor(n/2):end)))
    ,1);

% Unfold Pyi and interpolate on the domain yi
Pyii=cat(2,Pyii,flip(Pyii(1:end-mod(length(Pyii),2))));
Pyi=interp1(xi,Pyii,yi,'linear',0);

% Generate a prob. distribution from P(yi) (normalize to 1)
Pyi=Pyi/trapz(yi,Pyi);


%---Initialize the dataspace---------------------

% Generate a position mesh
[X,Y]=meshgrid(xi,yi);

% Compute velocity meshes, vi=dx/dt=X/(t1+t2) [mm/s]
vx=X./(c.dt1+c.dt2);
vy=Y./(c.dt1+c.dt2);


%---Propagate the beam backwards (3)-------------

% Compute position at BCF
X=X-vx*c.dt2;
Y=Y-vy*c.dt2;

% Write the initial beam conditions, distribution to variables
init=cat(3,X,Y,vx,vy);
Pxy=Pyi'*Pxi;
```

```
%% ---Force Simulation Data-----------------------------------------

% ---Import the force data-----------------------------

% Set file path
path='C:\Users\Scott\Documents\Grad_UConn\Research\Numerical
    Models\Multi-Level\Force vs. Intensity';
file='FvW_noI_045.xlsx';

% Import the excel file
[data, header]=xlsread([path '\' file],'data_force');

% Split into useful variables
v=data(:,1); % [Gamma/k]
F=data(:,2:end); % [hbar k Gamma/2]
W=cell2mat(cellfun(@(x)str2double(x(3:end)),header(2:end),'
    UniformOutput',0));


% ---Generate F(y,z) surface-----------------------

% Compute Avg. Force over m points [hbar k Gamma/2]
F_avg=haircut(F,v,-2.45,2.45,0);

% Convert W_Rabi to intensity
Ir=45.2*(W/63.64).^2;

% Generate domain for intensity data
[zi,yi]=meshgrid(linspace(-2*c.hbcf,2*c.hbcf),init(:,1,2));

% Generate a beam intensity surface [W/cm^2]
I=max(Ir)*exp(-(zi.^2)/(c.hbcf^2/2)).*exp(-(yi.^2)/(c.vbcf^2/2)
    );

% Compute the force at each intensity [hbar k Gamma/2]
Fxy=interp1(Ir,F_avg,I,'spline');


% ---Compute ideal/simplified shift (1)-----------

% Compute change in x-momentum vs height (y) (integrate z)
dpx=trapz(zi(1,:)/1000,Fxy,2)*(c.hbar*c.k*c.Gamma/2)/c.vbeam;

% Compute the average change in momentum
```

```
Dp=trapz(yi(:,1),dpx)/(yi(end,1)-yi(1,1));

% Compute the average force
DpDt=Dp/((zi(1,end)-zi(1,1))/c.vbeam);


%% ---Simulate Interaction-----------------------------------------

% ---Shift the distribution coordinates----------

% Compute dvx [mm/s]
dvx=1000*repmat(dpx,1,size(init,2))/c.m;

% Apply the velocity change to init, write to final
final=cat(3,init(:,:,1),init(:,:,2),...
      init(:,:,3)+dvx,init(:,:,4));

% Propagate the beam forwrad in time
final(:,:,1)=final(:,:,1)+final(:,:,3)*c.dt2;
final(:,:,2)=final(:,:,2)+final(:,:,4)*c.dt2;

init(:,:,1)=init(:,:,1)+init(:,:,3)*c.dt2;
init(:,:,2)=init(:,:,2)+init(:,:,4)*c.dt2;


%% ---Simulate Detection-------------------------------------------

% ---Re-fit data to the dectector----------

% Define detection domain
[detx,dety]=meshgrid(...
     linspace(ref(1,3)-c.slit,ref(end,3)+c.slit,size(init,2)),
     linspace(-c.mask/2,c.mask/2,size(init,1)));

% Interpolate the distributions
detPi=interp2(init(:,:,1),init(:,:,2),Pxy,detx,dety);
detPf=griddata(final(:,:,1),final(:,:,2),Pxy,detx,dety);


% ---Integrate over slit positions----------

% Integrate over y
intyPi=trapz(dety(:,1),detPi);
intyPf=trapz(dety(:,1),detPf);

% Find the limits of integration
```

```
lim(:,1)=ref(:,3)-c.slit/2;
lim(:,2)=ref(:,3)+c.slit/2;

% Integrate over each x-interval
sig=zeros(13,2);
ind=[0,0];
for i=1:length(lim)

    % Find the limit indicies
    [~,ind(1)]=min(abs(detx(1,:)-lim(i,1)));
    [~,ind(2)]=min(abs(detx(1,:)-lim(i,2)));

    % Integrate over the indicies
    sig(i,1)=trapz(detx(1,ind(1):ind(2)),intyPi(ind(1):ind(2)));
    sig(i,2)=trapz(detx(1,ind(1):ind(2)),intyPf(ind(1):ind(2)));
end
clear i

% Compute the average location of each and the shift
x_avg=sum(sig(4:11,:).*ref(4:11,3))./sum(sig(4:11,:));
shift=diff(x_avg);
```

D.2.1 Haircut Function

The accessory haircut function is included below.

```
% ---BCF 'Haircut' Function, v2.0---

function [avg, metrics]=haircut(data,v,vllim,vulim,flag)
%% ---Input Handling-----------------------------------------------

% ---Check the inputs---------------------------------

% Count the inputs and set default values
switch nargin
    case {1,2,3} % Data is always the first variable, v is
        useless w/o limits
        lind=1;
        uind=length(data);
        fflag=0;
    case 4 % Assume the figures aren't wanted unless specified
        [~, lind]=min(abs(v-vllim));
        [~, uind]=min(abs(v-vulim));
        fflag=0;
    case 5
        [~, lind]=min(abs(v-vllim));
        [~, uind]=min(abs(v-vulim));
        fflag=flag;
    otherwise
        disp('Error: too many input variables')
        return
end


% ---Initialize parameters----------------------------

% Pull out the relevant data from the full set
F=data(lind:uind,:);

metrics.data0=data;
metrics.F0=F;

% Compute the mean, std of the data and save a copy of them
favg0=mean(F,1);
fstd0=std(F,0,1);

metrics.favg0=favg0;
metrics.fstd0=fstd0;
```

```
% Initialize the comparison variables
favg=ones(size(favg0));
favg1=zeros(size(favg0));

% Check the plot flag
if fflag
    figure
    subplot(1,2,1)
    plot(data)
    line([lind lind],[-4.5 4.5])
    line([uind uind],[-4.5 4.5])
    axis([0 size(data,1) -4.5 4.5])
end

%% ---Data Processing-----------------------------------------

% Record the sign, magnitude of the forces (2)
sgn=sign(F);
F=abs(F);

count=0;

% ---Peak trimming-------------------------------

% As long as the avg changes, keep cutting
while any(favg-favg1)

    % Check the avg before the cut
    favg=repmat(mean(F,1),size(F,1),1);
    fstd=repmat(std(F,0,1),size(F,1),1);

    % Find what needs to be cut
    ind=(F>(favg+fstd));

    % Replace any cut indicies with the avg value
    F(ind)=favg(ind);

    % Compare the avg before vs. after the cut
    favg=favg(1,:);
    favg1=mean(F,1);

    count=count+1;
end

% Reapply polarity
```

```
F=sgn.*F;

% Insert trimmed data back into full set
data1=cat(1, data(1:(lind-1),:), F, data((uind+1):end,:));

%% ---Write Outputs-----------------------------------------------

% Write the average to the output
avg=mean(F,1);

% Write add'l variables
metrics.count=count;
metrics.data=data1;
metrics.F=F;
metrics.favg=avg;
metrics.fstd=std(F,0,1);

% Plot the trimmed data (if desired)
if fflag
    subplot(1,2,2)
    plot(data1)
    line([76 76],[-4.5 4.5])
    line([125 125],[-4.5 4.5])
    axis([0 200 -4.5 4.5])
end
end
```

D.3 Frequency Scan Fitting

This program uses marker interferometer peaks to linearize the frequency axis of a laser scan and shifts the 0 to one of the recorded spectral features.

```
%% TDMS CaF Spectrum Data Conditioning v1.1
%

function [f, p, S]=CaFfreqFit(dataIn)
%% Plot the input data

% Grab the input variable name
a=inputname(1);

% Collect dimension information from the input data
[l, NumChan]=size(dataIn);
label={'CH1','CH2','CH3','CH4','CH5','CH6','CH7','CH8'};

% Open a new figure, plot the data
figure
plot(dataIn)
xlabel('Index')
title(a)
legend(label{1:NumChan},'Location','SouthOutside','Orientation'
    ,'Horizontal')

% Query the number of reference peaks in the dataset
np=inputdlg('How many reference peaks to fit?','Reference Peaks
    ',1,{'4'});
numPeaks=str2double(np);

% Query the approximate location of each reference peak
n=ginput(numPeaks);
n=round(n);
dn=round(l/20);

% Find the actual location of each reference peak
for i=1:numPeaks

    % Define the search range min & check for out-of-range
        index
    if (n(i)-dn)<1
        nmin=1;
    else
        nmin=n(i)-dn;
```

```
    end

    % Define the search range max & check for out-of-range
        index
    if (n(i)+dn)>l
        nmax=l;
    else
        nmax=n(i)+dn;
    end

    % Find the ref peak location and overwrite the guess value
    [~, imax]=max(dataIn(nmin:nmax,1));
    n(i,1)=nmin+imax-1;
    n(i,2)=300*(i-1);
end

clear nmin nmax i maxV imax np

% Find the index for the frequency zero
h=msgbox('Please select f0');
uiwait(h)
n0=ginput(1);
n0=round(n0(1));

% Define search min
if (n0-floor(dn/3))<1
    n0min=1;
else
    n0min=n0-floor(dn/3);
end

% Define search max
if (n0+floor(dn/3))>l
    n0max=l;
else
    n0max=n0+floor(dn/3);
end

% Figure out which channel has the reference spectrum data
if (NumChan)>=4
    chN=4;
else
    chN=NumChan;
end

% Find the I2 peak minimum
```

```
[~, imin]=min(dataIn(n0min:n0max,chN));
n0=n0min+imin-1;

% Fit the reference peaks to a polynomial
ind=(1:l);
[p, S]=polyfit(n(:,1),n(:,2),min([size(n,1)-1 2]));
f=polyval(p,ind);
f0=polyval(p,n0);
f=(f-f0)';

close

end
```

D.4 Gaussian Image Fitting

I made use of a 2D Gaussian fitting function in order to extract laser beam parameters from pictures taken of the beam. The code I used was based on code from Ryan Carollo and the JILA BEC & Ultracold Atoms group (available at: http://jilawww.colorado.edu/bec/BEC_for_everyone/matlabfitting.htm). I edited it slightly to better fit my needs, but the main body of the code is mostly taken from the original JILA code so it is not worth reproducing here. I've included this section as a reference in order to draw attention to the original code (for the convenience of others in the future).

Appendix E

Laser Alignment

The following are general use procedures for the major laser systems used in the BCF experiment. Since the experiment has been dismantled at this point, it is questionable how useful these will be, but they should provide some general-knowledge tips and tricks for using the laser systems in the future (particularly the 699 dye laser).

For the 699, I wrote a set of procedures meant as a helpful guide to myself for using and maintaining the laser system. These guides are not meant as a replacement for the system manual and are by no means complete. Rather, they were written to be used in conjunction with the procedures outlined in the manual and were only ever meant to be a reminder of how to perform the steps listed there. The guide is divided into four subsections: daily operation guide (including shutdown procedure and misc. notes), full realignment procedure, pump laser maintenance, and dye change procedure. They are presented in that order.

Following the dye laser guides is a procedure outlining the startup and tuning of the 531 nm frequency doubler system. It describes the daily startup/usage produced, and also includes some brief notes on the bichromatic generation AOM setup. A brief overview of the AOM system is included as well.

E.1 Dye Laser Procedures

E.1.1 Daily Alignment

The Coherent 699 Dye Laser Operation:

1. Turn on cooling water
    a. Only leave it on when it's actively in use
2. Turn on Coherent control box
3. Turn on dye circulator
    a. Turn to internal circulation, let run to remove bubbles
    b. Look for pressure ~50psi
    c. Begin dye jet
4. Open laser case, examine dye jet
    a. Look for stable jet
5. Remove thin etalon port tape
    a. Clean optics (gently)
        i. First blow off dust, then wipe with MeOH
            1. Comp. Roms (near tweeter) => clean daily
            2. Other clean as needed
            3. Don't forget about the Brewster plate
6. Place power meter in beam path
    a. Should already be there!
7. Turn on I200 cooling water
    a. Open valve, turn on booster pump
        i. Don't leave running when the laser's off!
8. Activate Coherent I200 key switch (in rear)
9. No lasing until system power ON button is depressed (+60s delay)
    a. Clunk => lasing is imminent
    b. Look out for faults
        i. Power Track AT LIMIT => activate Tune; re-tune laser head (in rear)
            1. Power meter into beam path
            2. Vert & horz adjusts to ~6W (up to 7W); turn off Tune
        ii. Passbank Trans Failure
            1. Should clear automatically
            2. If persists, may need to repair laser controller
10. Dye laser should begin lasing when pump hits jet (warm up 1-2 mins)
    a. Must re-peak each time; keep dust covers closed if possible
        i. Adjust output coupler, pump mirror, tweeter
            1. Adjust a round of vert knobs, then horz knobs, repeat
11. Peak etalon adjustments
    a. Turn on oscilloscope
    b. Use Coherent laser control box
        i. Lock laser
        ii. Thin etalon => minimize back reflections on plate
        iii. Thick etalon => around draft tube knobs; max power
            1. May need to tweak etalon horz./vert. tilt (left side)
        iv. BRF => knurled knob on near side; max power
    c. Most drift is due to output vertical adjust
        i. Push on the output coupler vert. knob to test if near lasing
        ii. If it's not close enough to lase momentarily, do full realign

Shut down:

1. Remove BRF cover, set etalon to flash
    a. Adjust etalon horz./vert. tilt to align spots on roof
2. Turn off I200
    a. OFF button
    b. key switch out
    c. let water temp equalize (check by hand)
        i. Turn off Ar water valve, pressure pump
3. Turn off dye circulator, cooling water
4. Tape etalon port, put the cover on, close dust shields
5. Coherent box off, oscilloscope off

Alignment Notes & Misc.:

- Linewidth ~1MHz
- Thin etalon mode hop = 10 GHz (thick et)
    - +/- knob adjusts with scan
- BRF => 225 GHz (thin et)

AutoScan Notes:

- Thin etalon monitor (poke 0) => align to fringe minimum
- Program commands:
    - Run = autoscan program (just like startup Y/N query)
    - Peak Eta = peak etalon adjustment
    - Ctrl + Reset = breaks out of current program
        - Allows access to manual control options
    - Run 60000 = enables manual control
        - See list of Pokes for full external sensor options
        - Most common sensor options:
            - 0 = thin etalon monitor
            - 7 = laser power monitor

E.1.2 Full Cavity Realignment

Full Realignment:

1. Remove output end cover
    a. Place a card into the output to observe the mode
2. Remove BRF cover, set etalon to flash
    a. Observe spots on roof, adjust ICA to overlap
        i. Set horizontal angle on left side knob
            1. On the front/near side, leftmost ICA cradle knob
            2. Gently nudge the ICA if no horz movement
        ii. Set vertical angle on left side screw
            1. Leftmost flathead screw on ICA (above horz knob)
3. Pull Brewster plate up & out of the way
    a. Loosen far side knob and lift out of beam path
4. Remove ICA (requires ball-headed hex driver)
    a. Loosen spring-loaded knob on rear
    b. Unplug electrical connections
    c. Unscrew top screws (3) => loosen entirely (spring loaded)
        i. Gently lift straight up out of cradle
        ii. Put on something soft (large folded kimwipe)
5. Establish lasing in open cavity
    a. Start with last knob that was adjusted
    b. Align spots at all points on ring
        i. Output coupler
        ii. Upper fold mirror
        iii. Pump mirror
    c. Maximize power
        i. Adjust output coupler, pump mirror
            1. Can try tweeter too, but don't go too far
        ii. Clean any dusty optics
        iii. Should get ~800mW open cavity
6. Replace ICA
    a. Place gently in its cradle
    b. Tighten far knob, Allen screws
        i. Aim for ~1/4-midrange on spring compression
    c. Reattach serial interface cable (don't attach cable clamps)
    d. Set thin etalon knob to ~9-10 o'clock
    e. Set etalon back to flash
        i. See above
        ii. If lasing, peak up the power via tweeter & pump
            1. Very small adjustments
        iii. If not lasing, get it to do so
            1. Adjust cavity, reestablish flash lasing
                a. Look for orange output fluorescence
7. Walk ICA off flash
    a. Walk as far as possible off horz (just stops lasing)
        i. Adjust vertical to come back to full lasing
    b. Switch (walk off vert, bring back w/ horz)

    c. Repeat until operating point (max power)
        i. Use thin et. knobs to peak power while walking
        ii. If walk too far off may need to realign the cavity
8. Reinstall Brewster plate
    a. Lower Brewster plate into beam, tighten retention knob
    b. Reestablish lasing via vertical adjusts
        i. Output coupler
        ii. Tweeter
9. Maximize power
    a. Adjust BRF
    b. Adjust thin etalon
    c. Lock the laser
        i. Scan thin etalon, BRF
    d. Peak thick etalon knobs, output coupler
10. Align information beams
    a. Remove the small cover on the far end of the laser
    b. Push down magnetic-closure door on the front of the laser head
    c. Adjust position of the beam splitter to center the beam on last turning mirror
        i. If necessary, loosen thumbscrew on lower fold mirror and adjust to center
    d. Remove the detector block from the far side of the ref. cavity
    e. Pull the reference cavity out, place gently to the side
    f. Place a lens tissue between the two turning mirrors
        i. Use the set screw adjustments to center the beam through the ref cavity
            1. May need to re-adjust beam splitter position, but not usually
    g. Use the set screw adjustments to center the beam through the draft tube
        i. Move the draft tube around while observing the laser spot
            1. If the spot moves with the tube: the spot is a reflection, try again
            2. If the spot is obscured by the tube: all set
    h. Remove the lens tissue from between the mirrors
    i. Lower the reference cavity back into its cradle
        i. Use the screws to position the two spots ~2mm apart
            1. If only one spot is observed, try backing out all of the screws and tipping the cavity manually until you get it close
    j. Reattach the detector block
    k. Turn off the coherent control box
        i. Set display to ref cavity
        ii. Set mode to zero servo (calibration)
        iii. Set scan control to manual
    l. Turn the control box on
        i. Trace should reach all the way from -5V to +5V and lock at 0V when mode is set to Lock

E.1.3 Pump Laser Alignment

Ar Laser Maintainance:

1. Cleaning the Output Coupler
    a. Remove output cylinder
    b. Clean & drag cleaning w/ acetone then MeOH in-situ
    c. Optional:
        i. Remove and clean beamsplitter
        ii. Reinstall beamsplitter
    d. Reinstal output coupler assembley
        i. Look for notch matching
        ii. Screw in cover knob to finger tight
2. Clean front Brewster window
    a. Be VERY carefully
        i. Go from blunt end to sharp
    b. Use MeOH & hemostat => fold w/ hemostat 4-5x short side, then long side
        i. Re-cover plate between wipes
3. Clean rear mirror & Brewster the same way => mirror first, then window
    a. Mirror pulls out as a plug from rear
        i. set button in optic table hole
    b. Align notch & slide in => screw in cap
    c. Brewster w/ hemostat wipe (note: upside down)
        i. Can use acetone, but don't if not necessary
4. "Vertical Search" alignment
    a. Back off vert adjust
        i. Rock vert while adjust horz for laser flash
        ii. Dial in laser flash
            1. Power track will pull it back up to max
5. Put into tune mode & re-center power track
    a. Peak roughly w/ vert/horz adjusts in rear
    b. Power track back on => should be able to get control unit to laser head
6. Adjust aperture w/ hex wrenches
    a. Long SS screws on mounting plates
    b. Maximize power quickly vs. power track
        i. May be easiest to turn power track off for this part
7. "Walk-In" Procedure
    a. Adjust front, back mirrors & reset aperture => repeat vert then horz
    b. Allen key in front, clockwise until lasing almost stops
    c. Compensate in rear back to max
    d. Re-center aperture on new location (vert & horz)
        i. See what happened to power, move appropriately
            1. Go further or back up to maximize power?
                a. No change => good to go
                b. It's a pretty standard walk-in procedure
    e. Repeat with the other dimension (vert => horz or vice-versa)
8. Re-clean front Brewster window
9. Clean turning mirror while you're in the area

E.1.4 Dye Change Procedure

Dye Change:

1. Remove dye feed hose, place in a container large enough to hold the dye volume
    a. Be careful when removing the hose not to torque the dye jet assembly
2. Turn on dye module, drain the dye into a waste container. Turn the module off after all the dye has been drained.
3. Remove the input and output hoses from the dye accumulator, invert it over a waste container and drain.
    a. A large, wide plastic washtub makes an excellent waste container
4. Unplug the dye module, invert it over the waste container
5. Remove the filter housing and let it drain into the waste container
    a. On the older module, there is a wingnut at the top of the filter housing to drain, and a large nut at the bottom which secures the housing down; both should be removed in turn.
    b. On the newer module, there is no separate drain plug, simply unscrew the blue housing and let drain.
6. Wipe out the dye reservoir and filter housing. Replace the dye filter if necessary.
    a. (Optional) Flush the system with clean solvent
        i. Replace the filter cover without adding a filter and let the solvent circulate
        ii. This is a required step if you're changing to a different dye
7. Reattach hoses to the accumulator and laser, add ~700ml of dye to the reservoir
8. Cycle the dye internally until bubbles subside
9. Cycle the dye through the laser, topping off the reservoir as needed to avoid pulling air
    a. Should be ~1 L total, we usually use 1.1 L to be safe

E.2 Frequency Doubler Procedures

E.2.1 Daily Alignment

Doubling Crystal Alignment Procedure:

1. Turn on the system components
    a. Turn on the temperature controllers
        i. Don't forget to turn on power supplies if necessary
    b. Turn on the seed laser
    c. Turn on the IPG
        i. Do not activate emission yet
2. Set IPG amplifier to 1W output, activate emission
3. Peak the crystal temperature setpoint
    a. Increase the setpoint to sweep the temperature through the ideal
        i. Reset the Thorlabs max power point to the max doubler output (~17mW)
    b. Adjust temp by ±0.2°C, look for the max output temperature
4. Adjust crystal tip/tilt mount to maximize power
    a. Tip usually yields the most gain in power; tilt not as much
5. Maximize output via the x-translation stage
    a. CAUTION: this knob is *highly* sensitive!
6. Readjust the temperature as needed
    a. As the crystal warms up, the actual temperature will drift from the measured temperature and the temperature may need to be re-peaked
        i. Set the PID parameters for a slow lock to facilitate manual adjustments
7. Adjust the input focusing lens for maximum power
    a. Can adjust the two turning mirrors if necessary, but should be quite stable
8. Increase power incrementally and tune the temperature as needed
    a. Don't need to be super-fine with steps, but intermediate steps may be helpful getting the temperature close to its full-power setting

Changing Crystal Waveguides:

1. Set IPG to 2W output
2. Translate the x-stage slowly
3. Observe the crystal rear facet and watch for flashes of green emission
    a. Adjust the temperature to maximize the output power
4. Re-peak the output
    a. Starting with the x-stage adjustment

Note: if you're in an unknown slot or have to do a full re-alignment, you can translate the x-stage and count green flashes across the full width of the crystal for a quick location guide.

E.2.2 AOM Usage Guide

AOM RF Driver Configuration Notes:

There is a single RF synthesizer (16dBm max) driving both AOMs. The synthesizers is set with 1dB of attenuation, thereby yielding an output of 15dBm.

The synthesizer output is sent to a 50/50 splitter (-3dB in each arm) and immediately thereafter through a variable RF attenuator. The attenuators are identical and operate as follows:

- They take 5V power, delivered by the fixed 5V output of the TekPower supply
- Insertion loss of -3dB
- Control voltage is 0-20V:
    - 0V = no output power
    - 20V = full output power (input-3dB)

The two variable channels are dedicated to controlling the first and second stage AOMs. The first AOM stage is controlled by channel 1, the second AOM stage is controlled by channel 2.

Appendix F

Data Statistics

As stated previously, there was a lot of averaging that went into computing the data. There were significant shot-to-shot variations in the CaF flux, making it necessary to do lots of averaging to bring up the SNR. The average values and error bars were computed by aggregating all of the shots together and computing statistics on the combined values. Aggregate averages are easy enough: the average of the big data set is the average of the subset averages. Aggregate variances are a bit trickier. Intuition may suggest that it would behave like an average, but that's only half of the story. The aggregate variance is the average of the subset variances plus an additional term which computes the average difference of the subset averages from the total average. It makes total sense when you think about it a little bit, but it's not necessarily immediately obvious.

When combing datasets, rather than making a truly massive data file, I used statistics on the data subsets to build up statistics for the full dataset. This is a fairly straightforward process, detailed below.

Given two (or more) datasets, $x_1 = \{x_1^1, x_1^2, \cdots, x_1^{N_1}\}$, $x_2 = \{x_2^1, x_2^2, \cdots, x_2^{N_2}\}$, etc., their respective averages are given by:

$$\overline{x^i} = \frac{\sum_j x_i^j}{N_i}.$$

The average of the combined dataset, $\overline{x_T}$, is given by:

$$\overline{x_T} = \frac{\sum_k x^k}{N_T},$$

where $k = 1, \cdots, N_T = 1, \cdots, \sum_i N_i$. This can then be broken into $\sum_k = \sum_i (\sum_j^{N_i})$ such that we find

$$\overline{x_T} = \frac{\sum_k x^k}{N_T} = \frac{\sum_i \sum_j^{N_i} x_j^i}{\sum_i N_i},$$

which can be re-expressed as:

$$\overline{x_T} = \frac{\sum_i N_i \overline{x^i}}{\sum_i N_i}.$$

This is simply an average of the sub-set averages, weighted by the number of elements in each sub-set. When the sub-sets are all the same size, i.e. $N_i = N_j = N$, this reduces to a simple average of the averages:

$$\overline{x_T} = \overline{(\overline{x^i})}.$$

The standard deviation of the compound dataset is not quite as intuitive. Given an average and variance for each dataset, $\overline{x^i}$ and $(\sigma^i)^2 = v^i$, we can compute the total variance following a similar procedure as we did for the average. We define the total variance as:

$$v_T = \frac{\sum_k (x_k - \overline{x_T})^2}{N_T - 1},$$

where, again, $k = 1, \cdots, N_T = 1, \cdots, \sum_i N_i$. We again can break this up into a

sum over sums and consider the addition of $\overline{x^i} - \overline{x^i} = 0$ such that we find:

$$(N_T - 1)v_T = \sum_i \sum_j (x_i^j + (\overline{x^i} - \overline{x^i}) - \overline{x_T})^2 = \sum_i \sum_j ((x_i^j - \overline{x^i}) + (\overline{x^i} - \overline{x_T}))^2.$$

Distributing the square, we find the first term, $\sum_j (x_i^j - \overline{x^i})^2$, is simply $(N_i - 1)v^i$. We set aside the second term, $\sum_j (\overline{x^i} - \overline{x_T})^2$, and consider the cross term. With some algebra, it can be shown that this cross term, $\sum_i \sum_j (x_i^j - \overline{x^i})(\overline{x^i} - \overline{x_T})$, vanishes such that we find:

$$(N_T - 1)v_T = \sum_i ((N_i - 1)v^i + N_i(\overline{x^i} - \overline{x_T})^2),$$

i.e.

$$v_T = \frac{\sum_i ((N_i - 1)v^i + N_i(\overline{x^i} - \overline{x_T})^2)}{(N_T - 1)}.$$

The first term in the numerator is a weighted average of the variances for each sub-set, much like what we found for the total average value. This term alone, however, neglects variations which arise from the differences in sub-set averages from the total average. These additional fluctuations are accounted for by the second term in the numerator, and yields the combined data variance.

References

[1] R. Frisch, Zeitschrift für Physik **86**, 42 (1933).

[2] J.-L. Picqué and J.-L. Vialle, Optics Communications **5**, 402 (1972).

[3] R. Schieder, H. Walther, and L. Wöste, Optics Communications **5**, 337 (1972).

[4] M. Cashen and H. Metcalf, J. Opt. Soc. Am. B **20**, 915 (2003).

[5] M. Cashen, O. Rivoire, V. Romanenko, L. Yatsenko, and H. Metcalf, Phys. Rev. A **64**, 063411 (2001).

[6] M. T. Cashen and H. Metcalf, Phys. Rev. A **63**, 025406 (2001).

[7] M. T. Cashen, *Optical Forces on Atoms in Polychromatic Light Fields*, PhD thesis, State University of New York at Stony Brook, 2002.

[8] M. A. Chieda and E. E. Eyler, Phys. Rev. A **86**, 053415 (2012).

[9] M. A. Chieda, *Bichromatic Slowing of Metastable Helium*, PhD thesis, University of Connecticut, 2012.

[10] R. Grimm, Y. B. Ovchinnikov, A. I. Sidorov, and V. S. Letokhov, Phys. Rev. Lett. **65**, 1415 (1990).

[11] I. Kozyryev et al., Phys. Rev. Lett. **120**, 063205 (2018).

[12] J. Söding, R. Grimm, Y. B. Ovchinnikov, P. Bouyer, and C. Salomon, Phys. Rev. Lett. **78**, 1420 (1997).

[13] M. R. Williams, F. Chi, M. T. Cashen, and H. Metcalf, Phys. Rev. A **60**, R1763 (1999).

[14] V. S. Voĭtsekhovich, M. V. Danileĭko, A. M. Negriĭko, V. I. Romanenko, and L. P. Yatsenko, JEPT Lett. **49**, 161 (1989).

[15] L. Anderegg et al., Phys. Rev. Lett. **119**, 103201 (2017).

[16] J. F. Barry, E. S. Shuman, E. B. Norrgard, and D. DeMille, Phys. Rev. Lett. **108**, 103002 (2012).

[17] B. Hemmerling et al., Journal of Physics B: Atomic, Molecular and Optical Physics **49**, 174001 (2016).

[18] I. Kozyryev et al., Phys. Rev. Lett. **118**, 173201 (2017).

[19] E. S. Shuman, J. F. Barry, D. R. Glenn, and D. DeMille, Phys. Rev. Lett. **103**, 223001 (2009).

[20] E. S. Shuman, J. F. Barry, and D. DeMille, Nature **467**, 820 (2010).

[21] D. Wineland and W. Itano, Phys. Rev. A **20**, 1521 (1979).

[22] T. Hänsch and A. Schawlow, Opt. Comm. **13**, 68 (1975).

[23] H. J. Metcalf and P. van der Straten, J. Opt. Soc. Am. B **20**, 887 (2003).

[24] H. J. Metcalf and P. van der Straten, *Laser Cooling and Trapping*, Springer-Verlag, 1999.

[25] J. Javanainen, Phys. Rev. Lett. **64**, 519 (1990).

[26] X. Miao, E. Wertz, M. G. Cohen, and H. Metcalf, Phys. Rev. A **75**, 011402 (2007).

[27] D. Stack, J. Elgin, P. M. Anisimov, and H. Metcalf, Phys. Rev. A **84**, 013420 (2011).

[28] E. Ilinova, M. Ahmad, and A. Derevianko, Phys. Rev. A **84**, 033421 (2011).

[29] E. Ilinova, J. Weinstein, and A. Derevianko, New Journal of Physics **17**, 055003 (2015).

[30] A. Goepfert et al., Phys. Rev. A **56**, R3354 (1997).

[31] I. Kozyryev, L. Baum, K. Matsuda, B. Hemmerling, and J. M. Doyle, Journal of Physics B: Atomic, Molecular and Optical Physics **49**, 134002 (2016).

[32] M. Partlow, X. Miao, J. Bochmann, M. Cashen, and H. Metcalf, Phys. Rev. Lett. **93**, 213004 (2004).

[33] M. J. Partlow, *Bichromatic Collimation to Make an Intense Helium Beam*, PhD thesis, State University of New York at Stony Brook, 2004.

[34] M. R. Williams, F. Chi, M. T. Cashen, and H. Metcalf, Phys. Rev. A **61**, 023408 (2000).

[35] F. Bloch, Z. Phys. A-Hadron Nucl. **52**, 555 (1929).

[36] L. Aldridge, S. E. Galica, and E. E. Eyler, Phys. Rev. A **93**, 013419 (2016).

[37] L. Aldridge, *The Bichromatic Force in Multilevel Systems*, PhD thesis, University of Connecticut, 2016.

[38] S. E. Galica, L. Aldridge, and E. E. Eyler, Phys. Rev. A **88**, 043418 (2013).

[39] V. S. Voĭtsekhovich, M. V. Danileĭko, A. M. Negriĭko, V. I. Romanenko, and L. P. Yatsenko, JEPT Lett. **59**, 408 (1994).

[40] M. A. Chieda and E. E. Eyler, Phys. Rev. A **84**, 063401 (2011).

[41] L. Yatsenko and H. Metcalf, Phys. Rev. A **70**, 063402 (2004).

[42] J. H. Moore, C. C. Davis, M. A. Coplan, and S. C. Greer, *Building Scientific Apparatus*, Cambridge University Press, 4th edition, 2009.

[43] J. O. Clevenger, *Spectra and Dynamics of Calcium Monochloride*, PhD thesis, Massachusetts Institute of Technology, 2002.

[44] L. A. Kaledin, J. C. Bloch, M. C. McCarthy, and R. W. Field, Journal of Molecular Spectroscopy **197**, 289 (1999).

[45] M. Pelegrini, C. S. Vivacqua, O. Roberto-Neto, F. R. Ornellas, and F. B. C. Machado, Brazilian Journal of Physics **35**, 950 (2005).

[46] S. F. Rice, H. Martin, and R. W. Field, The Journal of Chemical Physics **82**, 5023 (1985).

[47] M. Dulick, P. F. Bernath, and R. W. Field, Canadian Journal of Physics **58**, 703 (1980).

[48] M. D. Morse, "Supersonic Beam Sources", in *Atomic, Molecular, and Optical Physics: Atoms and Molecules*, edited by F. Dunning and R. G. Hulet, volume 29 of *Experimental Methods in the Physical Sciences*, pages 21 – 47, Academic Press, 1996.

[49] C. M. Gittins, *Electronic Structure and Electronic-Vibrational Energy Exchange in Rydberg States of Calcium Monofluoride*, PhD thesis, Massachusetts Institute of Technology, 1995.

[50] X. Jiang, *Rydberg Spectroscopy of Calcium Monofluoride*, PhD thesis, Massachusetts Institute of Technology, 2004.

[51] N. Harris, *Rydberg Spectroscopy of Calcium Monofluoride and Calcium Monochloride*, PhD thesis, Massachusetts Institute of Technology, 1995.

[52] Y. Zhou, *Direct observation of Rydberg-Rydberg transitions via CPmmW spectroscopy*, PhD thesis, Massachusetts Institute of Technology, 2014.

[53] J. F. Barry, E. S. Shuman, and D. DeMille, Phys. Chem. Chem. Phys. **13**, 18936 (2011).

[54] M. R. Tarbutt et al., Journal of Physics B: Atomic, Molecular and Optical Physics **35**, 5013 (2002).

[55] T. E. Wall et al., Phys. Rev. A **78**, 062509 (2008).

[56] M. R. Tarbutt and T. C. Steimle, Phys. Rev. A **92**, 053401 (2015).

[57] J. Nakagawa, P. J. Domaille, T. C. Steimle, and D. O. Harris, Journal of Molecular Spectroscopy **70**, 374 (1978).

[58] P. J. Dagdigian, H. W. Cruse, and R. N. Zare, The Journal of Chemical Physics **60**, 2330 (1974).

[59] G. Herzberg, *Molecular Spectra, Vol. 1*, D. Van Nostrand Company, Inc., Toronto, 1963.

[60] J.-C. D. Meiners, Precise determination of EF $^{l}\Sigma_{g}^{+}$ levels in H_2, D_2, and HD, Master's thesis, University of Delaware, 1994.

[61] P. C. D. Hobbs, Opt. Photon. News **2**, 17 (1991).

[62] E. C. Hamamatsu Photonics K.K., Photomultiplier tubes: Basics and applications, Technical Report 3a, Hamamatsu Photonics K.K., 2007.

[63] L. N. Pfeiffer and J. F. Porter, Appl. Opt. **3**, 317 (1964).

[64] C. S. French, Appl. Opt. **4**, 514 (1965).

[65] W. H. Turner, Appl. Opt. **12**, 480 (1973).

[66] M. P. F. Bristow, Appl. Opt. **18**, 952 (1979).

[67] S. Reichel, R. Biertümpfel, and A. Engel, DGaO Proceedings 2015 (2015).

[68] Kopp Glass, Filter glass equivalency guide - filter cross reference, `http://www.koppglass.com/filter-catalog/filter-equivalency-guide.php`.

[69] C. J. Erickson, M. V. Zijll, G. Doermann, and D. S. Durfee, Review of Scientific Instruments **79**, 073107 (2008).

[70] D. L. Troxel, C. J. Erickson, and D. S. Durfee, Review of Scientific Instruments **82**, 096101 (2011).

[71] M. F. Stone, Stabilized external-cavity diode lasers, Master's thesis, State University of New York at Stony Brook, 2001.

[72] G. D. Boyd and D. A. Kleinman, Journal of Applied Physics **39**, 3597 (1968).

[73] Covesion, Ltd., Covesion guide to PPLN, `https://www.covesion.com/support/covesion-guide-to-ppln.html`, 2016.

[74] P. L. Gould, G. A. Ruff, and D. E. Pritchard, Phys. Rev. Lett. **56**, 827 (1986).

[75] J. F. Barry, *Laser cooling and slowing of a diatomic molecule*, PhD thesis, Yale University, 2013.

[76] J. E. Murphy, J. M. Berg, A. J. Merer, N. A. Harris, and R. W. Field, Phys. Rev. Lett. **65**, 1861 (1990).

[77] E. E. Eyler, Review of Scientific Instruments **82**, 013105 (2011).

[78] E. E. Eyler, Review of Scientific Instruments **84**, 103101 (2013).